PROCEEDINGS BOOK OF 2rd INTERNATIONAL CONFERENCE ON PROGRESSES IN AUTOMOTIVE TECHNOLOGIES: ICPAT 2020

ICPAT'20

December 28 - 29, 2020

Istanbul – TURKEY

CONFERENCE CHAIR

Prof. Dr. Kadir Aydın (Çukurova University, Adana, Turkey)

CONFERENCE CO-CHAIR

Prof. Dr. Hakan Serhad Soyhan (Sakarya University, Sakarya, Turkey)
Assoc. Prof. Dr. Hasan Köten (Istanbul Medeniyet University, Istanbul, Turkey)

PLENARY SPEAKERS

Prof. Dr. Zafer Gül (Marmara University, Istanbul, Turkey)

Prof. Dr. Muhammad Sultan (Bahauddin Zakariya University, Multan, Pakistan)

Prof. Dr. Hua Zhao (Brunel University, London, England)

Dr. Emre Özgül (Ford Otosan, Istanbul, Turkey)

SCIENTIFIC COMMITTEE

Abdullah Selim Parlakyiğit (Istanbul Medeniyet University, Istanbul, Turkey)

Ahmet El Baz (The British University in Egypt, Egypt)

Ayman M. Elhagrasy (King Abdullah University of Science and Technology, Saudi Arabia)

Balaram Kundu (Jadavpur University, India)

Burak Safaker (Southern Illinois University Edwardsville, Edwardsville, USA)

Dongsheng Wen (University of Leeds, Leeds, United Kingdom)

Ehsan Ebrahimnia-Bajestan (Graduate University of Advanced Technology, Kerman, Iran)

Emre Cenker (Sandia National Laboratories, California, USA)

Fethi Khaled (King Abdullah University of Science and Technology, Saudi Arabia)

Godson Asirvatham Lazarus (Karunya University, Coimbatore, India)

Hong G. Im (King Abdullah University of Science and Technology, Saudi Arabia)

Ioan Pop (Emanuel University, Oradea, Romania)

Mohamed Awad (Mansoura University, Mansoura, Egypt)

Moh'd A. Al-Nımr (Jordan University of Science and Technology, Jordan)

Mustafa Yılmaz (Marmara University, Istanbul, Turkey)

Özlem Boydak (Istanbul Medeniyet University, Istanbul, Turkey)

Patrice Estelle (University of Rennes 1, Rennes, France)

Taib Iskandar Mohamad (National University of Malaysia, Selangor, Malaysia)

Tolgahan Kaya (TUBITAK-The Scientific and Technological Research Council of Turkey, Turkey)

Ismail H. Savci (Ford Otosan, Turkey)

Mehmet Ozdemir (Bozankaya A.S., Turkey)

Altay Arbak (Istanbul Technical University, Istanbul, Turkey)

Kaan Erdem (Istanbul Technical University, Istanbul, Turkey)

Tuğba Tetik (Istanbul Technical University, Istanbul, Turkey)

Duygu Gündüz Raheem (Marmara University, Istanbul, Turkey)

Turgay Eray (Adnan Menderes University,Aydin, Turkey)

Fatih Öztürk, Istanbul Medeniyet University, Istanbul, Turkey)

Dhinesh Balasubramanian (Mepco Schlenk Engineering College, Tamil Nadu, India)

Gülsüm Kübra Kaya (Istanbul Medeniyet University, Istanbul, Turkey)

Kamil Koçak (Istanbul Medeniyet University, Istanbul, Turkey)

PRESENTATIONS

A Study of Ignition Delay, Combustion Process and Emissions in a High Ambient Temperature of Diesel Combustion

Iqbal Shahridzuan Abdullah[1,] Amir Khalid*[1], Norrizam Jaat[1], Ridwan Saputra Nursal[1,2] Hasan Koten[3] Yasin Karagoz[3]

[1]*Automotive and Combustion Synergies Technology Group, Universiti Tun Hussein Onn Malaysia, 84600 Pagoh, Johor, Malaysia*

[2]*Department of Marine Engineering, Politeknik Bagan Datuk, 36400 Hutan Melintang, Perak, Malaysia*

[3]*Mechanical engineering Department, Istanbul Medeniyet University, 34700 Istanbul, Turkey*

Corresponding Author E-mail: amirk@uthm.edu.my

ABSTRACT

Pre-inflammation mixture formation plays as a core factor of diesel combustion. The goal of this research was to better understand the effects of air-fuel mixing process during the time of ignition delay and initial heat release in the combustion process that strongly influence exhaust emissions. This study explored the ignition delay, combustion process and emissions in a high ambient temperature of diesel combustion. The Rapid Compression Machine (RCM) simulated real phenomena in the combustion chamber. This analysis used 5vol%, 10vol%, and 15vol% mixing of palm oil methyl ester with standard diesel fuel in B5, B10, and B15 diesel engines and standard diesel itself. Injection pressure ranged from 80 MPa to 140 MPa, while RCM atmospheric temperature ranged from 750 K to 950 K. For all tested fuels, the ignition delay time decreased as the ambient temperature rose. The initial heat release becomes more prolonged to lower ambient temperatures, and its peak was observed to rise gradually and shorten the delay of ignition. High ambient temperature effects showed a reduction in emissions, particularly HC, CO and CO_2.

INTRODUCTION

The global fuel reserve has been depleting steadily across the year. Due to this situation, alternative fuel were researched as a substitution for the conventional fuel. One of the renewable fuel used for economic stabilisation is biodiesel fuel. Biodiesel has become an enticing alternative to traditional diesel fuel, helping to minimise reliance on imported petroleum and providing lower pollutant emissions in the new pollution control setting. Considering both economic and environmental advantages, biodiesel production is increasing worldwide as an alternative petroleum diesel fuel. Biodiesel is commonly classified as ester-based fuels (fatty esters) and can be manufactured using alcohols such as methanol and ethanol from different palm oils, animal fats, or waste cooking oils.

This research uses biodiesel from palm oils. Biodiesel has higher viscosity, density, flash point and amount of cetane than normal diesel fuel [1-5]. In addition it is non-toxic, oxygenated, biodegradable and environmentally safe. Biodiesel fuel properties significantly influence engine efficiency, emission characteristics, and lead variations in the conduct of combustion [6–8]. Biodiesel offers many benefits over fossil fuel, such as bio-diesel provides smoother engine operation by improving lubricity and combustion properties.

Biodiesel can substantially minimise greenhouse gas emissions to the atmosphere by minimising CO, unburned hydrocarbon and particulate matter, but biodiesel creates higher nitrous oxide emissions that are being more closely controlled worldwide [9]. Regardless of many attempts to improve the emission of BDF, it still has NOx and particulate matter (PM) emission problems. This is because of the cetane number, biofuel composition, and stoichiometric point and antioxidants properties of the BDF. [10]. PM is released in a rich region, while NOx is formed in a high temperature and stoichiometric mixture zone. It is understood mixture formation manipulability in the diesel engine is crucial to refine the exhaust emissions [8]. Mixture forming during early burning is especially important as ignition is regulated by physical processes induced by multi-hole injection and air movement and chemical processes of fuel decomposition and oxidation [12]. The effect of variant ambient temperature against the heat release rate, ignition delay time and emission were analysed using the rapid compression machine (RCM). A constant volume chamber is an excellent instrument for researching temperature effect on auto ignition of combustible mixtures as it provides direct measurement of ignition delay [13]. The engine performance and emission is very relatable with the ignition delay of the fuel. Ignition delay is the period when the first droplets of the fuel enter the combustion chamber until the point where the slightest of flame is observed. In diesel engine, ignition delay is a major factor deciding the rapid pressure increase in the initial burning stage and subsequent stages of combustion. The ignition delay in a diesel engine is can be separated into two different classification which is, the physical and chemical ignition delay [14].

Physical ignition delay refers to the fuel-air mixture formation and the chemical ignition delay to the time required for an exponential rise in chemical reaction rate. The factors that effects the physical delay were atomization, infiltration,

air entry and vaporisation, and for the chemical delay, the factor effecting were fuel decomposition, aggregation and oxidation [15]. According to Yiming Wang et al. [16] in an analysis of high-temperature combustion phenomena using a constant volume chamber, it was concluded that at high temperatures the ignition delay is very brief and the ignition happens near the tip of the nozzle and the combustion time is protracted. Temperature effects on the ignition process are examined up to the initial stages of pressure increase resulting from net heat release due to fuel evaporation and heating [17]. Biodiesel based on palm oil production was planned from 1982 to use B5 (5 percent palm oil and 95 percent diesel) blend for Malaysian factories and vehicles. Malaysia's government introduced the first biodiesel blend with petroleum diesel known as B5 with a commercial name called Envo Diesel [18-19]. In addition, National Biofuel Policy (NBP) along with Envo Diesel's officially launch in 2006 under the Malaysia Ministry of Plantation Industries and Commodities. NBP's most significant initiatives were palm oil as a biofuel to replace synthetic fuels [20].

In addition, these measures were drafted to ensure that biofuel remained one of the country's five energy sources. Other primary goals of the instigated strategy are to encourage palm oil for domestic and international markets, decrease the loss of crude oil, and maintain the commodity at the par price. B5's obligatory mixing was introduced in phases starting 2011 and expanded to B7 by the end of 2014. The government has adopted the B10 in 2018 and expected to introduce the B20 in 2020 after the successful introduction of B5, B7 and B10. The biodiesel mandate positively impacted Malaysian palm oil's domestic market. It indicates the government's willingness to use palm biodiesel locally as green energy leading to a cleaner environment [21].

METHODOLOGY
Biodiesel blend preparation
Biodiesel blend preparation was explained in detail in this particular section. The biodiesel fuel used in this experiment was a combination of CPO and standard diesel, Euro 5. The blending machine was used to get three different biodiesel fuel blending ratio. The blending process took 2 hours at 70oC and spinning blade speed held at 270 RPM. Table 1 displays the nomenclature of blends with their arrangement. The physicochemical properties (Density, Kinematic Viscosity, Cetane Number, Flash Point and Low Heating Value) of all the blend tested in the experiment were done after blend preparation. The fuel properties were checked using ISO for each property. Table 2 reported the fuels' properties.

Table 1: Nomenclature of all tested fuel.

No.	Name	Composition
1.	Diesel	Euro 5
2.	B5	5% CPO + 95% EURO 5(by volume)
3.	B10	10% CPO + 90% EURO 5(by volume)
4.	B15	15% CPO + 85% EURO 5(by volume)

Table 2: Properties of BDFs and diesel.

	B5	**B10**	**B15**	**Diesel**
Density (kg/m^3)	837.1	837.7	840.4	833.7
Kinematic Viscosity (mm^2/s)(40°C)	3.00	3.01	3.04	2.9
Cetane number	56.1	56.3	56.4	55.7
Flash Point	91.5	92.0	93.5	8.0
Low Heating Value(MJ/kg)	39.2	38.9	38.4	45.8

Combustion process analysis

Using a rapid compression machine, the effects of ambient temperature on combustion process were studied. RCM or precisely the free-piston compression machine simulated the diesel combustion in a constant volume over a broad range of pressure conditions and atmospheric temperature comparable to real diesel engines. Rapid compression machines (RCM) are considered an essential experimental instrument to understand the initial temperature needed for auto-ignition under idealised engine-like conditions. This is because a particular condition in the RCM can be manipulated while it is hard to manipulate in a diesel engine. RCM simulates specifically a single compression stroke in an internal combustion engine cycle. Figure 1 displays RCM's schematic diagram. The test condition manipulated in the analysis was the percentage of atmospheric temperature, injection pressure, and blending ratio. Table 3 revealed the experimental specification. Data on ignition delay and the heat release rate defines the ignition behaviour of tested fuels under practical engine conditions. In order to calculate ignition delay times in the aspect of ambient temperature

and fuel form RCM was mainly selected for this research. RCM was chosen and not the standard diesel engine because it is hard to manipulate the ambient temperature in standard diesel engine while it is easier using RCM.
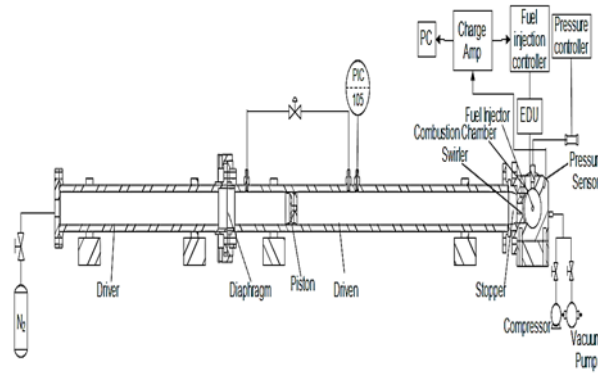

Figure 2: RCM Schematic Diagram

Table 3: Experimental specifications.

Parameter	Information
Injector type	6 holes, Ø = 0.129 mm
Fuel type	Diesel, B5, B10 and B15
Injection Pressure, P_{inj} [MPa]	140, 130, 100, 80
Fuel quantity, q_i [ml]	0.04
Ambient Temp, T_i [K]	750, 850, 950
Swirl velocity r_s [m/s]	19
Ambient density, ρ [kg/m^3]	16.6
Oxygen concentration, O_2 [vol%]	21

Heat release rate calculation

The chamber pressure obtained by the piezoelectric pressure transducer (Kistler, 1510A) was used to calculate and acquire the heat release rate dQ/dt. The measured heat release rate is a net apparent heat release that involves energy losses due to the transfer of heat to the chamber wall and the release of chemical heat. Thus specific heat ratio was implemented with specified mathematical equation. The equation used was as below.

$$dQ_c = \alpha. A_w. (T - T_w). dt \quad \text{........ (1)}$$

Where,

A : The thermal diffusion coefficient between the
    wall and gas
A_w : Total area of combustion chamber walls
T_w : Temperature of combustion chamber wall (T_w =30°C)

RESULT AND DISCUSSION

A relationship between the ignition delay and surrounding air ambient temperature is known to be of great importance for studying and simulating the cycle of diesel engines, as temperature is the primary component. Many study was conducted in this direction, focusing on experimental findings in engines and constant volume chambers. The time scales used in RCM was in ms units, hence it is useful to use RCM facilities to calculate ignition delay times over a large temperature range. Usually, these ignition delay times depend on an experiment's temperature, where generally shorter ignition delay would be obtained in higher temperatures.

Rapid Compression System tests were performed to measure ignition delays to produce base line characteristics. These base line characteristics of conventional diesel fuels were then contrasted with the characteristics of diesel blends of oil palm-based biodiesel fuels. This analysis used regular diesel fuel available on the market. After diligent filtration, all blends and samples were prepared and blended correctly.

Ignition time is the duration between beginning the fuel injection into the combustion chamber and starting the combustion during the delay period, all physical and chemical changes happened simultaneously. The variations in atmospheric temperature influence both physical and chemical processes during ignition delay. During the delay of

ignition, chemical processes tend to regulate rather than physical processes. Previous experiments found the greater value of the chemical component of the ignition delay over the physical portion. Therefore, any change in the temperature of the reactants between air and fuel mixing during the ignition delay is likely to influence the duration of the ignition delay.

Figure 4.1 maps the influence of atmospheric temperature on variation of ignition delay for different injection pressures with different fuels used. Separate diagrams for transparency. The observation results from the figures given below that the inflammation delay patterns for the different fuels are identical, with estimated ignition delays continuously declining as the atmospheric temperature rose. Theoretically, two-part ignition delay is an amount of physical ignition delay and chemical ignition delay. As the atmospheric temperature of the combustion chamber increases, the impeding fuel spray's chemical delay decreases as pre-flame chemical reactions occurring during chemical delay become swift. Thus, chemical latency decreases as air temperature increases. Higher air-fuel mixing rate due to faster fuel evaporation because of hot surface within the combustion chamber also further decrease the ignition delay. The spray impingement on the hot surface causes the process of fuel evaporation and fuel-air mixing.
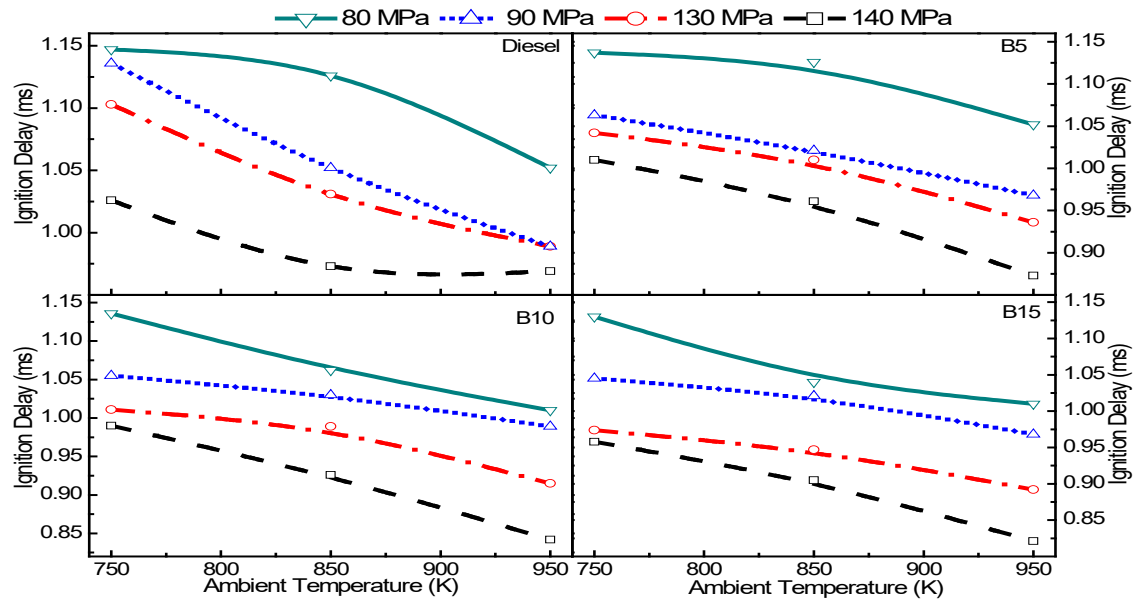

Figure 4.1: Effects of ambient temperature, Ti on ignition delay.

It is crucial to obtain the dQ/dt to identify the combustion characteristic of a particular fuel tested. Equation (1) was used to calculate the dQ/dt based on the first law of thermodynamics. It depends on the ignition delay and fuel properties which is the BDF with blending ratio of 5%, 10% and 15%.

Figure 4.2 to Figure 4.5 displays records of diesel, B5, B10 and B15 in combustion chamber pressure and heat release concentrations at varying ambient temperatures. Combustion pressure, Pf and heat release, dQ/dt with needle rise, NL against time t from the start of injection. The effect of atmospheric temperatures on the production of combustion at base oxygen concentration O_2=21% vol. The data collection process started as the injector was activated, and the ambient temperature ranged from 750 K to 950 K.

As seen in the figures, at lower ambient temperatures, the initial heat release is delayed, and its peak is found to rise continually and shortens the combustion period. As the ignition delay of B5, B10 and diesel fuel lengthens, a constant rise in dQ/dt was observed. A more significant amount of accumulated combustible mixture, longer physical process and lower initial reactant temperature can affect this form of heat release histories, particularly at T_i = 750 K. The reducing chemical reaction rate can explain an increase in the ignition delay in the combustion chamber as T_i declines. Provided that the temperature T_i is mean temperature, and the local temperature of the combustible mixture influences ignition, the variation of temperature distribution at low-temperature conditions affects ignition further.

With almost the same volume of fuel pumped, the peak combustion pressures are very similar at varying atmospheric temperatures. It can be seen at a lower ambient temperature the combustion had a slightly higher pressure. Longer ignition delay leads to more premixed combustion in the chamber and hence further increases the chamber pressure. Otherwise, lower heat loss through the chamber wall and lower ambient temperature flame radiation can also help increase the pressure.

The autoignition delay increased at lower ambient temperature. The decrease in ignition delay provided more time for the liquid jet to penetrate the chamber, and more atmospheric air to create a premixed zone of fuel vapour. Thus, with declining atmospheric temperature, spray jet caused more ambient air, and premixed combustion consumed more carbon.

According to the analysis of the figure, the higher ambient temperature combustion indicates a lower ignition delay for all fuels tested. At higher atmospheric temperature, faster evaporation of fuel mixture and shorter penetration occurred. Nonetheless, BDF has a shorter ignition delay than diesel at the same ambient temperature, which was because of higher cetane number and higher viscosity of the BDF. The reason for this phenomenon is that the biodiesel

is less compressible and injected from the injector nozzle earlier than diesel, which then results in the earlier start of biodiesel combustion versus diesel fuel. Next, the stoichiometric state was able to be achieved faster due to the oxidizer content within the biodiesel mixtures [74].
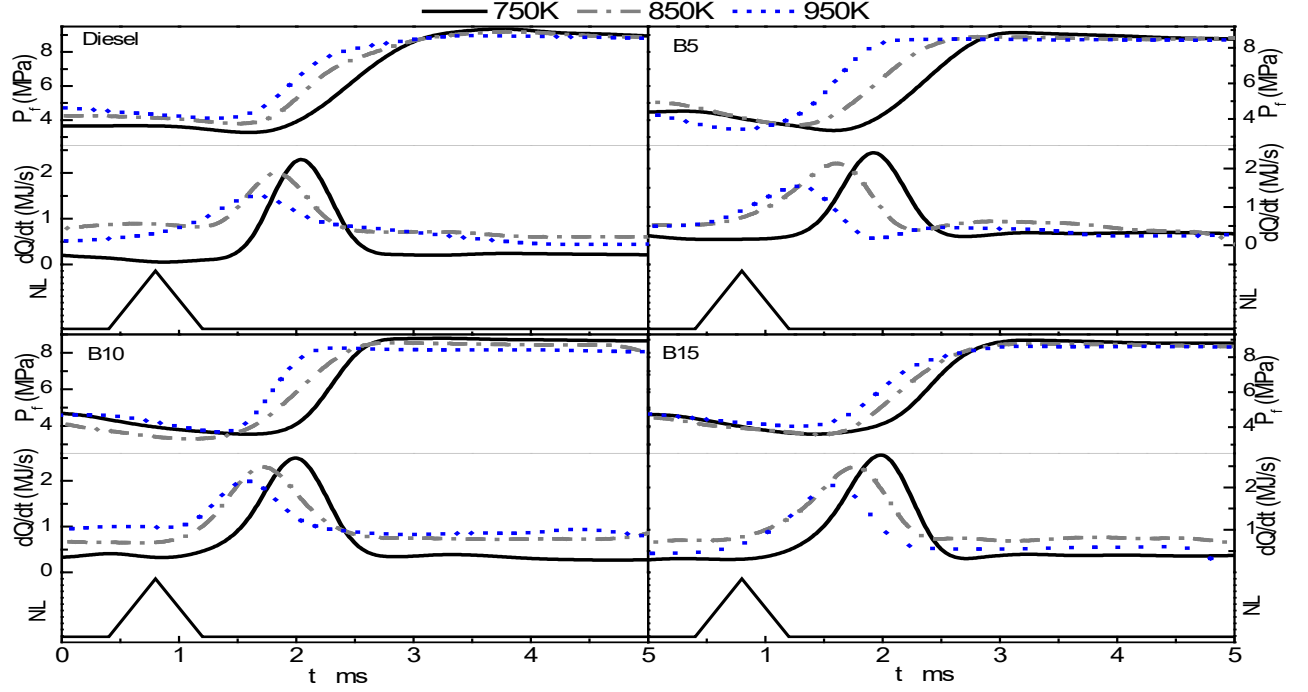
Figure 4.2: Effects of ambient temperature on heat release at P_{inj} = 80 MPa
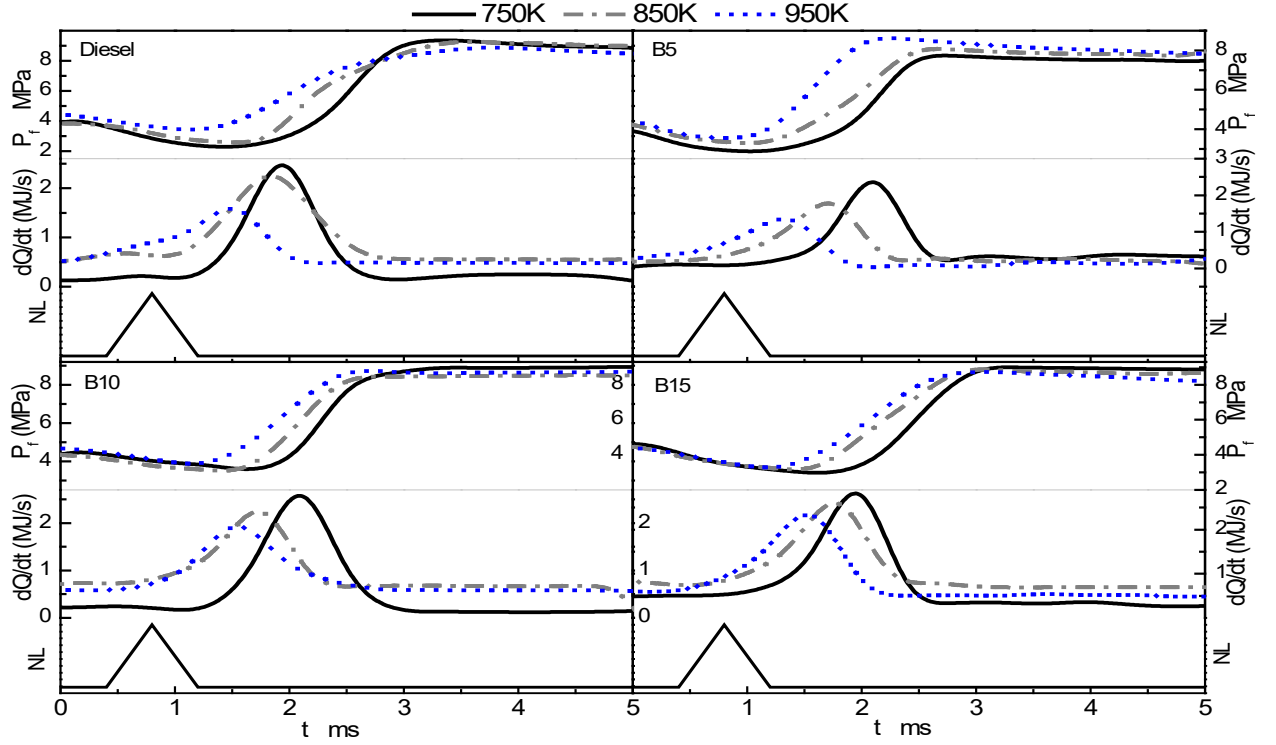
Figure 4.3: Effects of ambient temperature on heat release at P_{inj} = 100 MPa.
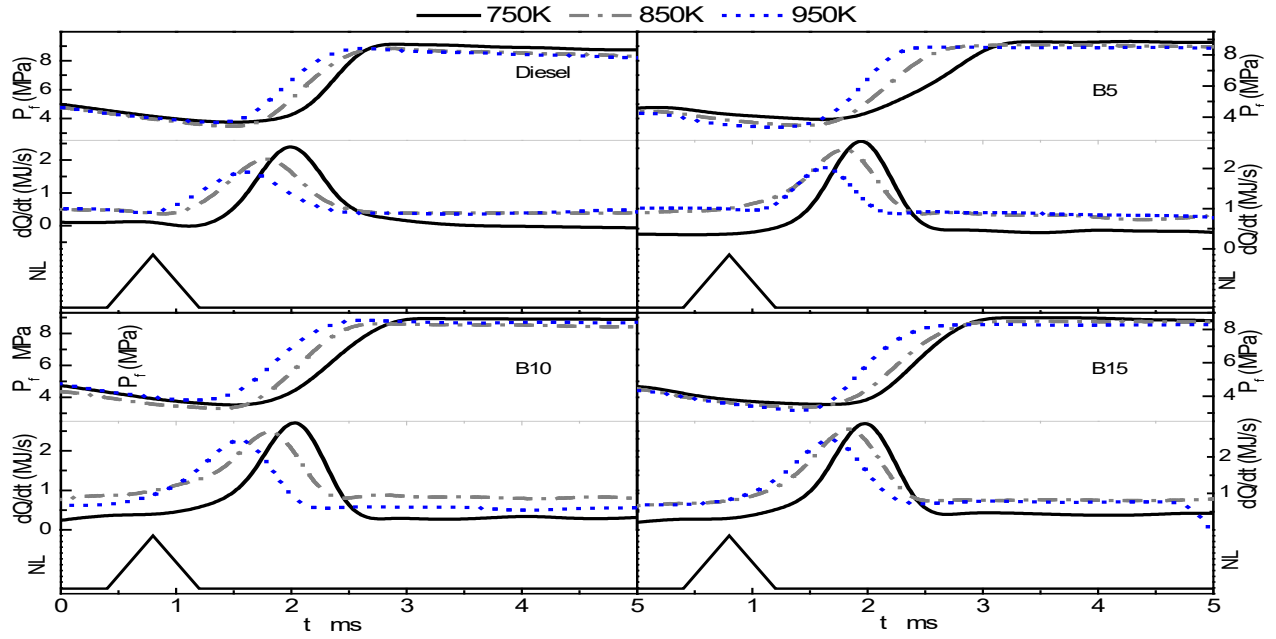
Figure 4.4: Effects of ambient temperature on heat release at P_{inj} = 130 MPa.
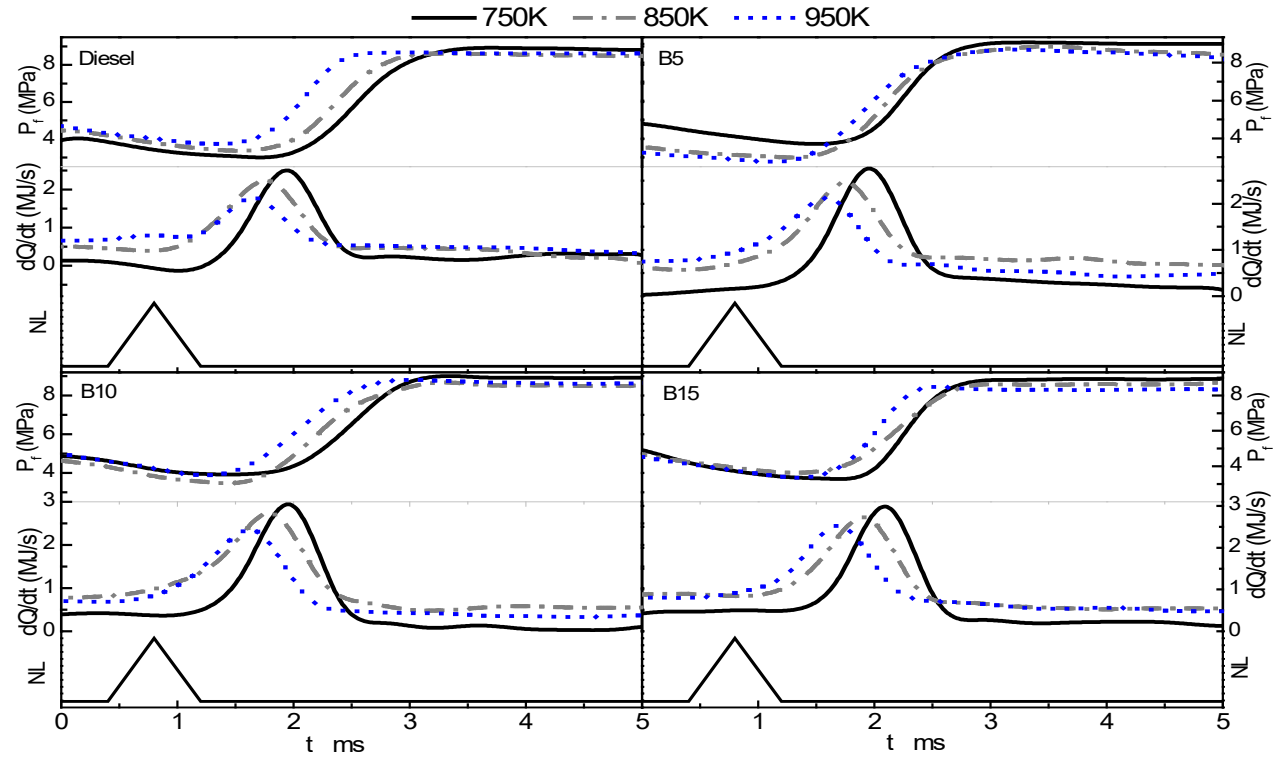
Figure 4.5: Effects of ambient temperature on heat release at P_{inj} = 140 MPa.

The effect of ambient temperature on emission was first measured with the parameters while using biodiesel B5 and preceded by B10 and B15, with ambient temperature conditions Ti at 750 K, 850 K and 950 K respectively. In base condition, with pressure chamber, pc = 100 kPa, injection pressure Pinj=100 MPa with fuel quantity qi = 0.04 ml, swirl rs = 19 m / s and density π= 16.6 kg / mm.

The emission readings are graded by injection pressure, P_{inj} = 100 MPa relative to the use of various biodiesel grades B5, B10 and B15. Comparison of pollution readings reveals that compounds are not proportional in each parameter. Generally, the amount of compounds fluctuates with each of the biodiesel grades as well as the different atmospheric temperatures used.

CONCLUSION

Throughout the studies, various outcome were obtained which were concluded as below:

- Ignition delay is mainly affected by the physical properties of fuels such as density, viscosity, temperature, and pressure. The fuel cetane number reflecting fuel ignitability also has significant effects on ignition delay. This

6

study showed that in terms of ignition delay, the biodiesel has excellent overall behaviour. The ignition delay was highly sensitive with the change of the ambient temperature.

- It is concluded that as the T_i increased, the ignition delay shortens. Compared to standard diesel, BDF had a shorter ignition delay. As prolonged with increasing biodiesel content in the blends, the ignition delay shortens furthermore. It is due to the characteristic of BDF, which has a higher cetane number and oxygen content.

- At high ambient temperature, the ignition occurs near the nozzle. Thus, the initial combustion rate becomes low, and the combustion duration became shorter. As a result, good fuel conversion and complete combustion process occur.

- At varying ambient temperatures in the combustion chamber, exhaust emissions rise as ambient temperature rises. It is found that at the high ambient temperature, the fuel smoke opacity was lower. However, it improved significantly as the ambient temperature increase as more fuel is pumped at a higher temperature, so less oxygen is required for the reaction.

REFERENCES
[1] A. Datta, and B. K. Mandal, "A comprehensive review of biodiesel as an alternative fuel for compression ignition engine," Renew. Sustain. Energy Rev., vol. 57, pp. 799–821, 2016.
[2] [2] Khalid, A. (2013). Effect of ambient temperature and oxygen concentration on gnition and combustion process of diesel spray. Asian Journal of Scientific Research, 6(3), 434-444. doi:10.3923/ajsr.2013.434.444
[3] Khalid, A., Tajuddin, A. S. A., Jaat, N., Manshoor, B., Zaman, I., Hadi, S. A. A., & Nursal, R. S. (2017). Performance and emissions of diesel engine fuelled with preheated biodiesel fuel derived from crude palm, jatropha, and waste cooking oils. International Journal of Automotive and Mechanical Engineering, 14(2), 4273-4284. doi:10.15282/ijame.14.2.2017.12.0341
[4] Andsaler, A. R., Khalid, A., Adila Abdullah, N. S., Sapit, A., & Jaat, N. (2017). The effect of nozzle diameter, injection pressure and ambient temperature on spray characteristics in diesel engine. Paper presented at the Journal of Physics: Conference Series, , 822(1) doi:10.1088/1742-6596/822/1/012039.
[5] C. Wityi et al., "Ignition and combustion characteristics of various biodiesel fuels (BDFs)," Fuel, vol. 158, pp. 279–287, 2015.
[6] A. N. Ozsezen and M. Canakci, "Determination of performance and combustion characteristics of a diesel engine fueled with canola and waste palm oil methyl esters," Energy Conversion and Management, vol. 52. pp. 108–116, 2011.
[7] M. Suresh, C. P. Jawahar, and A. Richard, "A review on biodiesel production, combustion, performance, and emission characteristics of non-edible oils in variable compression ratio diesel engine using biodiesel and its blends," Renew. Sustain. Energy Rev., vol. 92, no. April, pp. 38–49, 2018.
[8] A. S. Yusuff, O. D. Adeniyi, M. A. Olutoye, and U. G. Akpan, "Performance and Emission Characteristics of Diesel Engine Fuelled with Waste Frying Oil Derived Biodiesel-Petroleum Diesel Blend," Int. J. Eng. Res. Africa, vol. 32, pp. 100–111, 2017.
[9] P. Mccarthy, M. G. Rasul, and S. Moazzem, "Analysis and comparison of performance and emissions of an internal combustion engine fuelled with petroleum diesel and different bio-diesels," Fuel, vol. 90, no. 6, pp. 2147–2157, 2011.
[10] I. Miyata, Y. Takei, K. Tsurutani, and M. Okada, "Effects of Bio-Fuels on Vehicle Performance : Degradation Mechanism Analysis of Bio-Fuels Reprinted From : Alternative and Oxygenated Fuels," SAE Pap. No. 2004-01-3031, 2004.
[11] A. Khalid, T. Yatsufusa, T. Miyamoto, J. Kawakami, and Y. Kidoguchi, "Analysis of Relation between Mixture Formation during Ignition Delay Period and Burning Process in Diesel Combustion," SAE Pap. No. 2009-32-0019, 2009.
[12] W. Jazair, T. Harada, S. Kubo, Y. Kidoguchi, and K. Miwa, "Improvement of Emissions in a DI Diesel Engine Fuelled by Bio-diesel Fuel and Waste Cooking Oil," SAE Pap. No 2007-01-2029, Jul. 2007.
[13] M. Ikegami, K. Miwa, and M. Inada, "A Study on Ignition and Combustion of a Diesel Spray by Means of a Rapid Compression Machine," Bull. JSME, vol. 24 No 195, 1981.
[14] E. Rosseel and R. Sierens, "The Physical and the Chemical Part of the Ignition Delay in Diesel Engines," SAE Pap. No. 961123, 1996.
[15] F. E. Corcione, B. M. Vaglieco, G. Valentino, and I. Motori, "A Study of Physical and Chemical Delay in a High Swirl Diesel System via Multiwavelength Extinction Measurements," SAE Pap. No. 980502, no. 724, 1998.
[16] Y. Wang, C. Yang, and G. Shu, "An Observation of High Temperature Combustion Phenomenon in Low-Heat-Rejection Diesel Engines," SAE Pap. No 940949, no. 412, 1994.
[17] G. R. Kannan and R. Anand, "Effect of injection pressure and injection timing on DI diesel engine fuelled with biodiesel from waste cooking oil," Biomass and Bioenergy, vol. 46, pp. 343–352, 2012.
[18] M. Faizal and S. Ateeb, "Energy, Economic and Environmental Impact of Palm Oil Biodiesel in Malaysia," J. Mech. Eng. Res. Dev., no. September, pp. 93–96, 2018.
[19] M. H. Ong HC, Mahlia TMI, "A review on energy pattern and policy for transportation sector in Malaysia," Renew Sustain Energy Rev, vol. 16, pp. 532–542, 2012.

[20] S. Lim and K. T. Lee, "Implementation of biofuels in Malaysian transportation sector towards sustainable development : A case study of international cooperation between Malaysia and Japan," Renew. Sustain. Energy Rev., vol. 16, no. 4, pp. 1790–1800, 2012.

[21] B. Nambiappan et al., "Malaysia : 100 Years of Resilient Palm Oil Economic Performance," J. Oil Plam Resesarch, vol. 30, no. March, pp. 13–25, 2018.

DESIGN AND FABRICATION OF SOLAR HEAT CELL USING PHASE CHANGE MATERIALS

Bilal Anwar[1*], Adnan Aslam Noon[1], Hasan Koten[2], Yasin Karagoz[2],
Muhammad Zeeshan Khan[1], Iftikhar Ali[1]

[1] *International Islamic University, Mechanical Engineering Department, Islamabad, Pakistan.*

[2] *Istanbul Medeniyet University, Mechanical Engineering Department, Istanbul, Turkey.*

[*]bilalktkiiui@gmail.com , *[1]adnan.aslam@iiu.edu.pk* , *[2]hasan.koten@medeniyet.edu.tr* ,

[1]zeshankhan028@gmail.com , *[1]iftukhar333@gmail.com*

ABSTRACT

Thermal comfort as well as lower cooling and heating loads are need of the world today. Various studies has shown that thermal energy storage (TES) is a way to accomplish this goal. Our aim in this study is to store heat energy in a cylinder (called cell) from the sun light and to use the stored heat in absence of sunlight for cooking and other heating purposes. Estimates are made for designing a cell, capable of storing heat from sunlight, required to boil a cup of water. Focused sunlight is used to charge the cell from sunlight. The focused light is produced by focusing plate. The cell is kept at the focal point of focusing plate. After some time the cell stores this heat by specific type of materials inside it. These materials are called phase change materials (PCM). Initially PCM heat up by concentrated beam of sunlight and store sensible heat. When the temperature of PCM reach its melting point, it start melting and store latent heat energy. At this stage, PCM contain both sensible and latent heat energy. The PCM, upon cooling, provides this energy with minor heat losses. The cell, keeping PCM, is well insulated and could store heat for 8 hours after charging. Beside this, smaller heat cells are also designed for use in insulated stove. So heat is stored by cells at the day time and could be used at the night time for heating and cooking purposes.

KEYWORDS: *Renewable Energy, Phase change Materials, Solar heat Cell, Thermal Energy, Latent Heat, Sensible Heat*

1. Introduction

A substantial amount of energy is required for cooking all over the world. Mostly this energy comes from fossil fuels, electricity or woods which are very costly. Beside the high cost, both the fossil fuels and woods are environmentally unfriendly and using woods for cooking causes rapid deforestation at the rate of 16 million hectares per year [1]. So if we switch our cooking toward solar thermal, we could reduce pollution and save energy. Temperature of the sun is 6000° centigrade and solar intensity reaching the earth is ranging from 300 to 1100 watts/m² for different countries at different times of the day [2]. If this energy is utilized in cooking and other domestic applications, we could have a considerable decrease in fuel consumption. Solar cooking method is energy proficient and atmosphere friendly having no emanation of Chlorofloro Carbon "CFC". Passing on an estimation, the energy consumed by developed countries in producing food items is 8-16 % of total annual energy consumption [3]. So by means of solar system we be able to have 16 % decrease in power consumption per annum. It gives us a cleaner, drier, more comfortable environment with no fuel consumption or no electricity. The only difficulty in solar system is that it's only working in the day time and cannot be used in the absence of light. Solar insulation for a particular sunshine duration was first proposed by Angstrom and is given as [4].

$$\frac{H}{H_o} = a + b\frac{S}{S_o}$$

The largest and free energy source of earth is the sun. Research reveals that 4 million Exa joules of energy reach the surface of earth annually of which 5×104 EJ of energy is harvestable [5]. The energy received per meter square of earth, called solar irradiance is 342 Wm^{-2} of which around 30 % is reduced by scattering and reflection [6]. Energy received after scattering is called diffused solar radiations [7]. The remaining 70 % energy, called direct radiations, can be harvested in the form of solar thermal and solar photovoltaic energies [8]. A lot of new technologies are in practice to harvest this energy and are called renewable energy technologies. Despite of the huge harvestable energy potential of the solar, its contribution toward global energy mix is negligible. The main focus of this research is to design, fabricate and test solar heat cells with phase change materials capable of storing heat in the availability of sunlight and to deliver that heat in the absence of sunlight. Solar photovoltaic (PV), solar thermal (ST) and concentrated solar power (CSP) are technologies used for harnessing solar energy. Each of these technologies use different component of sunlight. The daily, annual, monthly and seasonal data of a region and the type of energy requirement decide which is good for PV whereas the regions with direct irradiations are suitable for ST and CSP [9].

Solar energy potential of a specific region is proportional to sunshine hours, longitude, latitude and weather conditions of that region. In Pakistan, the sunshine hours are from 6 to 4 PM and the solar irradiation is estimated from 4.4 to 6 Kwh/ m² with average of 5.3 kwh/m² [10]. Raja and Twidell estimated total and diffused irradiation data of 40 stations of Pakistan. He subtracted diffused irradiation values from total irradiation values and calculated the direct solar irradiations value for those stations. Finally the average of daily diffused irradiation for a year were calculated to be ranging from 1.11 to
3.05 Kw/ m² with maximum values for summer and minimum for winter. Whereas the average value of daily direct solar radiation for a year were calculated to be ranging from 1.94 to 3.33 kWh/m² [11]. Solar cookers, being environmental friendly are used for cooking since several decades for harnessing solar irradiant energy. Box type solar cooker was the most common among them and was extensively

studies and modified since eighties. The cooker was easy to manufacture, low in cost but was very time consuming during cooking [12]. Box type cooker was then added with several reflector but cooking has must to be done out door and was slow. After this, parabolic cooker were used for fast cooking but they were also limited to the availability of sunlight and were hazard due to focused sun beams [13]. Split system solar cooker was proposed which has collector outdoor and cooking section inside the kitchen, with the pipes carrying the heat from collector to cooking section [14]. To increase the heat transfer rate, the cooker was added with collector having vacuum with heat pipes where heat was transferred by refrigerant [15]. For water purification, and hot water system, solar stills with phase change material (PCM) were used which showed significant

increase in performance [16]. Finally, concentrated solar cooker with good heat storing materials called PCM was selected for cooking. The selection of heat storing materials was based on heat storage density, durability, heat density and heat transfer rate .The concentrated light beam was provided by solar collector having good reflection [17].

Later on sun-tracking system was provided to the collector. Despite of providing concentrated heat flux for prolonged time, the cost of the cooking system was increased and the cooking, being outside the kitchen, was not easy. This type of cooking was feasible only for boiling food items. So a system of solar cooking was required which could be used even in the absence of sunlight and inside the kitchen. So to fulfill the above conditions, a parabolic dish, with inside reflective surface is used for collecting solar beam at the focal point of the parabola and a cell is designed with PCM inside the cell. The function of the collector is to focus light beam on the cell while the function of the cell is to store energy inside it. After placing the cell at the focal point, the PCM inside the cell will store heat energy from sunlight and will be charged. The cell can then be used for cooking purposes. PCM are studied over last four decades and a number of materials including paraffin waxes, organic compound, non-organic compound hydrated salts and polymers are considered to possess heat storage potential. Division of PCM is based on temperature and physical state [18].

Table 1. PCM classification based on temperature

Low temperature PCM	Here phase transition temperature is below 15 °C. These materials is mainly used in air conditioning systems.
Medium temperature PCM	Here temperature range is 15-90°C. These materials are mainly used in medical, textile and electronic industries.
High temperature PCM	These materials are used for application requiring temperature above 90 °C. For example, cooking, aerospace industry etc.

Table 2. PCM division based on its physical state [19].

Gas-liquid	Here liquid to gas and vice versa conversion take place.
Solid-solid	Here phase of material is not changed. Only the crystalline form of materials is changed.
Solid gas	These materials need large volume. Hence limited in application.
Solid-liquid	Here phase of materials is changed from solid to liquid and vice versa.

Finally an in-organic mixture of KNO3 and NaNO3, having the potential for energy storage was selected in the ratio of 40 to 60% respectively [20]. The mixture of KNO3 and NaNO3 has a melting point of 220°C [21]. The reasons for selecting these materials are its high latent heat of fusion, high specific heat, good thermal conductivity, stable at high temperature, cheap, non-corrosive and stable up to a temperature of 500°C [22].
The thermal energy storage is achieved by heating and melting the PCM materials and the release of energy is achieved by solidifying the materials. Energy can be stored in the following ways.

Latent heat energy can be stored at nearly isothermal conditions and over a narrow range of temperature [23].

$$Q = \int_{T_i}^{T_m} mC_p dT + ma_m \Delta H_m + \int_{T_m}^{T_f} mC_p dT \qquad (2)$$

$$Q = \int_{T_i}^{T_f} mC_p dT = mc_p(T_f - T_i) \qquad (3)$$

11

Mixture of KNO3 and NaNO3 can store both sensible and latent heat energy [24]. Initially, the temperature of the mixture increases and store sensible heat energy. After some time, the temperature remains constant and only state of the mixture changes from solid to liquid. Here mixture of PCM stores latent heat energy.
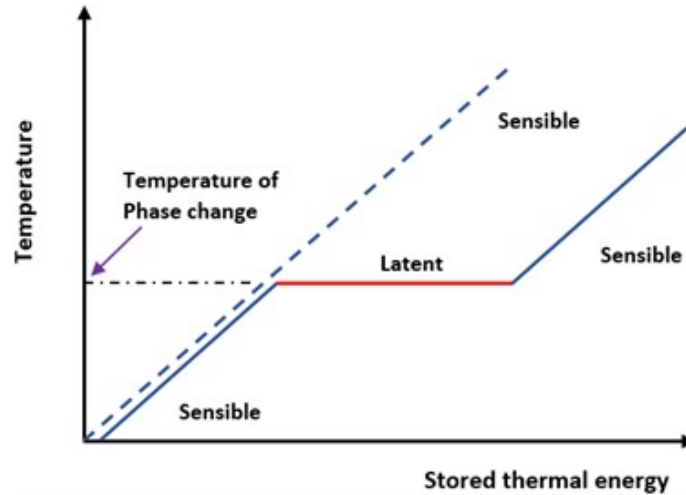
Figure 1. Thermal energy- Temperature Graph

The purpose of this study is to design, fabricate and test a solar heat cell capable of storing renewable energy in the form of solar thermal energy at the day time and to deliver that energy at the night time. The main purpose of the project is to make the solar energy able to be used at the night time when the sunlight is not present. This is achievable only when we store the heat and then use this heat for cooking and heating purposes. So, a composition called solar heat cell is made for storing heat. This cell is able to store heat during sunlight hours (called charging of cell) and to provide that heat during nighttime (called discharging of cell). This cell contains special chemicals called phase change materials. These materials have the ability to store heat energy for a long time and provide heat when needed. These materials have high melting point of about 217 degree centigrade. The cell is placed in specially designed parabolic collector for charging. This structure focuses sunlight on cell. After placing the cell in parabolic collector, the temperature of the materials reach to its melting point and its phase changes from solid to liquid. Here cell stores latent energy. When cell is fully charged, it is removed from the

Parabolic collector. Now heat is stored in cell for 8 hours.Energy stored in the cell can be used for cooking and heating. When the cell is used for cooking the temperature of cell start to reduce. Thus state of materials changes from liquid to solid again so called phase change materials. Consequently, upon charging, the state of materials is changed from solid to liquid and vice versa.

1. Methodology

The aim of the project is to design a cell capable of storing heat energy required to boil a cup of water with some basic calculations. The required energy is planned to be gained from concentrated sunlight at the day time and to be stored by PCM in the cell for use in the absence of light. The amount energy and PCM is calculated by heat transfer formula. The concentration of light is ensured by a parabolic dish called solar collector. The time required by the cell to store heat energy, called charging of the cell, is also calculated both mathematically and experimentally.

2.1 Cell design

A larger and some smaller heat cells are designed to store heat energy. The amount of energy required to boil a cup of water is calculated from the formula $Q = mc\Delta T$ and found to be 47k joules and the mass of materials required is also calculated from the same formula and is 486 grams [23]. The volume

of PCM is calculated from its mass by a formula $\rho = m/v$ and found to be 275 cm³. A cylinder is designed

according to volume of PCM. The top of the cylinder is made of copper and painted with black chrome to increase heat absorption. 5 rods are attached to the back of the top to insure proper heat transfer toward and away from PCM. To avoid heat loss, the cylinder along with its top is insulated by fiber wool and thermal flask. A temperature sensor is installed at the bottom of the cell to display the PCM temperature. Moreover, smaller cells are also fabricated and are used for general cooking purposes in insulated stove.

Figure 2. Solar Heat Cell   **Figure 3**. Head of cell with Inserting Plates
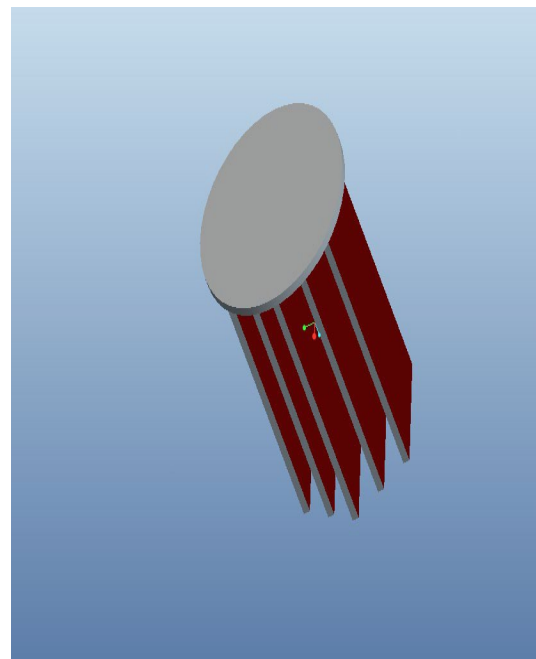
Figure 4. Smaller heat cells

Figure 5. Solar stove

Table 3. Specifications of cell

Volume	275 cm^3
Diameter	6 cm
Height	10 cm
Top absorbing plate	Copper
Coating of top absorbing plate	Black chrome/ nickel/black paint
Insulating material	Ceramic wool and vacuum flask around the cell
Material of rods	Copper
Separations between rods	0.95 cm

2.2 Solar connector

This part is used to provide concentrated heat energy to the cell. It is actually a parabolic dish with aluminum covering. It concentrate light on the cell.

Figure 6. Parabolic Trough

The collector with 40 % efficiency, drops the power to 120 watts/m². According to the formula $t = \frac{Jouls}{power}$ time required to charge the cell is found to be 16 minutes [25].

2. Heat source in the cell

After designing the cell, arrangement is done for storing heat in the cell from sunlight. It is found that, at the average 600 watts/m² of power is available when the sky is clear and at cloudy weather this power drops to 300 watts/m³ [26] . So calculations are done for 300 watts/m².This power is focused on the top of the cell by using a parabolic collector plate. The parameters of collector plate are designed by the formula [27].

$$f = \frac{D \times D}{16d} \qquad (4)$$

Table 3. Specifications of solar collector

Diameter (D)	1.5 m
Depth (d)	.39 m
Focal Length (f)	.36 m

2. Fabrication & Testing

The project consists of cells and collector plate. The fabrication of each section consists of the following sections.

2.1 Cell Fabrication

Stainless steel container was selected for the cell and was filled from mixture of NaNO3 and KNO3. The head of the cell, made of copper, along with its inserting plates was placed on the top of cylinder and was welded on it. A temperature sensor was also installed at the bottom of the cell. External walls of the cell were insulated by fiber wools and a thermal flask.

2.2 Solar collector installation

A parabolic trough was selected to focus sunlight on cell. The trough was illuminated by aluminum sheet to increase the reflectivity of light. The focus point of the parabolic trough was specially designed for placing the cell.

2.3 Testing

The cell was placed at the focus point of the parabolic trough in sunlight and the results were obtained for different hours of the day.

Table 5. Cell Testing

Time	Solar intensity (W/m^2)	Solar intensity After 60% optical loss in solar collector (W/m^2)	Cell Charging Time in minutes $t = \dfrac{Jouls\ required\ i.e\ 4700}{Power\ available(solar\ intensity)}$	Cell Charging Time after heat loss (Minutes)
08:00	303	121	6	24
09:00	486	194	4	16
10:00	746	298	2.7	11
11:00	1050	420	2	8
12:00	1075	430	1.8	7.5
13:00	948	379	2	8
14:00	770	308	2.5	10
15:00	505	202	4	16

3. Conclusion

The current study shows the active and passive TES technologies which can be utilized in the building sector. It also highlights the main advantages and drawbacks of each technology, including the materials used for sensible, latent and thermochemical heat storage. Some of the important parameters of the cell are durability, low capital and maintenance cost, easy to manufacture, small charging time, can provide heat for 3 hours etc. Through investigations, it is estimated that the cell was successfully charged in 8 minutes during solar peak hours but the theoretical or calculated time is 2 minutes. The time difference occurred due to convection and conduction hat losses. Similarly, transfer of heat from the cell to the food items take some additional time due to heat losses.

NOMENCLATURE

H	Monthly average of daily insulation on horizontal surface
HH_{JJ}	Monthly average of daily extraterrestrial insulation on horizontal surface
S	Daily sushine hours
S_o	Maximum possible dailysushine hours
Q	Quantity of energy stored
m	Mass of PCM
Cp	Specific heat capacity
dT	Temperature difference

REFERENCES

[1] U. Prasanna and L. Umanand, "Modeling and design of a solar thermal system for hybrid cooking application," *Applied Energy,* vol. 48, pp. 1740-1755, 2011.

[2] T. SK and . W. S, "Exergy analysis and parametric study of concentrating type solar collectors," *International journal of thermal sciences,* vol. 46, no. 12, pp. 1304-1310, 2007.

[3] T. J. &. M. Hager, " Energy consumption during cooking in the residential sector of developed nations," *Food Policy,* vol. 40, pp. 54-63, 2013.

[4] L. Wong and k. Chow, "Solar radiation model," *Applied energy,* vol. 69, no. 3, pp. 191-224, 2001.

[5] I. E. Agency, "World energy outlook," International Energy Agency, 2012. [Online].

[6] M. Hart, "The troubling science, economics, and politics of climate change," in *Hubris*, 2015.

[7] O. Tzuc, "Environmental-economic optimization for implementation of parabolic collectors in the industrial process heat generation," *Journal of Cleaner Production,* vol. 242, 2020.

[8] F. Ma and P. Zhang, "Performance investigation of the direct absorption solar collector based on phase change slurry," *Applied Thermal Engineering,* vol. 162, 2019.

[9] S. C. and S. Stokler, "Solar resource mapping in Pakistan," The World Bank, 2015.

[10] I. Ahmad and P. Akhter, "Solar radiation over Pakistan," *Applied solar energy,* vol. 31, no. 3, pp. 41-50, 1995.

[11] A. Raja and W. Twidel, "Distribution of global insolation over Pakistan," *Solar Energy,* vol. 43, no. 6, pp. 355-357, 1989.

[12] K. Schwarzer and d. silva, "Characterisation and design methods of solar cookers," *Solar energy,* vol. 82, no. 2, pp. 157-163, 2008.

[13] . A.-S. Mohammed and . S. . A. Essam, "A parabolic solar cooker with automatic two axes sun tracking system," *Appl Energy,* vol. 87, p. 463–70, 2010.

[14] K. j, M. Taha and A. Mannaa , " A split-system solar cooker with heat pipes," *Energy Convers Manage,* vol. 26, no. 2, p. 259–64, 1996.

[15] E. Mehmet , " Thermal performance of a solar cooker integrated vacuum-tube collector with heat pipes containing different refrigerants," *Solar Energy,* vol. 76, p. 751–7, 2004.

[16] M. Kawi and N. NM, " non conventional solar stills with energy storage element. Desalination," *Desalination,* vol. 153, no. 1-3, pp. 71-80, 2003.

[17] B. Zalba and J. Marin, "Review on thermal energy storage with phase change: materials, heat transfer analysis and applications," *Applied Thermal Engineering,* vol. 23, p. 251–83, 2003.

[18] M. Liu, w. Saman and F. Bruno, "Review on storage materials and thermal performance enhancement techniques for high temperature phase change thermal storage systems," *Renewable and Sustainable Energy Reviews ,* vol. 16, no. 4, pp. 2118-2132., 2012.

[19] A. Abhat, "Low temperature latent heat thermal energy storage. In: Thermal energy storageheat storage materials," *Solar energy,* vol. 30, no. 4, pp. 313-332., 1981.

[20] M. Liu , W. Saman and F. Bruno, "Review on storage materials and thermal performance enhancement techniques for high temperature phase change thermal storage systems," *Renewable and Sustainable energy Review,* vol. 16, p. 2118–2132, 2012.

[21] F. Roget and C. Favotto, "Study of the KNO3–LiNO3 and KNO3–NaNO3–LiNO3 eutectics as phase change materials for thermal storage in a low-temperature solar power plant," *Solar Energy,* vol. 95, p. 155–169, 2013.

[22] R. Bradshaw and D. Meeker, "High-temperature stability of ternary nitrate molten salts for solar thermal energy systems," *Solar Energy Materials,* vol. 21, no. 1, pp. 51-60, 1990.

[23] L. and A. George, Solar heat storage: latent heat materials, 1983.

[24] L. Gabriela, "Thermal Energy Storage with Phase Change Material," *Leonardo Electronic Journal of Practices and Technologies,* no. Issue 20, pp. 75-98, 2012.

[25] L. and E. Bradley, "A comparison of energy densities of prevalent energy sources in units of joules per cubic meter," *International Journal of Green Energy,* pp. 438-455, 2008.

[26] S. Tyagi and S. Wang, "Exergy analysis and parametric study of concentrating type solar collectors," *International Journal of Thermal Sciences,* vol. 46, p. 1304–1310, 2007.

[27] J. S. and . P. Hu, "Optical modeling for a two-stage parabolic trough concentrating photovoltaic/thermal system using spectral beam splitting technology," *Solar Energy Materials and Solar Cells ,* vol. 94, no. 10, pp. 1686-1696, 2010.

THERMAL RUNAWAY AND FIRE SUPPRESSION
FOR ELECTRIC VEHICLE BATTERIES

C. Un[1*], K. Aydin[2]

[1] *Çukurova University, Automotive Engineering Department, Adana, Turkey.*
[2] *Çukurova University, Mechanical Engineering Department, Adana, Turkey.*
*cagri_un@hotmail.com

ABSTRACT

Electric vehicles (EV) and their batteries are becoming a far larger business than most realize. Lithium-ion batteries (LIB) are the clear winner, with only a few percent of their business threatened by alternatives such as other advanced batteries and super capacitors even in 2030. To understand that, the whole opportunity from land, water and air to hybrid and pure electric vehicles must be reappraised. The largest market for lithium-ion batteries is and will remain electric vehicles, mainly cars, from 2020-2030. In these applications they almost always have the best compromise of performance, cost, weight and size. However, there are surprises revealed when a careful, fact-based analysis is carried out. In 2030, the EV market leaps to over $3 billion but with cars losing share and burgeoning demand for much smaller and much larger battery packs than those used in cars.

Different kind of LIB's are presenting as energy storages for the automotive industry. The kinds of LIB's divide into cylindrical and prismatic, whereas the prismatic type can be further divided according to the housing stability into hard-case and the pouch type

. However, the fire problems have become a major safety concern with the use of lithium-ion batteries in the automotive industry. Thermal runaway of lithium-ion batteries is particularly dangerous in systems where runaway can propagate through many cells. To understand thermal runaway propagation in these systems, it is important to understand the differences between failure characteristics of the initial cell that fails due to an abuse event and subsequent cells that fail due to thermal runaway propagation. This work compares thermal runaway events for single cells failed using a heater with cells failed due to propagation in an array. Also this study focuses on the fire suppression issues of EV's related to thermal runaway and fire in LIB's. This work also attempts to develop a quantitative understanding of fire suppression mechanisms of water to LIB's. Therefore, this paper provides a comprehensive research on the thermal runaway and fire suppression mechanism of the commercial lithium ion battery for electric vehicles.

Keywords: Vehicle Fire Suppression, Lithium Ion Battery, Thermal Runaway, Electric Vehicle

1. INTRODUCTION

In a fire, the material being burnt is undergoing a rapid oxidation with the evolution of heat and light. The phenomenon is called combustion and oxygen from the air, O_2, is by far the most common oxidant, but oxidizing chemical substances such as nitrates, chlorates and peroxides can also be the oxidant and should not be stored next to combustible materials. The chemistry occurring in a flame is very complex, and involves free radical chain reactions, and the overall reaction is very exothermic. When organic compounds undergo complete combustion the major products are carbon dioxide and water, but normally in fires complete combustion does not occur and fine solid material, smoke, and other gaseous material is given off [1].

The first component of the combustion triangle is fuel. There must be sufficient fuel present in the air to form an ignitable mixture. The fuel may be in the form of a gas, vapor, mist or dust. The second component of the combustion triangle is oxygen. For combustion to occur oxygen is necessary only at normal concentrations present in the air we breathe. The ignition sources are perhaps the most variable and unpredictable. For electrical equipment this may be from an arcing or sparking device or from a hot surface. There may be sources of ignition other than electrical equipment, such as hot exhaust surfaces from internal combustion engines. Essentially all three elements must be present for fire to occur. Removal of fuel or oxygen will result in the fire being extinguished, if the fire itself is considered as a source of ignition, then, the removal of ignition source also will result in the fire

being extinguished. Further fire research determined that a fourth element, a chemical chain reaction, was a necessary component of fire. The fire triangle was changed to a fire tetrahedron to reflect this fourth element [2].

The catastrophic loss of a battery cell can result in even more severe consequences such as damage to other system elements, and/or human injury or death. Failure of a cell may be the result of poor cell design or manufacturing flaws, external abuse (thermal, mechanical, electrical), poor battery assembly design or manufacture, poor battery electronics design or manufacture, or poor support equipment (i.e. battery charging/discharging equipment) design or manufacture. The primary battery risks are generally a result of external or internal short circuits, high or low temperatures, overcharge or over-discharge. These mechanisms can result in exothermic reactions within the battery. When temperatures become sufficiently high, or there is an ignition source present that ignites the flammable gases released by the battery. Figure 1 shows the combustion triangle theory was used to explain the battery fire and explosion.
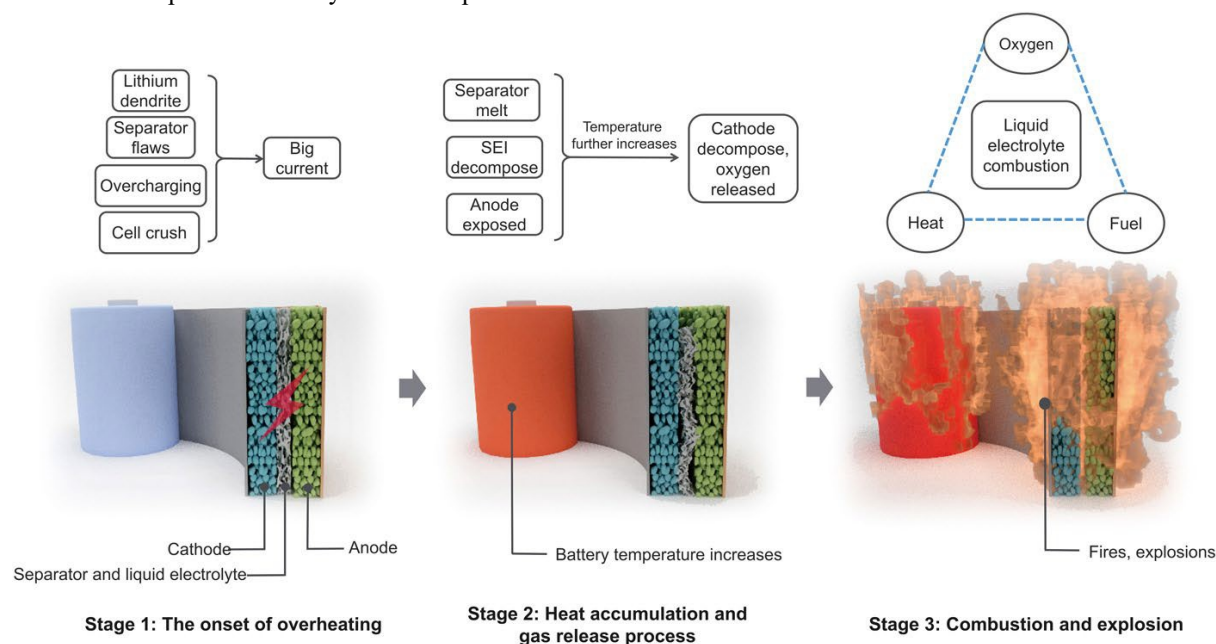

Figure 1. The fire triangle for lithium-ion batteries [3]

1.1. Battery Technology

Advancements in battery technology and the electrification of the automobile have contributed enormously to the changing technological landscape we see all around us. Today, the race is on between different battery technologies to claim the top spot in a variety of applications. Ultimately, it is those applications and the fit between battery technology/chemistry and the requirements demanded by that application that will determine the victors of this war.

To better understand and forecast the coming changes within the battery market over the next decade specifically, LIB chemistries used in electric vehicles. In this paper; relevant battery chemistries and their technological evolution looked at by analyzing academic research, patents, and an overview of the commercial landscape. This analysis with an overview of external factors that will drive battery adoption, namely the cost evolution of key raw materials, supply/demand projections, and investments in the space from key players and governments are coupled.

Analysis forecasts that by 2030, lithium iron phosphate (LFP) batteries will have the largest share of LIBs used in electric vehicles. This evolution will be the result of a close contest between LFP and lithium nickel manganese cobalt oxide (NMC) type chemistries, which may ultimately be decided by the preferences of China, whose large investments in LFP and the LFP manufacturing supply chain may tip the balance in favor of this chemistry [4].

Commercially available lithium-ion battery cells can be divided based on their structure and appearance into cylindrical and prismatic cells. Cylindrical cells are hard-case cells, while prismatic cells can either be hard-

21

case rectangular prisms or so-called pouch cells with a soft, bag-like structure. Specifics of manufacturing process of different builds of lithium-ion battery cells with focus on the efficiency of the production cycle showed that limitations of pick-and-place assembly are described as the main bottleneck in automotive production [5]. Figure 2 shows different commercially available cell types and their module designs with the suitability of different joining methods of electrical contacts.
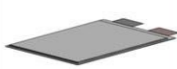
Figure 2. Commercially available cell and module types with electrical contact joining methods [6]

Cylindrical cells have a very high mechanical stability as their shape distributes forces, due to internal pressure increase, evenly over the circumference. Their shape makes it however harder to package them together in an efficient manner as a significant amount of space is lost when arranging them in a rectangular shape. This, however, make it easier for air to flow freely around a group of cylindrical cells resulting in easier thermal management.

Prismatic cells are commonly used for automotive traction batteries. Their prismatic shape makes them easier to integrate in a battery pack than cylindrical cells. This can make it more challenging to regulate their temperatures. The contents of prismatic cells follow the principle for cylindrical cells. Instead of rolled up, several layers of current collector packages are put on top of each other. As a result, prismatic cells tend to be tightly packed, which results in relatively high mechanical stresses on the prismatic package [7].

Pouch cells store their content inside a flexible foil pouch rather than inside a rigid container. In this case, the current collector assembly is stacked inside the pouch package, rather than rolled. This gives most of the space inside the package to be used for electrochemical material and thus allows for a high energy density per pouch cell. Their flat shape also allows for very high packaging efficiency of 90-95% when it comes to integrating them in battery packs. As a result, temperature management also becomes more important for this cell type, as it is more difficult to dissipate heat. Their soft construction can also be a drawback as it makes them vulnerable to external mechanical damage. Furthermore, pouch cells require a support structure as they are not mechanically rigid [8].

Generally, LIB possesses stable structure in which lithium ions transfer between the cathode and the anode during charging/discharging such that it can be regularly cycled considerable times. Whereas, the original stable-structure of the LIB will became damaged due to the effect of abusive factors, generating thermal hazard. The factors can be summarized as several main types: physical, electrical and thermal factors, as well as manufacturing defect and battery aging.

The destructive deformation of battery caused by an applied force is a common feature of physical factor. Where, vehicle collision/crash and penetration of battery are the typical conditions for physical failure. Furthermore, the volume expansion of electrode materials and stress generation within battery may also lead to physical failure.

It reveals that during an accident involving the vehicle; it is possible for a single battery or a battery pack to deform under the effect of an external force. The deformation of battery may result in dangerous consequences;

(1) the electrodes can come into contact causing an internal short circuit

(2) the flammable electrolyte leaks which may induce a fire [9].

As known, the compressive stress reached during lithiation and the tensile stress reached during delithiation are significant inside battery. Such large stress cycling over extended lithiation/delithiation cycles will invariably lead to fatigue damage, leaving battery materials susceptible to fracture and pulverization. Moreover, traditional electrode materials, such as silicon and transition metal oxides, may result in extreme volume changes during operation and further result in fracturing, electrical conductivity loss and mechanical integrity[10].

External short circuit, overcharge and over-discharge are common conditions of electrical failure. Where, the external short circuit of battery occurs once electrodes with a voltage difference are connected by conductors. It usually results from the deformation of battery, water immersion, conductor aging, improper usage and long-time charging, etc. During an external short circuit, the battery is in a state of fast discharging and the discharging current may be much larger than that of normal condition. Hereafter, the battery undergoes a violent temperature rise which may lead to serious consequence. As the open circuit voltage of battery is charged above the cut-off voltage, overcharge occurs. The failure of battery management system is the ordinary reason of overcharge so that the charging of battery will proceed continuously. As a result, the internal pressure of battery increases, the deformation of battery and leakage of electrolytes occur, and the performance of battery also significantly decreases. Besides, severe heat and gas generation can also be seen during overcharge process. Compared to normal charging process, the heat generation behavior during overcharge will be much greater as a result of the side reactions inside battery and the increased internal resistance. In addition, excessive loss of lithium ions at the cathode during overcharging will lead to structural collapse of the cathode and subsequent oxygen release. The released oxygen accelerates the decomposition of electrolyte, and thereafter, gases are generated. Consequently, the thermal hazard associated with an overcharged battery is greatly heightened compared to that of a normal battery due to the excessive energy stored in the overcharged battery.

Besides the overheating caused by physical or electrical factors, thermal failure can also be triggered by external high temperature and overheating. Thermal factor results in a fierce rise of battery temperature, the melting of separator, the decomposition of electrodes/electrolytes and numerous side reactions etc., and finally leads to battery thermal runaway. In other words, thermal abuse is the root cause of battery thermal runaway. It should be noted that both physical and electrical factors also ultimately cause thermal runaway. Further, it can be found that almost all the abusive conditions are accompanied with internal short circuit, i.e., an internal short circuit is the most common feature of thermal runaway. It occurs when the cathode and the anode contact with each other due to the failure of battery separator. Once the internal short circuit is triggered, the electrochemical energy stored inside the battery spontaneously releases, generating large amounts of heat [9].

After thermal runaway has initiated, smoke is released from the safety valve or through cracks in the battery shell. This smoke consists of a mixture of flammable and toxic gases. The flammable gases could be ignited by nearby ignition sources such as fire, sparks, and electrical arcs or may even be self-ignited due to a poor cooling condition. The resulting flame may then further heat the battery. If the release rate of gas out of the battery shell is lower than the internal gas-generation rate, the battery cell may also burst. The safety valve can release some of the accumulated gas that are typically generated during the pre-ignition thermal runaway process, but it may not be able to prevent the cell from external heating, such as flame radiation or a burning battery nearby. In addition, if the released gas is allowed to accumulate in an enclosed area and mix with surrounding oxygen, a gas explosion may occur once a pilot source like a spark and flame is present [11].

To stop a fire, one of the three elements of the fire triangle must be removed. So, if a fire runs out of fuel, it will smolder out; if you can cool a fire down it will lose heat and go out; and if the oxygen is removed it will suffocate. Therefore, attempts at combating a fire and also preventing a fire are based upon these principles. Fire extinguishers are developed to eliminate one of the three elements such as water fire extinguishers which cool the fire down and remove any heat.

By the same codes of practice, fire prevention methods are also developed in relation to the chemical reaction which occurs when fire takes place. Undertaking safety steps such as storing flammable liquids away and making sure piles of paper or fabric are not left near any possible heat sources are highly important.

By using this fundamental fire safety knowledge, the prevalence of fires and the damage they cause can be significantly reduced.

2. CONCEPT DESIGN

For this study, different types of LIB were fired with propane gas burner and these batteries were extinguished with water.

2.1. Fire Suppression with Water

Experiences on battery fire suggest that the primary effort of suppressing the EV fire is to cool down the temperature of the battery which is already in the thermal runaway state.

The function of water is simply to cool the burning fuel. Water is cheap, and can be directed on to the seat of a fire by a high pressure. Buildings are provided with sprinklers which operate automatically if the temperature rises above a certain value. Risers are vertical pipes in buildings to which a high pressure water supply may be attached at ground level. The cooling action of water is mainly due to its heat of vaporization. The molar heat capacity of liquid water is 75 J/mol K and its specific heat capacity is 4.18 J/g K. Thus a liter of water would absorb 313 kJ of heat in going from 25 °C to 100 °C. But its molar heat of vaporization is 42 kJ/mol or a liter of liquid water at 100 °C would absorb 2300 kJ on completely vaporizing.

Water should only be used on Class A fires, solid fuel. Most organic liquids have a lower density than water and will float on top and keep burning. Spattering of drops of burning liquid can also occur. Where electrical equipment is involved water can cause shorting resulting in sparks which could ignite material, and in material becoming electrically live. Reactive metals like sodium react vigorously with water at ambient temperature to produce combustible hydrogen, and less reactive metals such as aluminum also react in highly exothermic reactions at higher temperatures:

$$2\ Al(s) + 6\ H_2O(g) \rightarrow 2\ Al(OH)_3 + 3\ H_2(g) \tag{1}$$
$$2\ H_2(g) + O_2(g) \rightarrow 2H_2O(g) \tag{2}$$
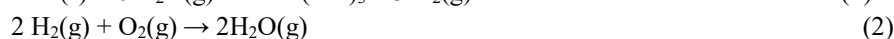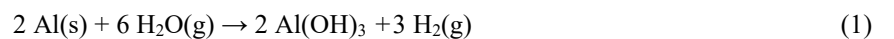
The simplest water fire extinguisher is a hose connected to a high pressure water supply. Fire hoses must be able to deliver 14 liters per minute and the pressures required for this are 225 kPa for 13 mm hose and 150 kPa for 19 mm hose. Water type portable extinguishers used to be activated by turning them upside down, this causing sulfuric acid to mix with sodium bicarbonate releasing carbon dioxide to provide the necessary pressure. These are now banned. Modern extinguishers are simply pressurized with enough nitrogen gas to drive out the water or have a cartridge containing a very volatile liquid, usually carbon dioxide. To activate the extinguisher the cartridge is opened in some way and the evaporating liquid provides the necessary pressure to drive out the water[1].

2.2. Lithium-ion Batteries

Lithium-ion battery is a type of rechargeable battery where the ions move from negative electrodes to the positive electrode during discharge and come back upon charging. Li-ion batteries are commonly used in home electronics which require high energy density, tiny memory effect and low self-discharge. Li-ion batteries are being widely adopted in electric vehicles, grid level energy storage solutions and for military as well as aerospace applications. Moreover, lithium-ion batteries have become a constant replacement for the lead–acid batteries.

Li-ion batteries are composed of four main components namely cathode, anode, electrolyte, and separator (Figure 3). Lithium-ion battery generates electricity because of continuous reactions of lithium.

Cathode: A cathode determines the capacity and voltage of a Li-ion battery. The cathode of a Li-ion battery is lithium oxide, since lithium is unstable in the element form. A thin aluminum foil holds the frame of the cathode, which is coated with a compound made up of active material, conductive additive and a binder. The active material contains lithium ions, the conductive additive is added to increase conductivity and the binder acts as an adhesive which aids the active material as well as the conductive additive to settle on the aluminum substrate.

Cathode plays an important role in determining the characteristics of the battery as the capacity and voltage are determined by the type of active material used for cathode. The higher the amount of lithium, bigger the capacity and the potential difference between cathode and anode, and higher are the voltage. The potential difference is small for anode depending on their type. The potential difference for cathode is generally higher and it plays a significant role in determining the voltage of the battery.

Anode: The anode is also coated with an active material that enables the flow of electric current through the external circuit while also allowing the reversible absorption or emission of lithium ions that are released from the cathode.

When the battery is being charged, lithium ions get stored in the anode and not the cathode. When the conducting wire connects the cathode to the anode in the discharge state, lithium ions flow back to the cathode through the electrolyte, and the electrons get separated from lithium ions and move along the wire generating electricity.

Graphite is used for an anode as it has a stable structure. Its properties such as structural stability, low electrochemical reactivity, storage of lithium ions and lower price lead to the wide use of the material for anode. The anode is also coated with active material, conductive additive and a binder.

Electrolyte: Electrolyte is a major component of a Li-Ion Battery as it facilitates the movement of the lithium ions between the cathode and the anode and the electrons move through the wire. An electrolyte is generally composed of chemicals with high ionic conductivity to facilitate the movement of lithium ions.

The electrolyte is composed of salts which enable the passage for lithium ions, the solvents that are organic liquids which dissolve the salts, and additives which are added in small amounts and have specific functions. The speed of lithium ions also depends on the type of electrolytes used. High purity electrolytes are a core component of li-ion batteries. The most commonly used electrolyte comprises of lithium salt, such as lithium hexafluorophosphate in an organic solution.

Separator: While the cathode and anode determine the basic performance of a battery, electrolyte and separator determine the safety of a battery. The separator acts as a physical barrier by keeping the cathode and anode apart. It also prevents the direct flow of electrons and allows only the lithium ions to pass through the internal microscopic hole. Commercialized separators used are generally synthetic resins like polyethylene (PE) and polypropylene (PP) [12].
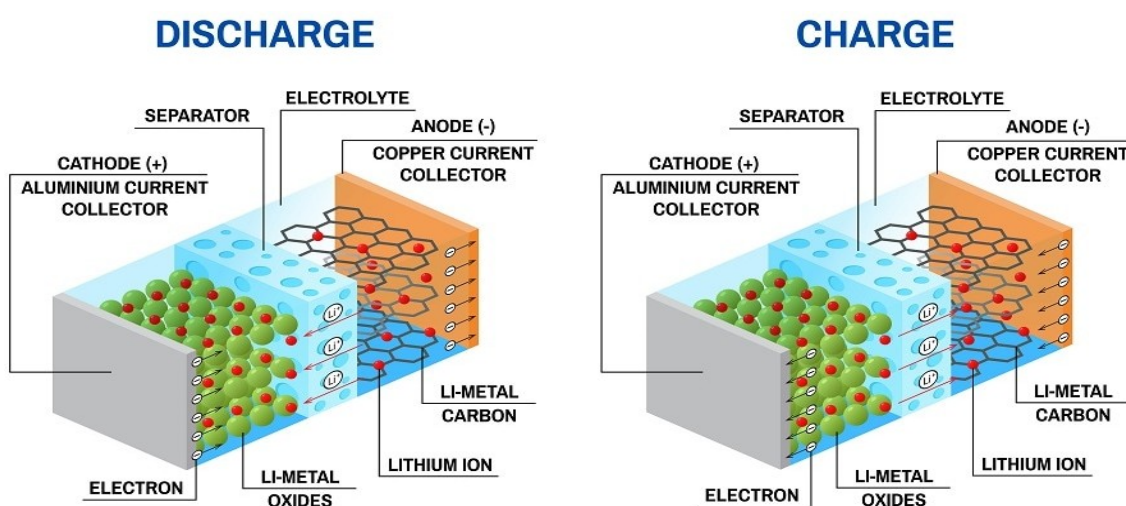
Figure 3. Schematic representation of a lithium-ion battery **[13]**

Lithium cobalt oxide (LCO or LiCoO₂): Lithium cobalt oxide is a chemical compound used in positive electrodes of lithium-ion batteries. It consists of layers of lithium that lie between slabs of octahedral structure formed by cobalt and oxygen atoms. It offers high energy density but presents safety risks when damaged. The performance of $LiCoO_2$ in batteries is related with the particle size of the material and different sizes ranging from nanometer to micrometer sized particles are researched and produced. The drawback of Li-cobalt is a relatively short life span, low thermal stability and limited load capabilities. Li-cobalt should not be charged and discharged at a current higher than it is C-rating. This implies an 18650 cell with 2,400 mAh must be charged and released at 2,400 mA.

Lithium iron phosphate (LFP or LiFePO$_4$): It is an inorganic compound and is either a grey, brown, red or black solid which is insoluble in water. LFP batteries have an operating voltage of 3.3 V, charge density of 170 mAh/g, long cycle life and stability at high temperatures.

Lithium-Ion Manganese Oxide (LMO or MnO$_2$): Lithium manganese oxide batteries have manganese oxide in their cathodes. They come in many widespread lithium sizes.

Lithium Nickel Cobalt Aluminum Oxide (NCA or LiNiCoAlO$_2$): It shares similarities with nickel manganese cobalt oxide (NMC), which offers high specific energy and long-life span. This is a further development of the lithium nickel oxide.

Lithium Nickel Manganese Cobalt Oxide (LiNiMnCoO$_2$ or NMC): It is one of the most successful Li-ion systems and has a cathode combination of nickel-manganese-cobalt. These systems can be tailored to serve as Power or Energy cells. Nickel is recognized for its high energy, but poor stability and manganese has the advantage of forming a spinal structure to attain low internal resistance but offers a low energy. Combining the metals improves each other's strengths.

Lithium titanate (Li$_4$Ti$_5$O$_{12}$ or LTO): Li-titanate has a nominal cell voltage of 2.40 V. It can be fast charged and delivers a high discharge current of about 10 times the rated capacity. It has low-temperature discharge characteristics and is safe [12].

NMC batteries currently account for nearly 28% of global EV sales, and Fitch forecasts that market share of NMC batteries is to grow to 63% by 2027. NMC uses lithium nickel manganese cobalt oxide as the cathode and graphite as the anode. The specific energy density of NMC is 150–220 Wh/kg, with the thermal runaway being 210 °C. The high cost and toxic nature of cobalt is leading battery manufacturers to move toward higher nickel content in cathodes. Compared to cobalt, nickel cells have a lower cost and longer cycle life.

An NMC battery generally has a longer cycle life, more stability, and a higher energy density than lithium cobalt oxide (LCO) and lithium iron phosphate (LFP) batteries. It also has a lower cost of energy because of the ability of an NMC battery to cycle with more stability than an NCA battery. The battery has a high cycle life suitable for both off-grid and very unstable grids, with commercial products featuring a 60% state of charge (SOC) greater than 6,000 cycles at 90% depth of discharge (DOD).

At a certain temperature, the cathode (cobalt in this case) releases oxygen, which makes the cell combustible because of the reaction between the electrolyte and oxygen. For an LFP cathode, the oxygen-phosphorus bond is not broken until 350 °C, whereas this temperature range is much lower for NMC. Hence, NMC batteries are less safe because of the highly toxic nature of cobalt.

NCA batteries are becoming increasingly important in electric power trains and in grid storage because of the recent increment in energy density (>280 Wh/kg), which was previously in the 150-220 Wh/kg range. They are sub classified into cylindrical and prismatic batteries.

NCA batteries require a small amount of active materials yet can deliver a higher energy density. They are also more stable than NMC batteries due to the addition of aluminum. An NCA battery pose safely challenges when compared to LFP batteries, as they are more prone to thermal runways. Another setback is cost, as they are expensive to mass produce due to limited applications.

With operating ranges from -4.4 °C to 70 °C, LFP batteries handle far wider variations in temperature than other chemistries. They also have a slightly higher self-discharge rate and low cell voltage (3.3V). Thermal runaways are less common for an LFP battery, as it doesn't require cobalt. Disadvantages LFP batteries have a lower energy density and last for a shorter time period compared to NMC and NCA batteries.

Lithium iron nano phosphate batteries can be used extensively in applications such as electric and hybrid vehicles and renewable energy generation.

LCO have a high current capability and longer calendar lifespan. It also has a high energy density and an increased safety level when compared to NMC batteries. Its relatively short life span, low thermal stability, and limited load capabilities are likely to act as restraints on demand. This battery chemistry uses manganese as the cathode and graphite as the anode. The LCO (cobalt-only) and LMO (manganese-only) batteries are precursors to NMC and NCA batteries. LMO batteries are usually used along with NMC in electric vehicle.

The operating voltages of LMO's are high compared to LFP batteries. The thermal runaway for LMO is 250 °C, which is relatively higher than NMC and NCA; hence they are touted as being safe. Disadvantages of LMO's have a much shorter lifespan, ranging between 300 and 700 cycles. In addition, their high charge promotes thermal runaway and degrades quickly at elevated temperatures [4].

The experimental phenomena during thermal runaway:
- heating stage
- safety vent opening
- gases releasing
- thermal runaway
- ignition and combustion
- abatement and extinguishment

There are many possible reasons why a battery cell can become hot, e.g. overcharging, short-circuiting, mechanical deformation or external heating. Various degrees of protection can be achieved by such means as battery design and quality.

Incidents involving gas releases, fire and explosion will occur and this is because of, for example:
- External factors such as mechanical impact, e.g. cars that crash and deform the battery, external heating or external fire
- Battery cells are also sensitive to, for example, a charge current that is too high. The current in each cell is therefore monitored by a monitoring system, usually known as a Battery Management System (BMS). It is important to have a high-quality BMS. The BMS cannot, however, offer protection in all cases. Furthermore, the BMS or a sensor can break down and no longer offer protection.
- There can also be a spontaneous internal short circuit. This phenomenon can actually occur at any time, even when batteries are not in use.
- The probability is not well-documented, but it is typically low, with figures in the order of 1 ppm (i.e. 1 cell out of 1 million cells). The reason is still not fully understood, but originates from defects in the manufacturing process combined or not with use (e.g. recurring small overdischarges/overcharges)
- It is difficult in the manufacturing phase to achieve 100% pure material that is absolutely free of contaminants and undesired particles. Leading battery safety experts now believe that manufacturing defects could not be fully avoided, no matter how much money were to be invested. When the battery wears through usage, these risks can also be affected through, for example, dendrite formation.
- Lower quality of cells and of BMS will increase the number of incidents.
- The human factor is also present at all times – incorrect handling, faulty connection, etc.
- Quick-charging can increase the risks, as higher currents are involved, which places tougher demands on, for example, control, detection and cooling.

As incidents cannot be entirely discounted, it is instead necessary to manage their consequences. Mitigating or preventing propagation is typically an important part of the solution. The design is crucial here. Even if it is not possible to stop a fire from spreading completely, it can be valuable to achieve a delay in order to create time for detection, evacuation, implementation and countermeasures and for the emergency services to arrive. Detection, ideally at an early stage, is therefore important.

Commonly, quantities of toxic gases can be generated during the thermal runaway process such as HF, carbon monoxide (CO), nitric oxide (NO), sulfur dioxide (SO_2), hydrogen chloride (HCl) and hydrogen (H_2) [9].

Fire suppression experiments which presented in this study; the technical characteristics of the lithium ion batteries used are given Table 1.

Table 1. Technical characteristics of the batteries used in the experiments

Cell Type	Volume of Electrolyte Per Cell	Number of the Cells Per Module	Weight of the Module (kg)	The Weight of System/String (kg)	Thermal Runaway Temperature (°C)
Type 1, NMC (Pouch)	10-30 % of weight	20/module	28	1232[a]	

Type 2, NMC (Pouch)	10-30 % of weight	176/pack	280 (±5)	2800[b]	200 °C
Type 3, NMC (Pouch)	10-30 % of weight	48/module	81-83	648-664[c]	
Type 4, LTO (Prismatic)	5-15 % of weight	276/pack	260 (±5)	2080[d]	250 °C

[a] 1 string = 4 packs of 11 modules

[b] 1 system of 10 strings

[c] 1 string of 7 modules

[d] 1 system of 8 strings

2.3. Propane Gas Burner

For these experiments; a 400 kW propane gas burner was placed underneath (80 cm) a metallic table on which were placed the cells and was ignited after the start of the test (Figure 4). Li-ion batteries were exposed to an external propane fire. The experiments were performed using an external propane burner for the purpose of heating and igniting the battery cells as described in the experiments.

Figure 4. Propane gas burner

2.4. Methods

For this study, different types of LIB were fired with propane gas burner and these batteries were extinguished with water. These LIB's are NMC (Nickel Manganese Cobalt Oxide) and LTO (Lithium Titanate Oxide) types. Also Li-NCA type cylindrical, 13 kg with plastic pack (Type 5) and Li-FePO$_4$ type cylindrical, 20 kg with plastic pack (Type 6) lithium ion batteries were used for experiments. The tested batteries with NMC and LTO feature are in prismatic and cylindrical in shape.

Thermal runaway issues of the different types of batteries and their extinction with water were observed (Table 2).

In the experiments that were conducted with the collaboration of Çukurova University, The University of Poitiers, The National School of Mechanics and Aerotechnics (ISAE-ENSMA), The Pprime Institute academicians (in Poitiers city of France) and Departmental Fire and Rescue Service of Vienne Region officers. The concept of fire was examined both theoretically and in terms of testing [14].

Table 2. Details of the experiments

Experiment Number	Materials	Objectives
No.1	Type 1-2, Li-ion NMC - Pouch	

No.2	Type 3, Li-ion NMC – Pouch + Type 4, Li-ion LTO - Prismatic	Cells exposed to heat source. The temperature increased during the thermal runaway.
No.3	Type 4, Li-ion LTO - Prismatic	
No.4	Type 1, Li-ion NMC (Pouch) in a package (aluminum and plastic case)	Water effect on module (possibility of water inlet). Cobra type extinguisher was used.
No.5	Type 3, Li-ion NMC (Pouch) in a package (steel case)	
No.6	Type 2, Package of prismatic cells	
No.7	Type 5, Cylindrical Li-NCA with plastic case	Water effect on the scooter module in fire/ examination of the reaction. Cobra type extinguisher was used.
No.8	Type 6, Cylindrical cell Li-FePO$_4$ with plastic case	

3. EXPERIMENT RESULTS

The thermal runaway of a battery is a phenomenon that occurs when it is subjected to very high temperature conditions. A thermal runaway is a rapid internal temperature increase that often results in one or more of the following events: heat generation, gas and smoke formation, cell breach/cell explosion, fire or gas explosion. Gas releases can typically occur at lower temperatures and without the occurrence of a thermal runaway.

In the first of two experiments, with the 400 kW propane gas burner a rapidly progressing combustion was observed for the Li-ion NMC, Pouch cells (Figure 5). Also, NMC and LTO type electric batteries were burned together. It was observed that LTO type prismatic battery burned less (Figure 6).

In the experiment 3; Li-ion LTO prismatic cell less burned. Extinguishing with water by the fireman was not very effective and it was necessary to wait a while for the full extinguishing action (Figure 7).
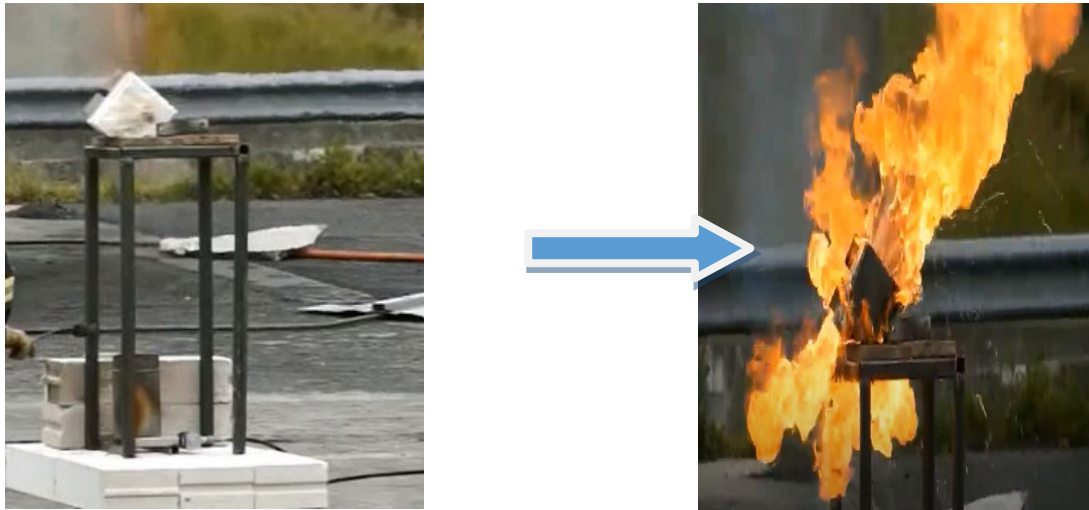
Figure 5. Pouch cells exposed to heat source
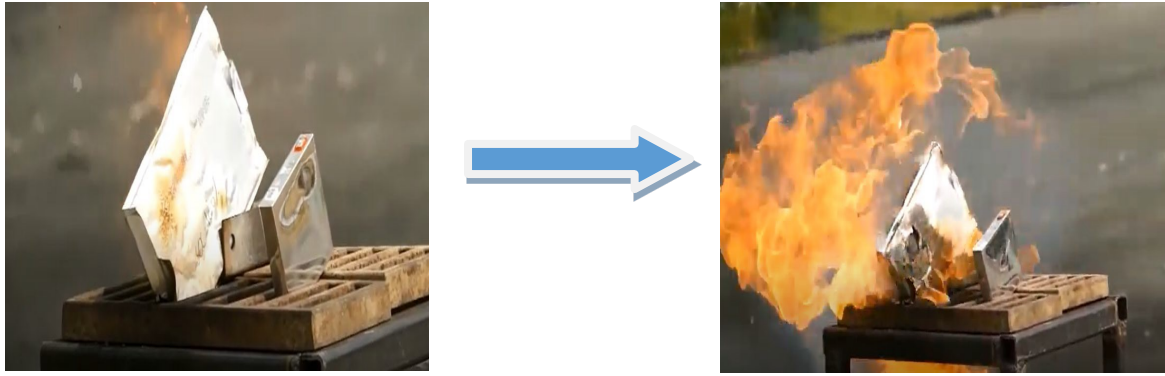
Figure 6. Pouch and prismatic cells exposed to heat source
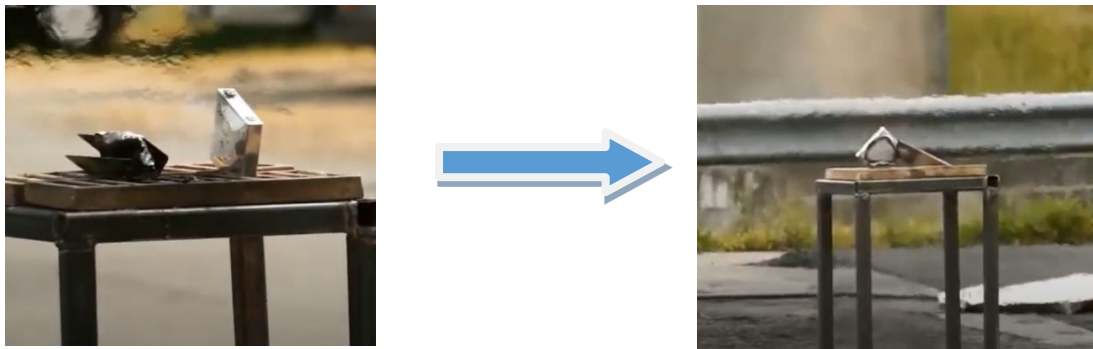
Figure 7. Prismatic cells exposed to heat source

In the experiments (4, 5 & 6) involving module/package of pouch type and prismatic type cells, different reactions were observed according to the type of cells. The pouch cells package with aluminum and plastic coating fire is a fire type with the risk of subsequent revival. After the thermal runaway of the battery, a significant smoke development was noticed (Figure 7). Thermal runaway of the prismatic cells package was accompanied with degradation of prismatic cells inducing a explosion of molten aluminum. The molten parts formation was crucial to send water inside the battery (Figure 8).

On the other hand the need of a high quantity of water as same as for the flexible cells module in the steel coating where the deformation of the pack or the melting of the fusible parts allowed water to be injected into the battery and therefore suppress the fire (Figure 9).

In the experiment 7 and 8, thermal runaway of cylindrical batteries were mainly characterized by the explosion of cylindrical cells. Cylindrical batteries typically have safety vents to enable the release of gases that set up inside the battery and thus help decrease the effects of thermal runaway, including fire and explosion (Figure 10), with regard to the battery used in scooters (2 kWh), three minutes after the first thermal runaway, the fire was brought under control without worry (Figure 11). Abundant white smoke was produced. There has also been a fire involving explosions and rattling.

However, the second thermal runaway which led to a explosion of cells was brought under control four minutes later. This type of fire requires a lot of water for complete extinction. As for the battery used in leisure vehicles, thermal runaway followed three minutes later by repeated explosions with a missile effect. The complete extinction was made nine minutes after the thermal runaway. In cylindrical batteries, sudden explosions were encountered even during the extinguishing phase of the fire.

Figure 8. Smoke development after extinguishing attempt

Figure 9. Injection of water through fusible/molten parts

Figure 10. Explosion of the prismatic cells package

Figure 11. Thermal runaway of cylindrical cells and images after explosion

Figure 12. Thermal runaway and followed by explosion of prismatic cells

Gas venting can occur at less than 100 ºC, before and without thermal runaway, multiple vents may occur, some not visible by eye. If gases are mixed with air and confined, a gas explosion can occur in case of ignition.

4. CONCLUDING REMARKS

As a result of the common studies with Çukurova University, The University of Poitiers, The National School of Mechanics and Aerotechnics (ISAE-ENSMA), The Pprime Institute academicians and Departmental Fire and Rescue Service of Vienne Region officers; the lithium ion battery fires were examined. The concept of fire was studied both theoretically and in terms of testing in the Departmental Fire and Rescue Service of Vienne Region Experimental Area in Poitiers / France.

Fire experiments and extinguishing trials have been made with electric batteries. Many attempts have been made in this regard. All extinguishing tests were done with water. For the individual cells, pure water has been seen to be the effective and convenient suppressant, due to its ability to reduce the temperature of the fire very quickly. Fire experiments have been carried out both on cell form and on multiple modules. In the experiments, batteries and battery cells were placed on a system under which a propane gas burner was placed to generate 400 kW heat power. This propane gas was given to other battery types in a fixed way and under the same conditions. As a result, in the event of a thermal runaway of the batteries characterized by an increased temperature, crackling, smoke, extinction is difficult (Li-ion), or even impossible. The protection of the environment will be a priority. Without the intervention of the fire brigade, the total combustion time of a battery can be up to 1 hour.

Lithium-ion batteries offer high energy density and many other benefits, but also risks that need to be dealt with. Design and construction can have a decisive effect on battery safety, and to assess and manage the risks it is important to maintain a holistic perspective that encompasses both the battery and the environment around and outside the battery system.

Li-ion batteries contain reactive materials and have a flammable electrolyte. The battery cell contains all three parts of the fire triangle (heat/ignition, oxygen and combustible material), even if, for example, the amount of oxygen that can be released varies between different Li-ion chemistries. If the battery cell is heated up, it is designed to release gas (to prevent a cell explosion). There are different cell formats, and they can release gases at different temperatures, e.g. pouch cells (flat prismatic cells in a pouch) can in certain cases of failure release gases from around 70 °C. If the cell temperature were to reach approx. 150–200 °C, there can be what is known as a thermal runaway. A thermal runaway is a rapid internal temperature increase that often results in one or more of the following events: heat generation, gas and smoke formation, cell breach/cell explosion, fire or gas explosion. Gas releases can typically occur at lower temperatures and without the occurrence of a thermal runaway.

Different kinds of battery explosions can occur. If the battery cell builds up high pressure (e.g. caused by a defective or poorly designed safety valve), a cell explosion can occur.

Another kind of explosion might occur if the battery gases are released and mixed with air but do not ignite immediately, but accumulate and ignite later on. This is known as a gas explosion, which can cause major damage. Battery gases contain toxic substances, e.g. the highly toxic fluoride compound hydrogen fluoride (HF).

Lithium ion batteries have a very high energy density and have wide applications. While the flammable, high energy and active material increase their dangers of fire and explosion. The fuel, oxygen and energy can exist in the battery system, which provide the necessary contributions to the combustion triangle, thus there is the possibility of fire and explosion.

The biggest advantage of cylindrical batteries in most situations is that they are very safe. If the internal pressure of a cylindrical lithium battery grows too high, most of the cells are designed to rupture - thus mitigating safety risks from situations like a fire or an explosion.

There is no guarantee of any water damage to objects. Water mist extinguishing system is not movable. The fire extinguishing properties are affected by droplet size, velocity distribution, impulse and geometric characteristics of nozzle. In recent years, the study on water mist extinguishing technology has been conducted extensively.

A cell in a cylindrical metallic case has good cycling ability, offers a long calendar life, is economical to manufacture, but is heavy and has low packaging density. The prismatic metallic case has improved packaging density but can be more expensive to manufacture, is less efficient in thermal management and may have a shorter cycle life. The prismatic pouch pack is light and cost-effective to manufacture. Exposure to high humidity and hot temperature can shorten service life.

For small consumer batteries, fire is probably the worst scenario, as a fire can also serve as an ignition source for other combustible material. To reduce the risk of battery fires, flame retardants or other substances are sometimes added, which can contain fluoride or other undesirable elements. New electrode materials have also been developed and started to come into use. This has meant that certain Li-ion cells ignite less often, but still release gases. It is possible that the gas composition when it does not burn is more toxic than when a fire has broken out, as in similar situations with other kinds of fires; the situation for Li-ion batteries has however not been investigated, as there is a lack of research in the area.

As the battery size grows, the amount of gas released can become significant. In this situation, at least in some scenarios, the gases can represent a bigger threat than a fire. As the battery gases are not incinerated, they can be mixed with air, and if the gas release has occurred in an enclosed or semi-enclosed area, the gases can accumulate. If the accumulated gas is ignited, a gas explosion can occur.

Ignition can take place through several ignition sources, both external and within the battery, e.g. an electrical contact, light arc, electrical spark or auto-ignition from a hot cell.

The use of additives can in principle both increase and decrease safety. A holistic evaluation of the use of additives is needed in order to assess overall safety, and this has not been investigated at present. In summary, the risks associated with battery gases, in terms of both toxicity and the risk of ignition/explosion, are an important element of overall safety and the risks can vary between different battery sizes, applications and environments.

5. REFERENCES

[1] J. Packer, B. Neilsen, XIV-Environment-C-Fire Fighting, Chemistry in Fire Fighting Section, NZ Fire Protection Association, 2017.

[2] Q. Wang, J. Sun, Guanquan Chu, Lithium Ion Battery Fire and Explosion, Fire Safety Science–Proceedings of the Eighth International Symposium, pp. 375-382, 2015.

[3] K. Liu, Y. Liu, D. Lin, A. Pei, Y. Cui, Materials for Lithium-ion Battery Safety, Science Advances, 4 (6), pp. 1-11, 2018.

[4] State of the Electric Vehicle Lithium-Ion Battery Market Report, http://pswordpress-production.s3.amazonaws.com/2019/06/State-of-the-Electric-Vehicle-Lithium-Ion-Battery-Market-PreScouter-2019.pdf

[5] R. Schröder, M. Aydemir, G. Seliger, Comparatively Assessing Different Shapes of Lithium-ion Battery Cells, Procedia Manufacturing Journal 8, pp. 104-111, 2017.

[6] H. Saariluoma, A. Piiroinen, A. Unt, J. Hakanen, T. Rautava, A. Salminen, Overview of Optical Digital Measuring Challenges and Technologies in Laser Welded Components in EV Battery Module Design and Manufacturing, Batteries 6, p. 47, 2020.

[7] E. Maiser, Battery Packaging - Technology Review, AIP Conference Proceedings, 2015.

[8] R. Bisschop, O. Willstrand, F. Amon, M. Rosengren, Rise Report 2019:50 Fire Safety of Lithium-ion Batteries in Road Vehicles, Rise Safety & Transport Fire Research, 2019.

[9] D. Ouyang, M. Chen, Q. Huang, J. Weng, Z. Wang, J. Wang, A Review on the Thermal Hazards of the Lithium-Ion Battery and the Corresponding Countermeasures, Applied Sciences 9 (12), p. 2483, 2019.

[10] S. Basu, S. Suresh, K. Ghatak, S. Bartolucci, T. Gupta, P. Hundekar, R. Kumar, T. Lu, D. Datta, Y. Shi, Utilizing van der Waals Slippery Interfaces to Enhance the Electrochemical Stability of Silicon Film Anodes in Lithium-ion Batteries, ACS Applied Materials & Interfaces 10, pp. 13442-13451, 2018.

[11] P. Sun, H. Niu, X. Huang, R. Bisschop, R., A Review of Battery Fires in Electric Vehicles, Fire Technology, pp. 1-50, 2020.

[12] Manufacturing Lithium-Ion Batteries, http://www.techsciresearch.com/blog/manufacturing-lithium-ion-batteries/29.html

[13] X. Cui, S.K. Kam, C. May, M. Chin, J. Chen, C. Babu, Models Based on Mechanical Stress, Initial Stress, Voltage, Current, and Applied Stress for Li-ion Batteries During Different Rates of Discharge, Energy Storage, 2 (3), pp. 1-10, 2019.

[14] M. Gentilleau, S. Delaunay, D. Pelletier, S. Cardou, A. Gransagne, J. Deparis, Fire Service Operational Handbook-Emergency Response on Vehicles, Departmental Fire and Rescue Service of Vienne Region publications. Chasseneuil Cedex City. Version 7, pp. 9-10. 2020.

REAL-TIME TRAJECTORY CONTROL OF AN INDUSTRIAL SERVO MOTOR DEVELOPING FOR INDUSTRY 4.0 APPLICATIONS

S. Oner[1], G. Bayrak[1*], H. Meral[2], N.M. Saraç[2], E. Pehlivan[2], A. Şahiner[2]

[1]Bursa Technical University, Department of Electrical and Electronics Engineering, Bursa, Turkey.
[2]Sibernetik R&D Center, Demirci Mh. Demirciyolu Cd. No: 58, Bursa, Turkey.
gokay.bayrak@btu.edu.tr

ABSTRACT

PLC modules generally control servo motors used in all areas of the industry. The increase in technological competitiveness on a global scale and the results of Industry 4.0 have led to the need to develop real-time monitoring, control, automation system, and software using LabVIEW infrastructure instead of the standard PLC-based automation system. As a result, it is aimed to increase reporting, real-time monitoring, graphing, testing, analysis, and communication capabilities.

In this study, an AC servo motor and a cylinder system connected to the servo motor's shaft were used, and the trajectory control of the servo motor was performed in real-time with LabVIEW. Then the commands to be given to the servo motor and information to be received from the servo motor were controlled by using LabVIEW with a communication protocol called Ads Server. The TwinCAT program was used for the movement of the servo system on the control screen. Position, velocity information is displayed on the interface prepared with LabVIEW on the computer from the AC servo motor, through the servo driver via the industrial PC. All operations are carried out via the developed LabVIEW interface.

Keywords: *Servo motor, trajectory control, real-time data acquisition and control*

INTRODUCTION

Special purpose machines included in servo motors used in all industries, automotive, textile, military, chemical, food, energy, etc. It is used in all systems requiring precise movement such as robotic, hydraulic, pneumatic, electro press, levers, electronic braking, automatic storage and collection, conveyor systems in many fields [1]. These systems, which have a wide range of uses, are generally controlled and monitored in PLC-SCADA systems using touch panels that communicate with PLC and PLC. The concept of Industry 4.0 is based on data sent from field sensors and terminal units of automation systems and the processing of these data. With the Industry 4.0 approach, the current working conditions, performance and results of automation systems are constantly measured. [9] With the emergence of Industry 4.0, PLC has begun to be insufficient by itself, and touch panels, whose programmability is limited and challenging in the face of developing, becoming more sensitive, and increasing product needs, have started to fail to fulfill their duties in SCADA systems [2,3].

HMI panels used in automation systems, which have only touch features, will be replaced by industrial computers where many control applications can be developed flexibly. In addition to these, it is also an important feature that the system can be monitored and controlled remotely in line with the customer's needs and thus facilitates the work of machine operators in the customer's production facilities [4,5]. By increasing the number of machines per operator, the production power increases, and this causes the costs to decrease. The ability to connect and control the system remotely in the domestic and international sales of the machines made by the servo motor in the manufacturer company, in case of malfunction or development and update requirements, reduces service costs [6].

The servo motor's trajectory control application realized in this study aims to develop a real-time control and automation software that will adapt to the developing technology with Industry 4.0 instead of classical PLC-SCADA systems. In the study, an AC servo motor, which is frequently used in the industry, was controlled by a computer-based system instead of classical SCADA systems. The monitoring process is done over the industrial PC instead of the touch panel, being the center of the PLC system used as the control unit. Thus, instead of high-cost and less capable HMI panels, a more cost-effective and competent system was used. Real-time monitoring

and control software was developed using an interface designed in the LabVIEW program on a computer, and the trajectory control of the servo motor was performed bidirectionally.

SERVO SYSTEMS AND DRIVERS

Servo motors are slightly different from the standard motor types in terms of their structure. They are mostly seen as a system. These systems generally consist of a motor and feedback element. The motor part may consist of an AC or DC motor variant, and the feedback element may consist of an encoder (encoder) or a tachometer with a speed measuring device. Servo motors are highly preferred in industrial applications due to their high torque in a smaller body, high efficiency, excellent positioning accuracy, ease of speed control, low moments of inertia, no need for external cooling, and being loaded with excessive loads [7,8]. AC servo system is requested to have an accurate response for the position reference and a quick recovery for the external disturbances or load variations.

Servo motors are the electronic power element that provides precise control of each of the parameters such as speed, position, moment, and acceleration and provides the connection between the motors' central controller. Generally, AC servo drives work by imitating the grid with pulse width modulation with a sinusoidal signal. According to the motor speed, acceleration, and position, the transistors in the sample representation in Figure 1 are transmitted with the appropriate sequence to control the motor. Servo motor speed control is directly proportional to the applied voltage frequency, as in other motors [5]. Usually, magnetic sensors, incremental or absolute encoders are used as feedback.
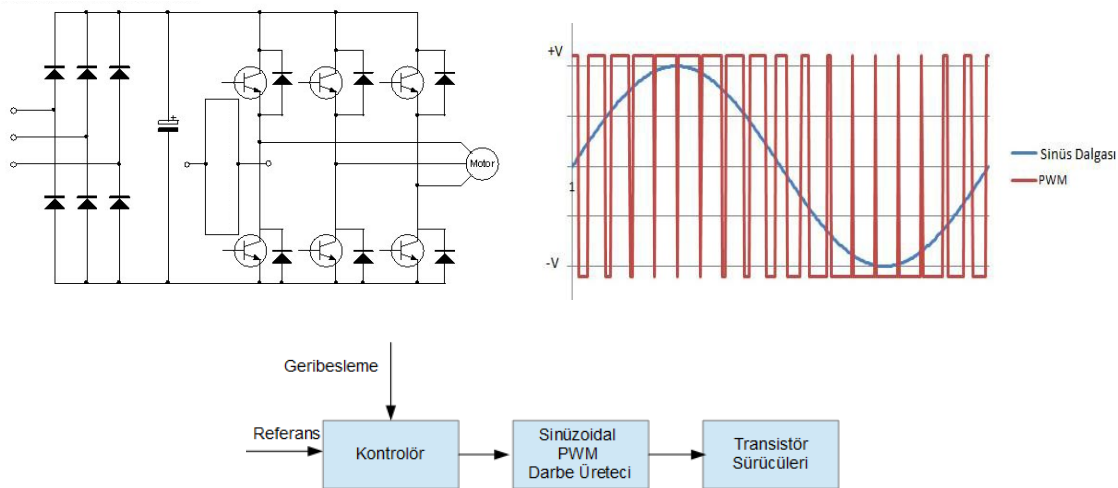
Figure 1. Operation principle of AC servo driver

Servo drives can drive more than one motor according to their models. The Beckhoff brand AX5203 coded servo drive was used in the graduation thesis application work, as shown in Figure 2. The main features of the driver are:

- Possibility of driving motor up to 2 axes.

- Three amps rated current per channel.

- Nominal supply voltage 1 phase 220 V AC or 3 phase 380 V AC.

- The maximum instantaneous current draw per channel is 10 amps.

- EtherCAT communication technology.

- Its mass is 6 kg.

- Possibility to read voltage and current values of each channel thanks to the display screen.

Figure 2. AC servo driver used in the experimental study

DEVELOPED REAL-TIME SERVO CONTROL SYSTEM

In the application work carried out, an AC servo motor, which is frequently used in the industry, was controlled by a computer-based system instead of conventional SCADA systems. The monitoring process is done over the industrial PC instead of the touch panel, being the center of the PLC system used as the control unit. Thus, instead of high-cost and less capable HMI panels, a more cost-effective and competent system was used. As seen in Figure 3, real-time monitoring and control software was developed using an interface designed in the LabVIEW program on a computer. The trajectory control of the servo motor was performed bidirectionally. [8,11]

Figure 3. General view of the system implemented, 1. Industrial PC, servo driver, and electrical panel of the system, 2. Servo motor unit, 3. A personal computer where LabVIEW interface is prepared

The block diagram of the implemented system is given in Figure 4. Here, the AC servo motor has been combined with a screw cylinder to form a compact structure. The servo motor is connected to the servo drive with a compact cable that transmits encoder information and power. The Servo driver is connected to the

industrial PC with an Ethernet cable that supports EtherCAT communication. The industrial PC was connected to the personal computer using the personal computer communication cable for which the interface was developed for programming and controlling the motor. Using the TwinCAT program, the Beckhoff PLC and servo system were communicated, and necessary parameters, adjustments, and manual tests were made on TwinCAT. After parameter adjustments, the blocks and commands required for servo motor movements are created with TwinCAT ladder programming, and variables are determined. After the program prepared in the TwinCAT program, the necessary inputs and outputs in the LabVIEW program where the main program interface and the system will be operated have been determined.
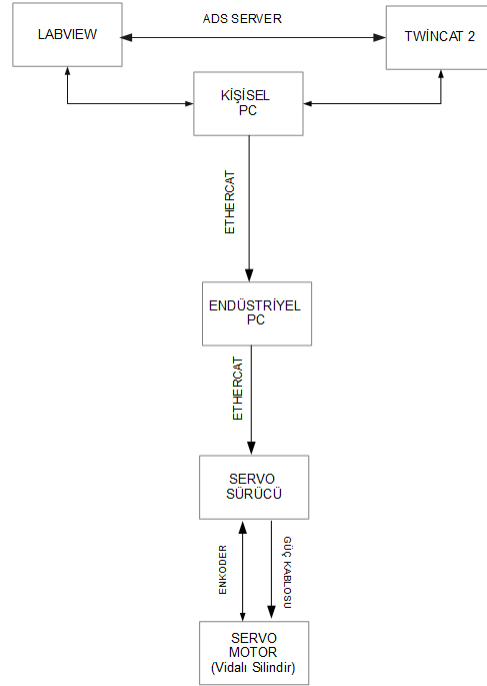
Figure 4. Block diagram of the developed program

DEVELOPED TRAJECTORY CONTROL IN LABVIEW

Variables drawn from the TwinCAT program to LabVIEW were transferred to the LabVIEW block diagram with the ADS library's help by using the port and address information. The interface part of the program in Figure 5 has been arranged, and the development of the servo motor control interface has been completed.
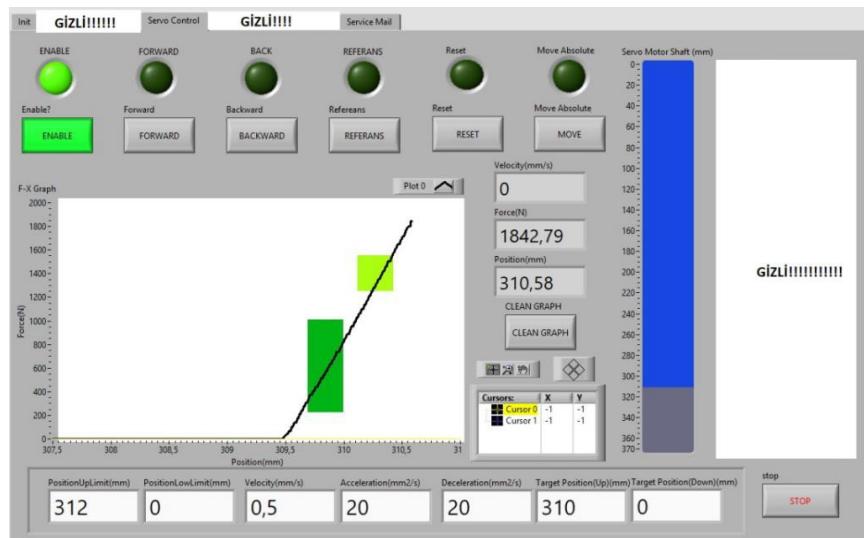

Figure 5. Designed servo motor control interface

There is one "ENABLE" button in a LabVIEW interface program to activate the servo motor. Thanks to this button, the motor can be turned on and off when desired. "FORWARD" to enable the cylinder connected to the motor to go forward, "BACKWARD" to make it go backward, "REFERENCE" button to ensure that the desired position of the cylinder shaft is selected as zero references when the servo system hits any obstacle or goes into error for any reason. There is a "RESET" button to clear the error and a "MOVE" button that will automatically switch between two points to be determined. A moving bar has been added to watch the motor shaft's motion as an animation on the LabVIEW interface. To not strain the engine in terms of safety, input controls have been added to enter the maximum and minimum points that the cylinder shaft can travel and determine the speed of the cylinder.

EXPERIMENTAL RESULTS

With the activation of the "MOVE" command in automatic mode, two different inputs will be made to ensure the movement, acceleration, deceleration accelerations, and speed input controls are included in the system. Indicators to measure the speed, position of the engine cylinder instantly with the information coming from the encoder and the value of a sample load cell connected to the end of the cylinder, as well as the force-position graph in which the change of the force of the motor after a certain point is examined in Figure 6. such as has been added to the interface. Thus, the desired movements from the motor shaft on the designed interface are achieved by using LabVIEW.
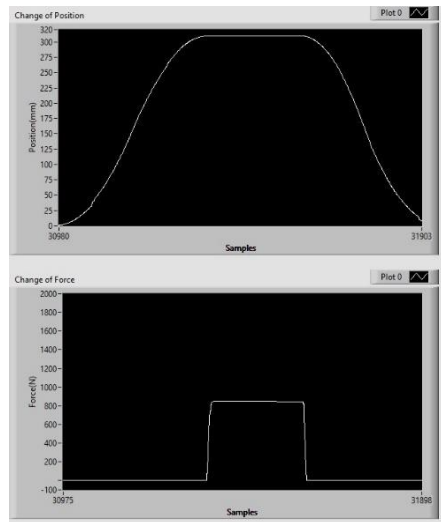
Figure 6. In practice, the position change of the cylinder shaft according to the speed and the force response of the load cell as a result of the compression of the cylinder

CONCLUSION

The industrial sector's ability to keep up with the developing technology and to develop based on Industry 4.0 is of great importance in terms of efficiency and competition. The servo motor's trajectory control application realized in this study aims to develop a real-time control and automation software that will adapt to the developing technology with Industry 4.0 instead of classical PLC-SCADA systems. In the study, an AC servo motor, which is frequently used in the industry, was controlled by a computer-based system instead of classical SCADA systems. The monitoring process is done over the industrial PC instead of the touch panel, being the center of the PLC system used as the control unit. Thus, instead of high-cost and less capable HMI panels, a more cost-effective and competent system was used. Real-time monitoring and control software was developed using the LabVIEW program's interface, and the trajectory control of the servo motor was performed bidirectionally.

REFERENCES

[1]. R. Halıcıoğlu, L.C. Dülger, A.T.Bozdana,(2015) Servo Pres Tasarımı ve Dinamik Modeli: Uygulamalı Bir Örnek, Gaziantep Üniversitesi, Gaziantep, Uluslararası Katılımlı 17. Makina Teorisi Sempozyumu, İzmir, 14-17 Haziran 2015

[2]. Közkurt, Cemil & Fenercioğlu, Ahmet & Akar, Mehmet. (2012). Otomatik Depolama Sistemlerindeki Robotlar için Servo Motor Seçimi (In Turkish). Gaziosmanpaşa Bilimsel Araştırma Dergisi. 1. 97-105.

[3]. Yıldırım, F. & Babaoğlan, H. & Tosun, L.(2016). Endüstride Kullanılan Kereste Kesme Mekanizmasının Otomatik Kontrolü ve Prototipinin Oluşturulması(Lisans Tezi). Karabük Üniversitesi, Mühendislik Fakültesi, Karabük.

[4]. Lei, S. Y. (2013). Servo-Control System Design of Automatic Production Line Based on PLC and HMI. Applied Mechanics and Materials, 457–458, 1381–1385.

[5].Yılmaz, F. H.(2008) AC ve DC Servo Sistem Eğitim Setinin Geliştirilmesi(Yüksek Lisans Tezi).Selçuk Üniversitesi, Elektrik-Elektronik Mühendisliği Anabilim Dalı, Konya.

[6]. Chanchal Dey, Sunit Sen, Industrial Automation Technologies, University of Calcutta, India

[7]. Gerçek zamanlı Ethernet:Terminale kadar ultra yüksek hız. 2013, https://www.beckhoff.com.tw/tr/default.htm?ethercat/default.htm

[8]. Hu Xing , Huan Jia , Liu Yanqianga,(2011) Motion Control System using SERCOS over EtherCAT School of Mechanical Engineering & Automation Beihang University, Beijing, China

[9]. Ö.Aydoğdu, A.Çatkafa, SECA Mühendislik Otomasyon Ltd. Şti (2019) Bir Hidrolik Derin Çekme Pres Makinesinin PLC Tabanlı Bulanık Mantık Kontrolü Ve Endüstri 4.0 Uygulaması, Konya Teknik Üniversitesi, Mühendislik ve Doğa Bilimleri Fakültesi, Elektrik – Elektronik Mühendisliği Bölümü, Konya, TÜRKİYE, ISSN: 2667-8055

[10].Hakan Terzioğlu, Gökhan Yalçın , Mustafa Kısa,(2019) Servo Motorun SCADA ile Kontrolü, Department of Electrical and Energy, Konya Technical University, Konya,Turkey, European Journal of Science and Technology Special Issue, pp. 428-435, October 2019

TRAJECTORY TRACKING WITH PID AND SLIDING MODE CONTROL FOR DIFFERENTIAL DRIVE MOBILE ROBOTS

S.Yigit[1*], A.Sezgin[1]

[1] *Istanbul University – Cerrahpasa, Mechanical Engineering Department, Istanbul, Turkey.*
* sinanyigit07@gmail.com

ABSTRACT

Differential drive mobile robot (DDMR) is the most commonly used autonomous land vehicle type for small scale trajectory planning and tracking applications. In this study, two driven wheeled and one castor wheel included DDMR model is used for kinematic and dynamic modelling. In trajectory tracking stage, kinematic based backstepping control (KBBC) is operated in order to reduce robot pose (position and orientation) error via kinematic model of the system. Sliding mode control (SMC) and proportional–integral–derivative controller (PID control) are separately implemented to the dynamic model for controlling dc motors of wheels which is requisite for tracking of given reference trajectory. Mathematical modeling of the DDMR and control strategies are simulated in software and results demonstrate that both SMC and PID control strategies with KBBC provide robust, smooth and accurate trajectory tracking performance. Because of the better SMC error performance in this study, it is foreseen that SMC can be better choice for more complex trajectory and environment conditions.

Keywords: *Trajectory Tracking, Differential Drive Mobile Robot, PID Control, Sliding Mode Control, Backstepping Control*

INTRODUCTION

Mobile robots are widespread preferred in academic studies and various industrial solutions for trajectory planning and tracking applications [1], [2], [3]. Differential drive mobile robots are more preferable among the other types of mobile robots because of the design simplicity, low energy usage and low-cost properties. In this paper, robot chassis design includes two coaxial independent wheels are mounted at the backside of the robot chassis, one free rotatable castor wheel in the front side and also two dc motors for each wheel drive. Besides, benefits of DDMR, motion control of DDMR is still needs to be in progress because of the nonholonomic system properties. The nonlinearity of DDMR is due to the nonholonomic constraints, makes it difficult to control smoothly, time invariantly and robustly which can be understood from Brockett's necessary condition. In order to eliminate these difficulties a couple of assumptions can be obtained such as, no-slip condition for wheels and certain control ability of motor speed and robot position [4] [5].

Although, there are various conventional control methods were applied to the motion control of DDMR in literature, alternative control methods can provide more robust, certain, fast and better transient performance which makes reasonable to study about trajectory tracking of DDMR. In trajectory tracking stage, kinematic based backstepping control (KBBC)is operated in order to reduce robot pose (position and orientation) error via kinematic model of the system. SMC and PID control are separately implemented to the dynamic model for controlling dc motors of wheels which is requisite for tracking of given reference trajectory. Mathematical modeling of the DDMR and control strategies are simulated in software and results demonstrate that SMC and PID control with KBBC gives robust, smooth and accurate tracking performance. In addition to this, critical points of the trajectory SMC have slightly better approach to the reference pose variables. [5][6]

DIFFERENTIAL DRIVE MOBILE ROBOTSYSTEM OVERVIEW

Differential drive mobile robots can be designed with two independently driven wheels and one castor wheel as Figure1. These back wheels are motioned through direct current (DC) motors which are controlled via mathematical models in software. In order to get mathematical model of DDMR motion, necessary coordinate systems need to be stated as Figure 1. Robot coordinate system $\{X_R, Y_R\}$ is fixed robot chassis and

inertial coordinate system $\{X_I, Y_I\}$ is defined as fixed universal coordinates will be used for calculations following sections.

Kinematic Model

The position and orientation of the DDMR in the initial and robot coordinate systems can be obtained in vector form in Equation 1.

$$q = \begin{bmatrix} x \\ y \\ \theta \end{bmatrix}, \; q_i = \begin{bmatrix} x^i \\ y^i \\ \theta^i \end{bmatrix}, \; q_r = \begin{bmatrix} x^r \\ y^r \\ \theta^r \end{bmatrix} \tag{1}$$

Orthogonal rotation matrix $R(\theta)$ represents the mathematical transformation between initial coordinate system and robot coordinate system in Equation 2

$$R(\theta) = \begin{bmatrix} \cos\theta & -\sin\theta & 0 \\ \sin\theta & \cos\theta & 0 \\ 0 & 0 & 1 \end{bmatrix} \tag{2}$$

In order to simulate motion of the DDMR, two main assumptions must be accepted;
No slip motion along the Y_R axis.
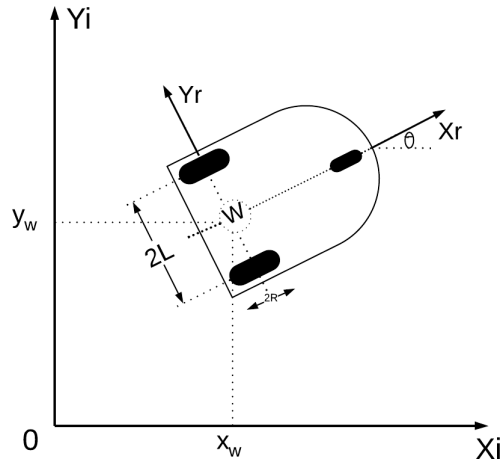
Figure 1. Robot Coordinate System

$$\dot{y}_w^r = 0 \tag{1}$$

And pure rolling constrains represent any slipping along the X_R axis, which means that wheels has one contact point with surface while trajectory tracking application. Pure rolling velocities;

$$V_p r = R\omega_r, \qquad V_p l = R\omega_l \tag{2}$$

The velocity mathematical representation of the velocities as shown in Equations 5 and Equation 6, V is the linear velocity and W is the angular velocity of DDMR. [7]

$$V = \frac{v_r + v_l}{2} = R\left(\frac{\omega_r + \omega_l}{2}\right) \tag{5}$$

$$W = \frac{v_r - v_l}{2L} = R\left(\frac{\omega_r - \omega_l}{2L}\right) \tag{6}$$

Robot pose expression is shown in equations 7,8 with respect to reference point W;

42

$$\dot{q}^r = \begin{bmatrix} \dot{x}_\omega^r \\ \dot{y}_\omega^r \\ \dot{\theta}^r \end{bmatrix} = \begin{bmatrix} R/2 & R/2 \\ 0 & 0 \\ R/2 & R/2 \end{bmatrix} \begin{bmatrix} \omega_r \\ \omega_l \end{bmatrix} \tag{1}$$

$$\dot{q}^i = \begin{bmatrix} \dot{x}_\omega^i \\ \dot{y}_\omega^i \\ \dot{\theta}^i \end{bmatrix} = \begin{bmatrix} \dfrac{R}{2}\cos\theta & \dfrac{R}{2}\cos\theta \\ \dfrac{R}{2}\sin\theta & \dfrac{R}{2}\sin\theta \\ R/2L & R/2L \end{bmatrix} \begin{bmatrix} \omega_r \\ \omega_l \end{bmatrix} \tag{2}$$

$$\begin{bmatrix} \dot{x}_a^i \\ \dot{y}_a^i \\ \dot{\theta}^i \\ \omega_r \\ \omega_l \end{bmatrix} = \begin{bmatrix} \dfrac{R}{2}\cos\theta & \dfrac{R}{2}\cos\theta \\ \dfrac{R}{2}\sin\theta & \dfrac{R}{2}\sin\theta \\ R/2L & -R/2L \\ 1 & 0 \\ 0 & 1 \end{bmatrix} \begin{bmatrix} \omega_r \\ \omega_l \end{bmatrix} \tag{3}$$

Dynamic Model

The difference between kinematic based trajectory tracking and real tracking can be optimized by designing dynamic model of DDMR.

DDMR as a nonholonomic system with n generalized coordinates $(q_1, q_2 \dots q_n)$ and dependent to m constraints can be described by Equation 10; [8];

$$M(q)\ddot{q} + V(q,\dot{q})\dot{q} + F(\dot{q}) + G(q) + \tau_a = B(q)\tau - A^T(q)\lambda \quad (10)$$

The kinetic energy (T) and potential energy (U) of the system are formulated to obtain dynamic model based on Lagrange Method.

$$L = T - U \tag{11}$$

The Lagrange equation can be expressed as below;

$$\frac{d}{dt}\left(\frac{\partial L}{\partial \dot{q}_i}\right) + \left(\frac{\partial L}{\partial q_i}\right) = F - A^T(q)\lambda$$

The potential energy of DDMR is accepted as zero because DDMR moves just in $X_i Y_i$ plane. The kinetic energy of robot body, kinetic energy of wheels and actuators generate total kinetic energy of DDMR.

$$m = m_c + 2m_\omega, \qquad I = I_c + m_c d^2 + 2m_\omega L^2 + 2I_m \tag{4}$$

$$T = \frac{1}{m}\left(\dot{x}_a^2 + \dot{y}_a^2\right) - m_c d\dot{\theta}\left(\dot{y}_a \cos\theta - \dot{x}_a \sin\theta\right) + \frac{1}{2}I_\omega\left(\dot{\omega}_r^2 + \dot{\omega}_l^2\right) + \frac{1}{2}I\dot{\theta}^2 \tag{5}$$

The equation of motion can be defined by using Equation 12 and Lagrange Function $(L = T)$ as follow;

$$m\ddot{x}_a - md\ddot{\theta}\sin\theta - md\dot{\theta}^2\cos\theta = A_1 \tag{6}$$

$$m\ddot{y}_a - md\ddot{\theta}\cos\theta - md\dot{\theta}^2\sin\theta = A_2 \tag{7}$$

$$I\ddot{\theta} - md\ddot{x}_a\sin\theta + md\ddot{y}_a\cos\theta = A_3 \tag{8}$$

$$I_\omega \ddot{\theta}_r = \tau_r + A_4 \tag{9}$$

$$I_\omega \ddot{\theta}_l = \tau_l + A_5 \tag{10}$$

$$A^T(q) = \begin{bmatrix} A_1 \\ A_2 \\ A_3 \\ A_4 \\ A_5 \end{bmatrix} \tag{20}$$

The equations of motion (15-19) are obtained in general form shown in equation 9 as;

$$M(q)\ddot{q} + V(q,\dot{q})\dot{q} = B(q)\tau - A^T(q)\lambda \tag{11}$$

$$S(q) = \frac{1}{2}\begin{bmatrix} R\cos\theta & R\cos\theta \\ R\sin\theta & R\sin\theta \\ R/L & -R/L \\ 2 & 0 \\ 0 & 2 \end{bmatrix}, \eta = \begin{bmatrix} \omega_r \\ \omega_l \end{bmatrix} \tag{12}$$

$$\dot{q} = S(q)\eta, \quad \ddot{q} = \dot{S}(q)\eta + S(q)\dot{\eta} \tag{13}$$

Substituting $\dot{q}$ and $\ddot{q}$ in general form;

$$M(q)\left[\dot{S}(q)\eta + S(q)\dot{\eta}\right] + V(q,\dot{q})\left[S(q)\eta\right] = B(q)\tau - A^T(q)\lambda \tag{14}$$

Thus, dynamic equations of the system can be written in alternative way as;

$$M'(q)\dot{\eta} + V'(q)\eta = B'(q)\tau \tag{15}$$

Kinematic Based Backstepping Control

The first derivative of the pose error is written in Equation 28; [9]

$$\dot{e}_p = \begin{bmatrix} \dot{e}_x \\ \dot{e}_y \\ \dot{e}_\theta \end{bmatrix} = \begin{bmatrix} \omega_d e_y - v_d + v_r \cos e_\theta \\ -\omega_d e_x + v_r \sin e_\theta \\ \omega_r - \omega_d \end{bmatrix} \tag{16}$$

In this step, Lyapunov stability approach is used for analysis of the controller, [5] [10]

$$L_1 = \frac{\left(e_x^2 + e_y^2\right)}{2} + \frac{1 - \cos e_\theta}{k_2} \tag{17}$$

In this equation, $k_2 > 0$ and $L_1 \geq 0$.

$$\dot{L}_1 = -e_x\left(v_d - v_r \cos e_\theta\right) - \sin e_\theta\left(\frac{\omega_d - \omega_r}{k_2} - v_r e_y\right) \tag{18}$$

$$\dot{L}_1 < 0 \tag{19}$$

Where, the KBBC law can be determined as;

$$v_d = \begin{bmatrix} k_1 e_x + v_r \cos e_\theta \\ \omega_r + k_2 v_r e_y + k_3 v_r \sin e_\theta \end{bmatrix} \tag{20}$$

Sliding Mode Control

The sliding mode control works based on the defined sliding surface and convergence from initial condition to reference condition with a smooth movement. Mathematical expression of the DDMR system can be obtained as 33 in order to decide sliding surface.

$$\dot{\underline{x}} = \underline{f}(x) + [B]\underline{u} \tag{21}$$

Linear velocity, angular velocity and also reference velocities are obtained as controlled parameters while defining $f(x)$.

If we organize equation 25 considering Equations 5 and 6, following equations can be shown as,[11];

$$\left(m + \frac{2I_\omega}{R^2}\right)\dot{V} - m_c dW^2 = \frac{1}{R}(\tau_r + \tau_l) \tag{22}$$

$$\left(I + \frac{2L^2}{R^2}I_\omega\right)\dot{W} - m_c dWV = \frac{1}{R}(\tau_r - \tau_l) \tag{23}$$

The control inputs of the system can be selected as Equation 36,

$$\underline{u} = \begin{bmatrix} u_1 \\ u_2 \end{bmatrix} = \begin{bmatrix} \tau_r + \tau_l \\ \tau_r - \tau_l \end{bmatrix} \tag{24}$$

The sliding surface (σ) is obtained as below;

$$\sigma = G\Delta X \tag{25}$$

$$G = \begin{bmatrix} \alpha_1 & 0 & 1 & 0 \\ 0 & \alpha_2 & 0 & 1 \end{bmatrix} \tag{26}$$

Γ is a positive definite diagonal matrix which is identified properly to get acceptable control results. Total SMC control input with equivalent control torque u_{eq} is defined as below; [12]

$$u = u_{eq} + (GB)^{-1}\Gamma\sigma \tag{27}$$

In order to eliminate the difference between calculated and actual equivalent control torque, a low pass filter is applied the control input.

$$\tau\dot{\hat{u}}_{eq} + \hat{u}_{eq} = u \tag{28}$$

Thus, final version of the SMC control input is shown in Equation 41;

$$u(t) = \hat{u}_{eq}(t) + (GB)^{-1}\Gamma\sigma \tag{29}$$

SIMULATION

Differential drive mobile robot body parameters and estimated driving components are modeled mathematically and simulated on Matlab Simulink environment. Reference path is defined mathematically on Matlab and trajectory tracking simulated for KBBC+SMC and KBBC+PID. In order to observe PID control and SMC performance, KBBC design and parameters defined in the same way.

DDMR model parameters are estimated as in the Table 1 and PID control parameters $\left(K_p, K_i \text{ and } K_d\right)$, SMC parameters $\left(\alpha_{1,2}, \Gamma_{1,2}\right)$ and also KBBC parameters are defined as $\left(k_1, k_2 \text{ and } k_3\right)$ are shown in Table 2. Reference path and velocities are defined for both SMC and PID control as;

$x = t, y = \sin t, \theta = a\tan(/yx)$
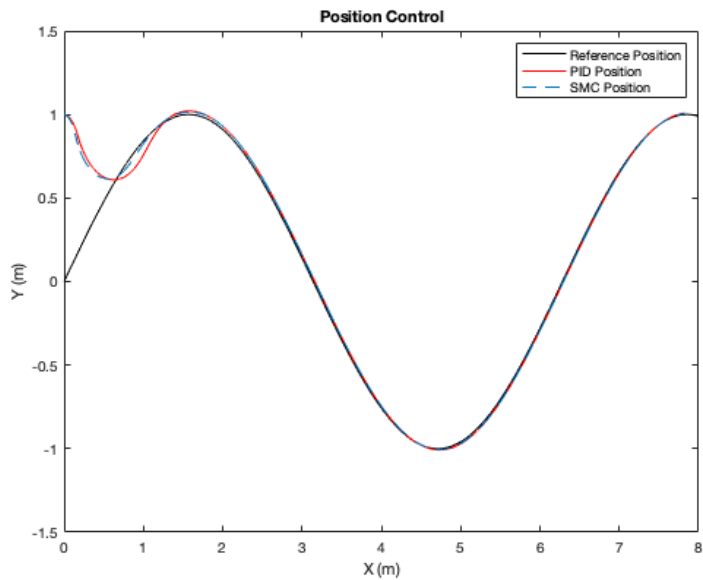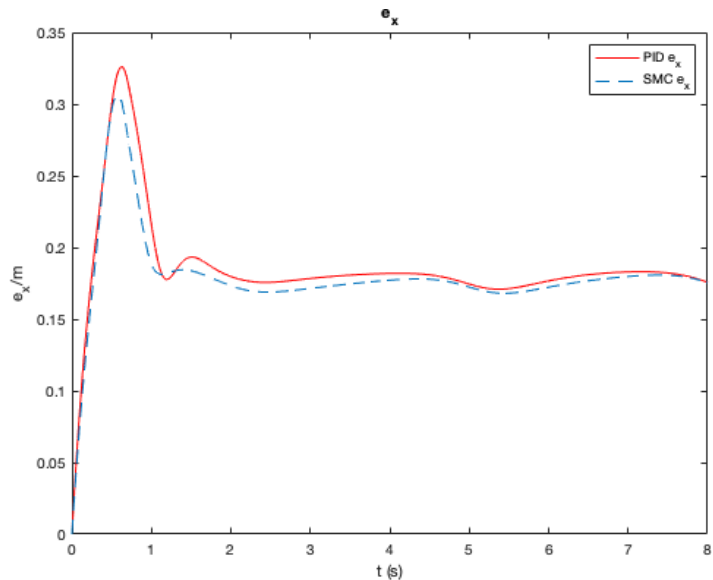$V_r = 0.15m/s, W_r = 0.1rad/s$

Figure 2. DDMR Trajectory Tracking
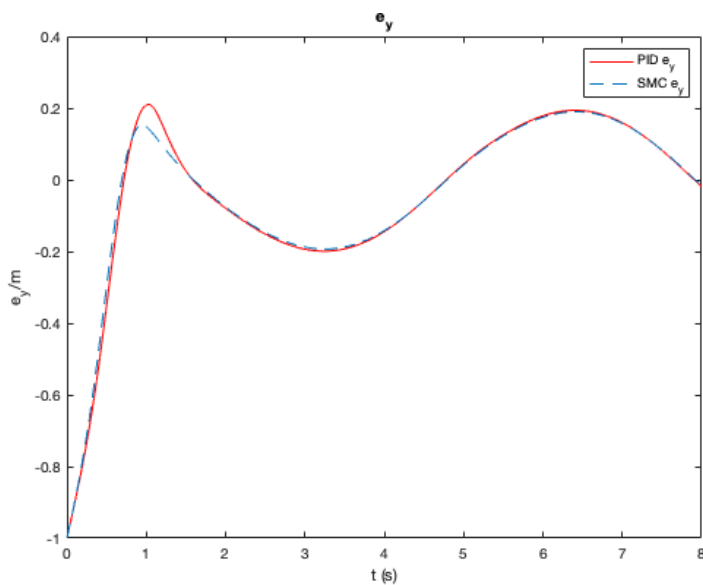

Figure 3. X Coordinate Error

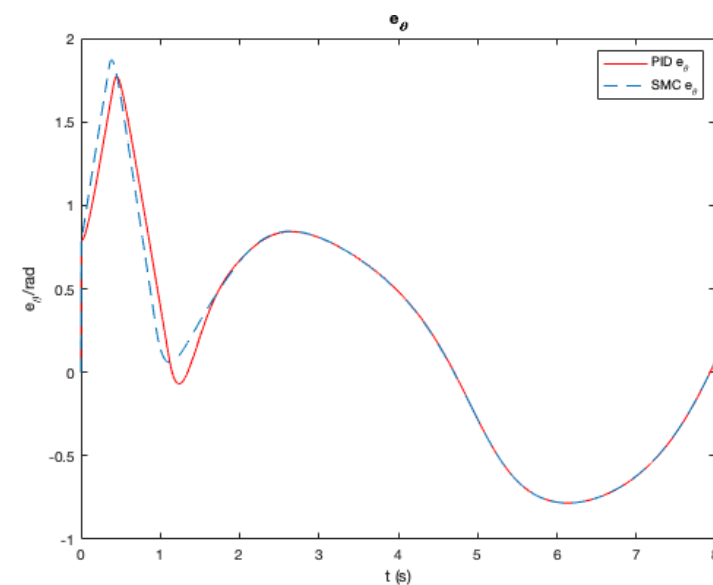**Figure 4.** Y Coordinate Error
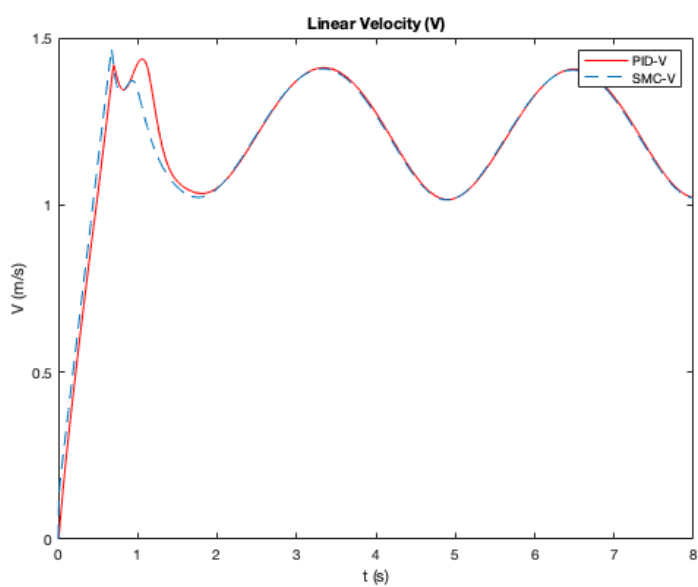

Figure 5. Heading Angle Error
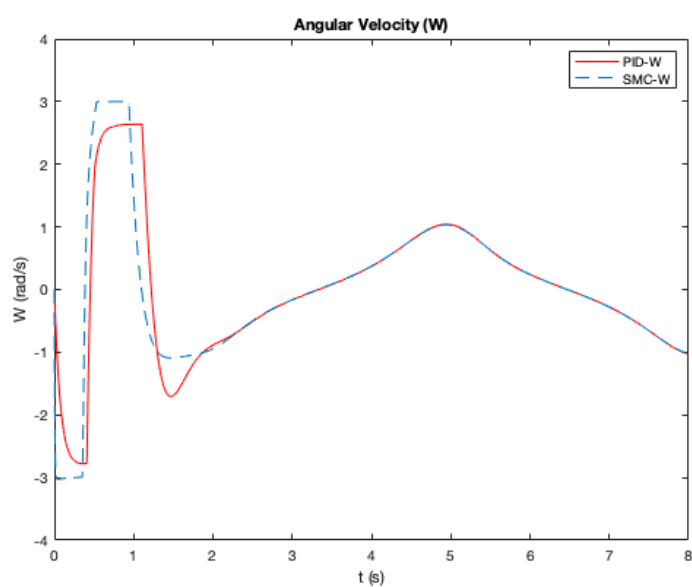

Figure 6. Linear Velocity

Figure 7. Angular Velocity

RESULT AND DISCUSSION

Simulation results shows that both SMC and PID control strategies perform successfully with KBBC strategy on predefined fully collision free environment. Besides, SMC path tracking performance slightly better than PID control in terms of quick response time at the beginning of the simulation and critical return points of the trajectory as shown in Figure 2. And Figure 3, 4, 5 shows that error performances are very similar for both SMC and PID control on this simulation conditions but also SMC is one little step ahead than PID control. Because of the known more robust control performance of SMC design which should be preferred instead of PID control strategy in complicated circumstances.

As a further study, it can be planned that both control strategies are going to be developed mathematically with additional control units to make controllers more adaptive and efficient based on the dynamic trajectory conditions. In addition to this both controllers would be tested with experimental setup for getting more realistic performance comparison between controllers.

NOMENCLATURE

m.	Mass
2L	Semi Track Width
I	Moment of Inertia
V	Linear Velocity
W	Angular Velocity
q	Robot Pose
X,Y	Coordinate Values of Robot Position
u	Control Input
τ	DC motor Torque

APPENDIX

Table 1. Model Parameters

Term	Value	Unit
m_{cc}	26	kg
m_{ww}	0,5	kg
I_{cc}	0,5	$k. mm^2$
I_{ww}	0,0020	$k. mm^2$
I_{mm}	0,0011	$k. mm^2$
R	0,10	m
L	0,170	m
d	0.05	m

Table 2. Controller Parameters

Term	Value
K_{pp}	10
K_{ii}	0,5
K_{dd}	0,5
α_{12}	100
Γ_{12}	75
k_1	95
k_2	45
k_3	0,2

REFERENCES

[1] M. S. A. Mahmud, M. S. Z. Abidin, Z. Mohamed, M. K. I. Abd Rahman, and M. Iida, "Multi-objective path planner for an agricultural mobile robot in a virtual greenhouse environment", Computers and Electronics in Agriculture, vol. 157, pp. 488–499, 2019.

[2] H. Li and A. V. Savkin, "An algorithm for safe navigation of mobile robots by a sensor network in dynamic cluttered industrial environments", Robotics and Computer-Integrated Manufacturing, vol. 54, pp.65–82, 2018.

[3] Q.-V. Dang, I. Nielsen, S. Bøgh, and G. Bocewicz, "Modelling and scheduling autonomous mobile robot for a real-world industrial application", IFAC Proceedings Volumes, vol. 46, no. 9, pp. 2098–2103, 2013.

[4] X. Wu, P. Jin, T. Zou, Z. Qi, H. Xiao, and P. Lou, "Backstepping trajectory tracking based on fuzzy sliding mode control for differential mobile robots", Journal of Intelligent & Robotic Systems, vol. 96, no. 1,pp. 109–121, 2019.

[5] Y. Kanayama, Y. Kimura, F. Miyazaki, and T. Noguchi, "A stable tracking control method for an autonomous mobile robot", in Proceedings. IEEE International Conference on Robotics and Automation. IEEE, 1990, pp. 384–389.

[6] F. Demirbas, and M. Kalyoncu, "Differential drive mobile robot trajectory tracking with using pid and kinematic based backstepping controller", Selçuk Üniversitesi Mühendislik, Bilim ve Teknoloji Dergisi, vol. 5, no. 1, pp. 1–15, 2017.

[7] T. Hellström, "Kinematics equations for differential drive and articulated steering.", Department of Computing Science, Ume University, 2011.

[8] L. Armesto, V. Girbés, A. Sala, M. Zima, and V. Šmídl, "Duality-based nonlinear quadratic control: Application to mobile robot trajectory-following", IEEE Transactions on Control Systems Technology, vol. 23,no. 4, pp. 1494–1504, 2015.

[9] N. Wada, S. Tagami, and M. Saeki, "Path-following control of a mobile robot in the presence of actuator constraints", Advanced Robotics, vol. 21, no. 5-6, pp. 645–659, 2007.

[10] R. Ahmad Abu Hatab, "Dynamic modelling of differential-drive mobile robots using lagrange and newton-euler methodologies: A unified framework", Advances in robotics & automation, 02 (02), 2013.

[11] O. Mohareri, "Mobile robot trajectory tracking using neural networks", Ph.D. dissertation, 2009.

[12] Y. Z. Arslan, A. Sezgin, and N. Yagiz, "Improving the ride comfort of vehicle passenger using fuzzy sliding mode controller", Journal of vibration and control, vol. 21, no. 9, pp. 1667–1679, 2015.

COMPARISON OF PERFORMANCE DATA OF ELECTRIC VEHICLE AND INTERNAL COMBUSTION ENGINE-POWERED VEHICLE

Y. KARAGÖZ[1*], Ö. BALCI[2], Ş. PUSAT[2]

[1] *Istanbul Medeniyet University, Mechanical Engineering Department, Istanbul, Turkey.*
[2] *Yildiz Technical University, Mechanical Engineering Department, Istanbul, Turkey.*

*yasin.karagoz@medeniyet.edu.tr

ABSTRACT

The theoretical model verification of the experimental results of a single cylinder engine has carried out in the performed study. Then one dimensional model and multicylinder engine model have set up. Afterward, vehicle model which developed with the help of Matlab-Simulink for the selected sample vehicle and fuel consumption data for conventional internal combustion engine-powered vehicle has determined. Then, energy consumption data occurred from electric vehicles have determined. Invertor, electric engine, battery yields have taken into consideration for the electric vehicle. Also conventional vehicle for the EUDC cycle and electric vehicle data have compared with the consideration the emission values which spread from power plants.

Keywords: *Electric vehicle, vehicle model, emission, fuel consumption, driving cycle.*

INTRODUCTION

Today, there is a take over from conventional engines to electric vehicles. But emission values based on electric vehicles are change according to countries and power plants. Various studies have been conducted with the fuel consumption model in the literature.

Zhang et al. [1] carried out a study that they have developed a model that can instantly predict fuel consumption for the hybrid electric vehicle. The operating mode has selected by predicting the fuel consumption in different hybrid operating scenarios, depending on the operating conditions of the internal combustion engine, electric motor and battery, with the help of the model that they developed. Then developed model has verified different travel cycles and tested under traffic flow conditions and it has concluded that around 30% fuel saving has achieved.

Zhao et al. [2] carried out a study that data have gathered from the vehicle with the help of OBD on-board diagnostic and smart phone. Thus, fuel consuming data have collected depend on driving characteristics. Thus, fuel consuming data have predicted with the help of back propagation (BP) neural network, support vector regression (SVR), and random forests methods. They have concluded according to results that accuracy were under 10% for the each three models.

Leung and Williams [3] carried out a study that fuel consumption and emission values have obtained of a lot of vehicles' chassis dynamometer of the spark engine vehicle in Australia. Then they have concluded that developed model could accurately estimate the fuel consumption and emission values on the chosen route in Sydney.

Yao et al. [4] carried out a study that they have emphasized that prediction of fuel consumption and emission values with the help of developed system is an very important factor. They have provided the prediction of fuel consumption and emission values with the developed model depending on the driving parameters. They have concluded that they developed model that could give results with sufficient accuracy for intelligent transportation systems from the results they obtained.

Bifulco et al. [1] carried out a study that they have developed real-time microscopic fuel consumption model. Then, the developed model have adapted to Advance Driving Assistance System. They have concluded that they developed model could defenselessly estimate the fuel consumption values depend on obtained results.

Firstly, multi cylinder engine has set up with the help of single cylinder SI engine model that confirmed with experimental data in the performed study. Then, engine maps have created with the help of multi cylinder engine model that developed with one dimensional model. Then, vehicle model has developed with the help of Matlab-Simulink. Right after, EUDC cycle emission values and fuel consumption data have procured with the help of developed vehicle model. After that, electric vehicle model has developed. Consumed energy amount for the EUDC cycle has found with the developed electric vehicle model. Then, emission that spread from electric vehicles have found with the consideration of emission values that spread from power plants, they have comprised with the emissions from conventional internal combustion vehicle model.

SI Engine Model

Firstly, a single cylinder, normally aspirated, gasoline engine has loaded with the help of dynamometer and the tests have applied. Theoretical model has validated with experimental results that obtained from SI engine. Then, data have obtained for four cylinder engine with the using of developed theoretical model data. Specific fuel consumption and emission data have obtained according to the power and engine speed values.

1.16 L, normally aspirated, gas injected, natural gas powered test engine has used during experiments. Test engine specifications are given in Table-1.

Table – 1 Test Engine Specifications

Engine brand	Honda
Number of cylinder	1
Cylinder volume (cc)	270
Bore (mm)	77
Stroke (mm)	58
Max power (kW)	6.3 kW @ 3600 rpm
Cooling system	Air
Aspiration system	Naturally aspiration

Engine Model

Engine model has created with the help of AVL Boost one dimensional analyze program in the performed study. Engine model schematic view is given in Figure-1.
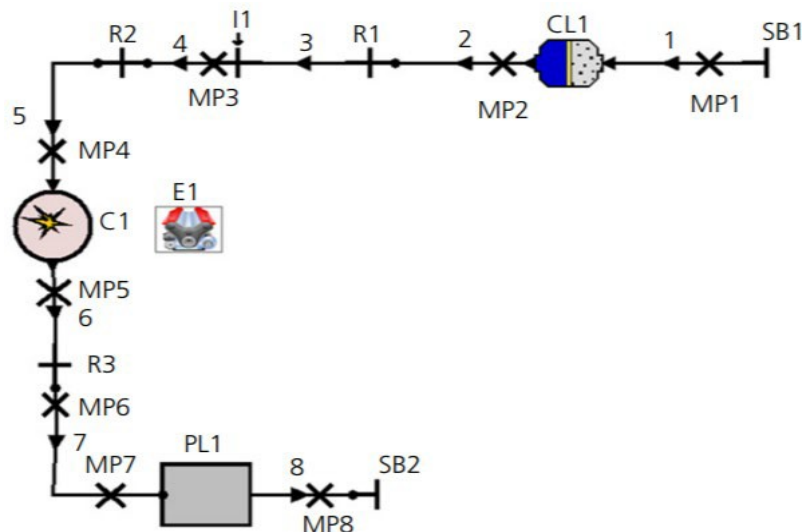

Figure-1 Schematic view of engine model

Vehicle Model

Fuel consumption values under different cycle and load (engine power) and emission values (CO, HC and NO_x) with engine model have obtained. Then, as seen in Figure-2, vehicle model has developed with the help of Matlab-Simulink. Fuel consumption and emission data have found for the conventional internal combustion engine for the EUDC driving cycle in the developed vehicle model.
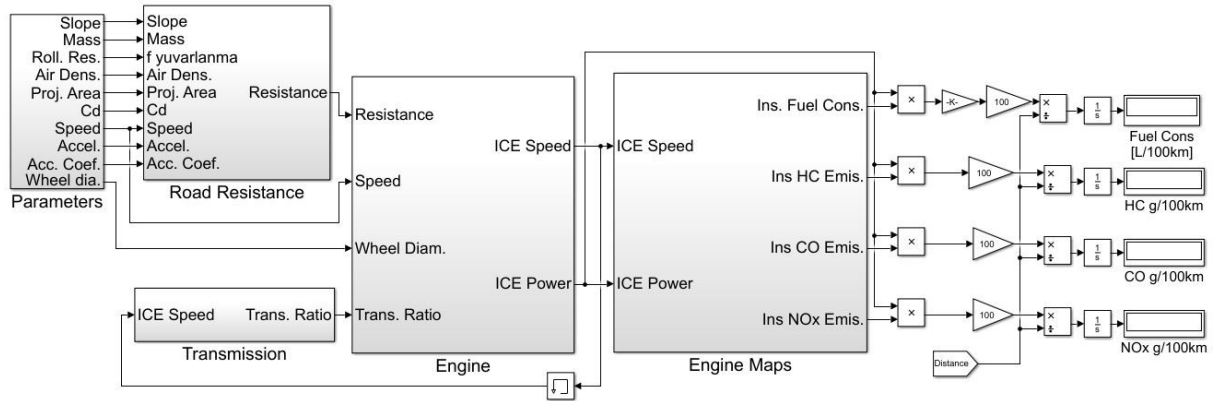
Figure-2 Developed vehicle model developed with the help of Matlab-Simulink

Electric Vehicle Model

As seen in Figure-3, electric vehicle model has set up with the help of Matlab-Simulink. 30 kW nominal rated power engine has modelled with the help of 10 kWh batteries and inverter in the developed model. 3 dimensional yield coefficients of electric engine, battery and invertor have entered. Thus, energy consumption in EUDC cycle could be found.
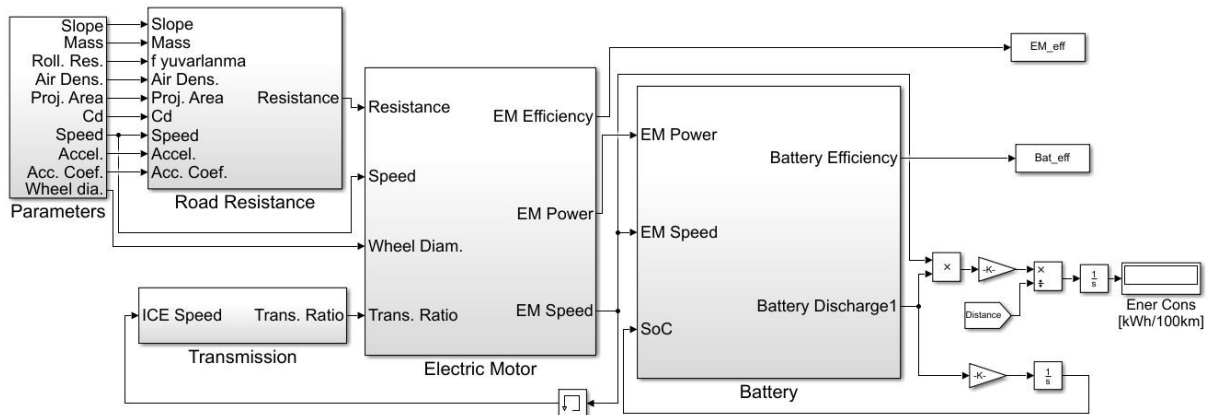
Figure-3 Electric vehicle model developed with the help of Matlab-Simulink

Theoretical Study

In despite of electric engine yield, battery yield and invertor yield have entered with the 3 dimensional maps in the electric vehicles, network loses have entered constant coefficient. Emission data have obtained take advantage of electric power plants emissions in the literature. After then, emission and fuel consumption data between electric vehicles and conventional engine vehicles have compared for EUDC driving cycle.

Results and Discussions

Firstly, 3 dimensional engine maps have created with the help of one dimensional engine model in the performed study. Then, fuel consumption data in EUDC cycle has found with the help of developed vehicle in Matlab-Simulink. In the final phase, electric vehicle model has created with the help of 3 dimensional electric engine yield, invertor yield and battery yield maps. Fuel consumption and emissions (CO, HC and NO_x) of electric vehicle and

conventional internal combustion engine vehicle have compared with the consideration of high tension line in plants and battery charge loses and average emission values.

In this study, annual electricity production data was utilized to get unit emissions from electricity generation for 2010 [6]. Annual electricity production is about 211 TWh in 2010. Total emissions generated from power plants are utilized to calculate unit emissions [7]. Unit emissions calculated for electricity generation system are presented in Table -2.

Table – 2 Unit emissions for electricity generation system in 2010.

Emission	g/kWh
NOx	1.50
CO	0.55
NMVOC	0.05
SOx	1.96
N2O	0.006
CH4	0.02
CO2	505.8

Energy Consumption

Fuel consumption data of electric vehicle and internal combustion engine vehicle in the NEDC driving cycle has compared in terms of energy consumption. Electric vehicle energy consumption value, gasoline powered vehicle energy consumption value has been calculated with consideration of lower heating value. In this way, energy consumption data of electric vehicle and conventional gasoline powered vehicle has found. Then, as seen in Figure-4, the comparison of electric vehicle and internal combustion engine vehicle has been applied. Values that have obtained in EUDC cycle has iterated to 100 km. Also high tension line losses and battery charge values have added into energy consumption results in electric vehicle. Energy consumption value with electric vehicle usage value decreased from 45.45 kWh/100 km to 21.80 kWh/100 km according to obtained results.

Figure-4 Comparison of energy consumption data

CO Emissions

CO emission release in EUDC driving cycle has calculated for the conventional internal combustion engine vehicle with the help of developed engine model and vehicle model. Energy consumption has found with the help of developed vehicle model for the electric vehicle again. Then, CO emissions have obtained from released emissions from plants with the consideration of high tension line losses. Then, as seen in Figure-5, electric vehicle and conventional engine vehicle data have compared. CO emission releasing value decreased from 1849.0 g/100 km to 11.9 g/100 km with the using electric vehicle according to obtained results.
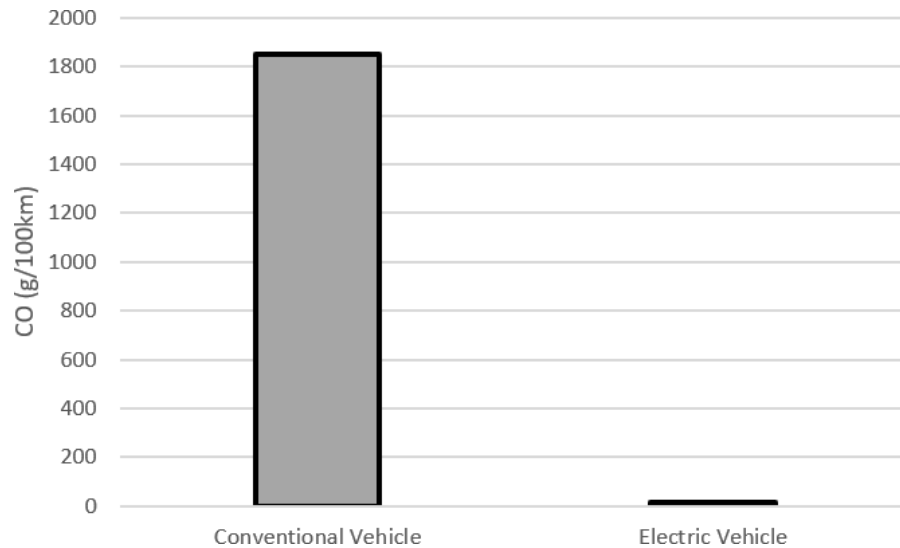
Figure-5 Comparison of CO emission data for conventional internal combustion engine vehicle and electric vehicle

HC Emissions

HC emission value for conventional internal combustion engine vehicle has calculated with the help of one dimensional AVL Boost engine model and Matlab-Simulink vehicle model. Firstly, energy consumption in EUDC driving cycle has found with the help of developed vehicle model for the electric vehicle. Then, HC emissions have obtained from released emissions from plants with the consideration of high tension line losses and battery charge losses. Then, as seen in Figure-6, electric vehicle and conventional engine vehicle data have compared. HC emission releasing value decreased from 26.5 g/100 km to 1.6 g/100 km with the using electric vehicle according to obtained results.
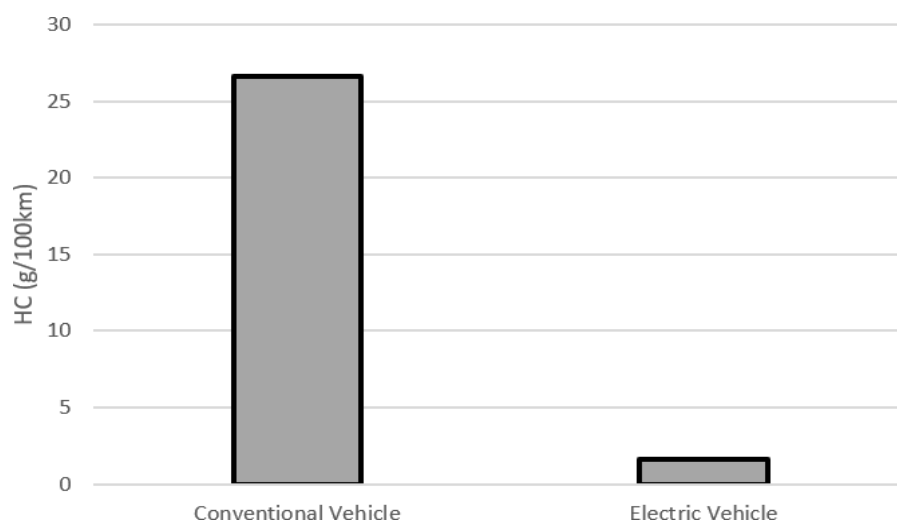
Figure-6 Comparison of HC emission data for conventional internal combustion engine vehicle and electric vehicle

NO$_x$ Emissions

Firstly, internal combustion engine model has generated with the help of AVL Boost software. Then, vehicle model has set up with Matlab-Simulink model and NO$_x$ emission data have obtained. Then, , energy consumption in EUDC driving cycle has found with the help of the developed vehicle model with Matlab-Simulink software for the electric vehicle with consideration of yield maps of electric engine, battery and invertor. After than, emission data from electric vehicle have found with consideration from released emissions from plants. Emission data of electric vehicle in NEDC cycle and conventional vehicle are given in Figure-7. NO$_x$ emission releasing value increased from 23.8 g/100 km to 25.1 g/100 km with the using electric vehicle according to obtained results.
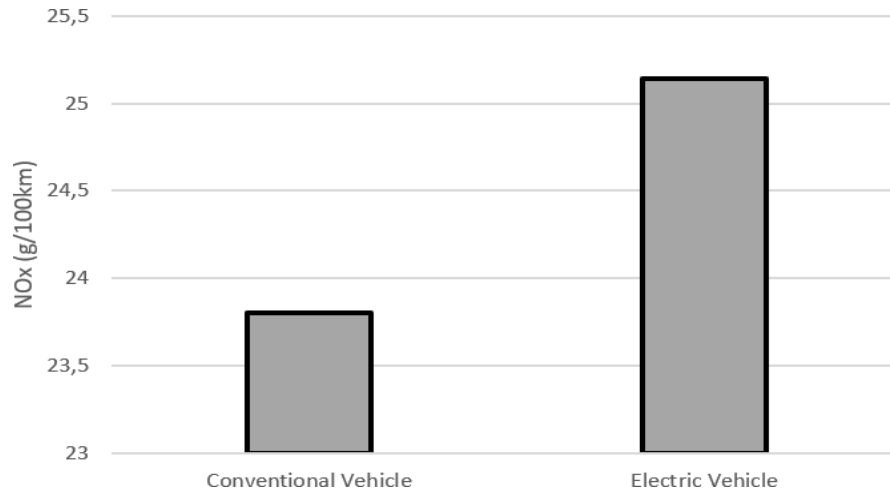
Figure-7 Comparison of NO$_x$ emission data for conventional internal combustion engine vehicle and electric vehicle

Conclusion

Engine maps have generated with the help of multi cylinder engine data that obtained with the validation of theoretical engine model with the help of one cylinder engine in the performed study. Then, vehicle model has developed with the help of Matlab-Simulink. After than, emission data have obtained with the consideration of model that developed for vehicle in Matlab-Simulink and energy consumption data and plant emission data. Right after, energy consumption and emission data (CO, HC and NO$_x$) obtained from EUDC driving cycle for the electric vehicle and conventional internal combustion engine have compared.

Obtained results are summarized below.

● Energy consumption value with electric vehicle usage value decreased from 45.45 kWh/100 km to 21.80 kWh/100 km.
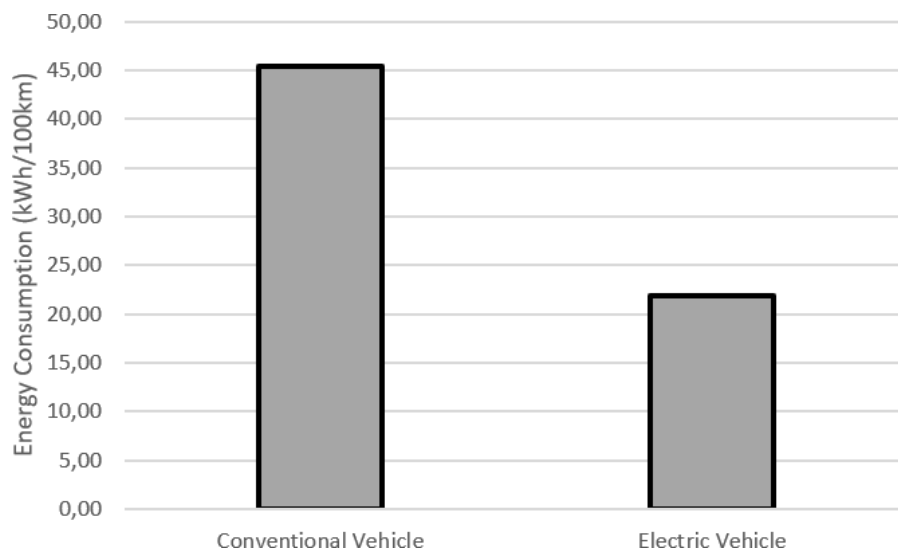
● CO emission releasing value decreased from 1849.0 g/100 km to 11.9 g/100 km with the using electric vehicle.

● HC emission releasing value decreased from 26.5 g/100 km to 1.6 g/100 km with the using electric vehicle.

● NO$_x$ emission releasing value increased from 23.8 g/100 km to 25.1 g/100 km with the using electric vehicle.

REFERENCES

[1] Yan-TaoZhang, Christian G. Claudel, Mao-Bin Hu, Yu-Hang Yu, Cong-Ling Shi. Develop of a fuel consumption model for hybrid vehicles. Energy Conversion and Management. Volume 207. 1 March 2007. 112546

[2] Ying Yao, Xiaohua Zhao, Chang Liu, Jian Rong, Yunlong Zhang, Zhenning Dong, Yuelong Su. Vehicle Fuel Consumption Prediction Method Based on Driving Behavior Data Collected from Smartphones. Journal of Advanced Transportation. 23 March 2020. Volume 2020. Article ID 9263605 | https://doi.org/10.1155/2020/9263605

[3] D.Y.C. Leung, D.J. Williams. Modelling of Motor Vehicle Fuel Consumption and Emissions Using a Power-Based Model. Environmental Monitoring and Assessment. November 2000 Volume 65. pages21–29.

[4] Yuan-yuan Song, En-jian Yao, Ting Zuo, Zhi-feng Lang. Emissions and Fuel Consumption Modeling for Evaluating Environmental Effectiveness of ITS Strategies. Discrete Dynamics in Nature and Society. Volume 2013. Article ID 581945. https://doi.org/10.1155/2013/58194

[5] Gennaro Nicola Bifulco, Luigi Pariota, Francesco Galante, Maria Russo Spena. A Linear Model for the Estimation of Fuel Consumption and the Impact Evaluation of Advanced Driving Assistance Systems. 22 October 2020. Sustainability 2015, 7(10), 14326-14343; https://doi.org/10.3390/su71014326

[6] Turkish Statistical Institute. (2010). TETC Electricity Generation - Transmission Statistics of Turkey. Date retrieved: 15.06.2013

[7] Turkish Statistical Institute. (2010). National Inventory Report. Date retrieved: 15.06.2013

CYCLE SKIPPING STRATEGIES FOR NATURAL GAS SI ENGINE

E. TUNÇER[1*], T. SANDALCI[1], Ş. PUSAT[1], Ö. BALCI[1], Y. KARAGÖZ[2]

[1] *Yildiz Technical University, Mechanical Engineering Department, Istanbul, Turkey.*

[2] *Istanbul Medeniyet University, Mechanical Engineering Department, Istanbul, Turkey.*

*erdaltuncer07@gmail.com

ABSTRACT

Cycle skipping in natural gas engine which has single cylindired, unsupercharged with 1.16 L natural volume, spark ignition type has worked in the performed study. Also, inlet manifold air has switched off during cycle skipping to minimize pumping loses in the performed study. Thus, both pumping loses has prevented and cycle skipping strategy has carried out and its effects on emission and fuel consumption have investigated. As a result of performed study, it is predicted that a significant improvement can be achieved in fuel consumption and emissions bu using cycle skipping strategies.

Keywords: *Cycle skipping, natural gas, spark ignition engine.*

INTRODUCTION

Investigation of alternative fuels in internal combustion engine and improvements in emissions and fuel combustion with different control strategies have continiued by researchers in nowadays. Some researchers have focused on alternative fuel powered engine, while other researches have aimed to improve performance and emissions with the different cycle and control strategies.

In internal combustion engines, less fuel consumption can be achieved by reducing pumping losses at partial loads using the cycle-skipping method. In the literature, there are some experimental and numerical studies on cycle-skipping strategies.

Kutlar et al. studied the cycle-skipping method for one cylinder spark ignition engine [1]. They developed a test system to evaluate cycle-skipping method on brake specific fuel consumption. They found that brake specific fuel consumption decresed about 11% at partial loads and engine may work at lower idle speed (about 45%) without any stability problem.

An experimental study was conducted to evaluate cycle-skipping method on pumping for internal combustion engines [2]. They investigated three different cycle-skipping modes on specific fuel consumption and exhaust emissions. They obtained significant improvements on brake specific fuel consumptions (4.3%), CO emissions (39%) and HC emissions (12.1%).

Baykara et al. studied the cycle-skipping method with a valve-control mechanism for spark ignition engines experimentally [3]. They concluded that cycle-skipping method is useful for fuel consumption reduction at partial loads. The brake specific fuel consumption decreased about 14% and 26% at lower and higher loads, respectively. However, THC emissions significantly incresed by cycle-skipping method.

A numerical study was performed to evaluate cycle-skipping method with variable valve timing strategy [4]. They aimed to get decrease in the emissions. They applied different strategies and obtained significant improvements on NOx emissions up to 39.4%.

Abas et al. investigated the cycle-skipping method on fuel consumption and emissions at partial loads experimentally [5]. They concluded that CO2 emissions reduced up to 5.7% and HC emissions reduced up to 6.8% at an idle speed.

In the performed study, cycle skipping has worked in natural gas fuel, single cylindired internal combustion engine with cycle skipping strategies unlike many studies in literature. Also, intake air has switched off with the help of solenoid valve that placed into intake manifold. Both selenoid valves in intake manifold and control unit of internal combustion engine were controlled with the microcontroller based electronic card developed by our project team.

Test Engine

1.16 L, unsupercharged, gas injectored, natural gas type test engine has used during experiments. Test engine specifications are given in Table-1.

Table-1 Test Engine Specifications

Engine brand	Erin Motor
Number of cylinder	1
Cylinder volume (L)	1.16
Bore (mm)	108
Stroke (mm)	127
Max power (kW)	10 kW @ 1500 rpm
Cooling system	Water
Aspiration system	Naturally aspiration

Testing Set

Eddy-current (APICOM FR50) type Professional engine dynomameter has used during performed studies. Dyno has both PID control system and it can be able to upload cycle based and load based, and both load and speed cycle based engine. Also, emissions have measured with Bosch BEA 060 5 gas analiyser. Kistler 6250C type pressure sensor has used to measure combustion chamber pressure of engine. Also Kistler charge amplifier has used. In-cylinder pressure datas have gathered with Teledyne T3DSO1104 4 channel oscilloscope. Measurements have applied with Newflow TLF series mass gas flow meter that is calibrated according to natural gas. Experimental results have gathered with National Instruments data collection system and Labview software. Picture of testing set are given in Figure-1.

Figure-1 Picture of testing set

Design of Experiment

Three separate conditions have tested in the performed study, The first is normal work, second is three normal one cycle skipping and third is two normal one cycle skipping working conditions. Summary of studies are given in Table-2. All the studies have applied in 1100 rpm revolutions. Engine has adjusted 1.6 kW constant brake load.

Table-2 Design of experiment

	Engine Speed (rpm)	Brake Engine Power (kW)
Normal	1100	1.6
3N 1S	1100	1.6
2N 1S	1100	1.6

Intake Air and Control Units

In the performed study, as seen in Figure-2, a lot of gas enjectors have placed in intake manifold and with the electronic control unit developed by our project team, the gas injectors have turned off during the cycle skipping and the intake air has cut off. Engine's control unit has developed by our project team, and gas enjectors have kept closed during cycle skipping so that natural gas fuel is not sprayed into the cylinder. Thus, cycle skipping has applied by cut of both fuel and air intake simultaneously.

Figure-2 View of gas injectors have placed in intake manifold and the electronic control unit

Results and Discussions

Cycle skipping strategies have been worked in single cylindired, spark ignition typed, unsupercharged engine in the performed study. Normal working condition, 3 Normal 1 cycle skipping condition (3N 1S) AND 2 Normal 1 cycle skipping condition (2N 1S) have been tested. Inlet of intake aitr has cut off with gas injectors which were placed intake manifold so that pumping losses have minimized. Fuel conpumption, CO emission, HC emission and NO_x emissio values are given comparatively.

Fuel Consumption

Fuel consumption datas in performed study are given in Figure-3. According to results, natural gas consumption of engine in normal condition, 3N 1S condition and 2N 1S condition have measured as 24 L/min, 19 L/min and 18 L/min respectively. According to results, it were determined that fuel consumption decreases when cycle skipping number increases. Fuel consumption decreased 20.8% and 25% in 3N 1S and 2N 1S operation conditions respectively compared to normal conditions. The most important reason for the obtained result is to work with a richer mixture and higher load in order to obtain the same power with cycle skipping and to remove burnt gases in a better way with cycle skipping.
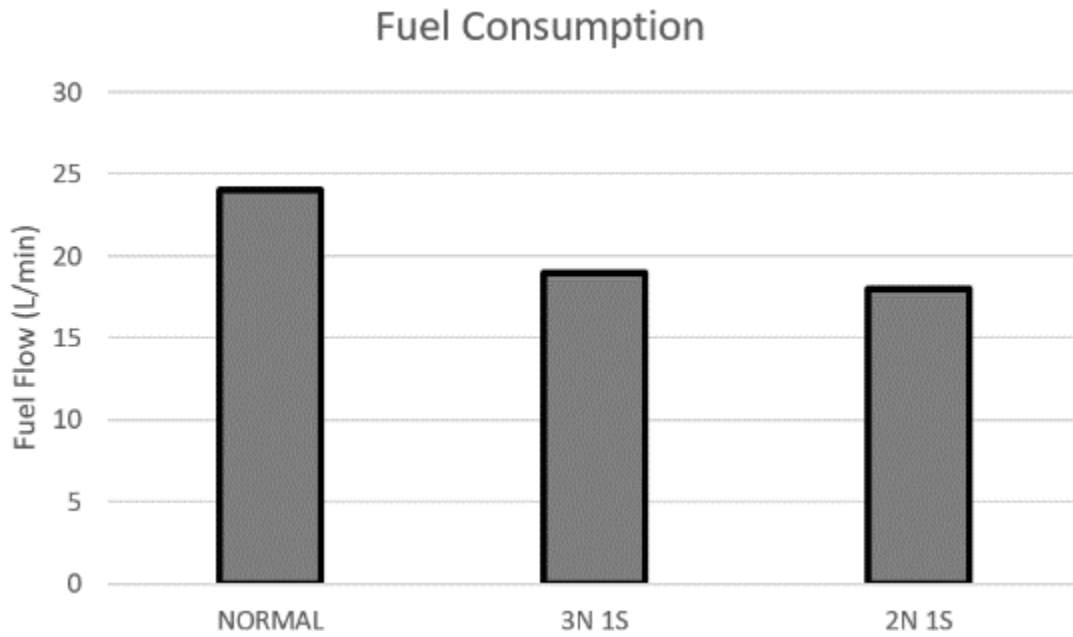
Fuel Consumption

Figure-3 The comparison of engine fuel consumption

CO Emissions

CO emission datas in performed study are given in Figure-4. According to results, CO emissions of engine in normal condition, 3N 1S condition and 2N 1S condition have measured as 0.026 %vol., 0.505 %vol. and 1.756 %vol. respectively. According to results, it were determined that CO emissions increases when cycle skipping number increases. The reason for this, to obtain same power with cycle skipping,rich mixture is formed by increasing the amount of fuel sprayed to the cylinders per unit cycle.

CO
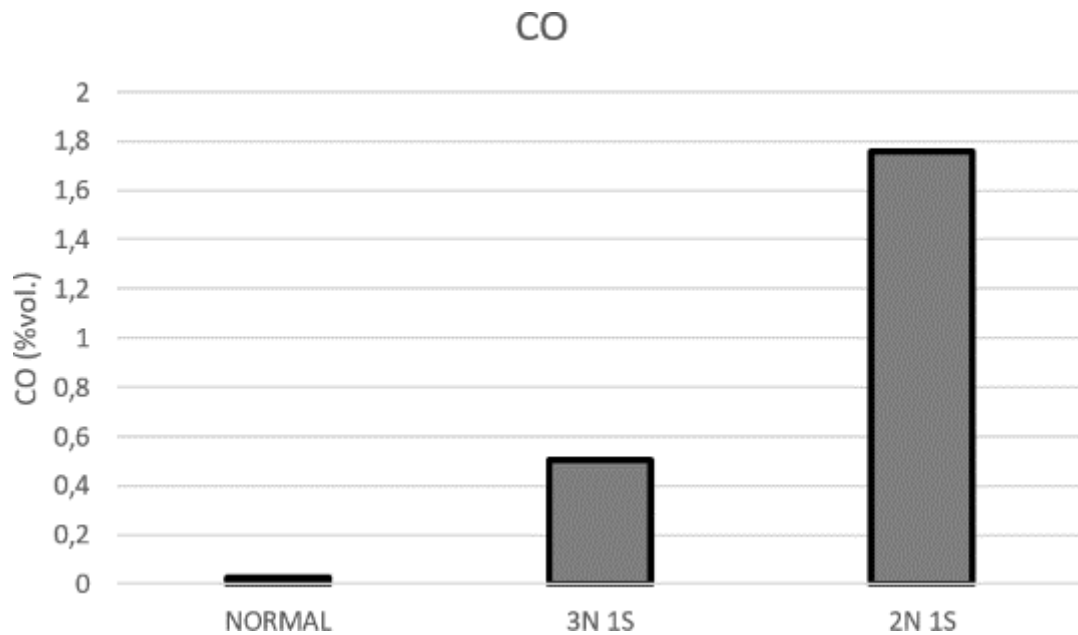
Figure-4 The comparison of CO emission values

HC Emissions

HC emission datas in performed study are given in Figure-5. According to results, HC emissions of engine in normal condition, 3N 1S condition and 2N 1S condition have measured as 146 ppm, 133 ppm and 313 ppm respectively. According to results, HC emissions reduce when the cycle skipping number is 3N 1S and HC emissions increases according to normal working conditions when the cycle skipping is 2N 1S. It is predicted that the reason of reducing HC values is that the excessive enrichment of fuel.
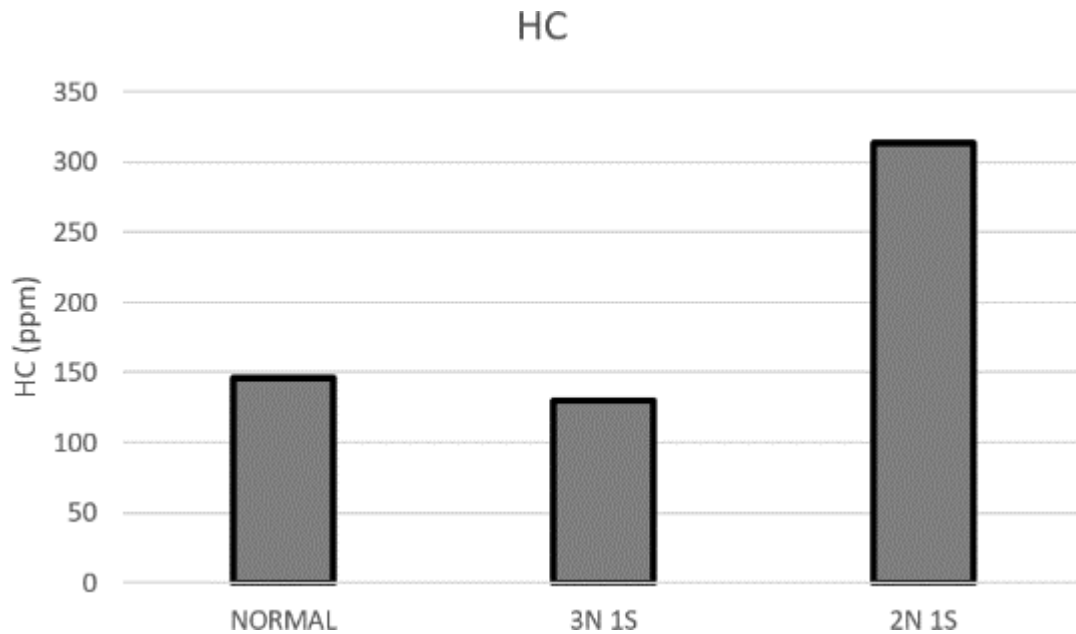
Figure-5 The comparison of HC emission values

NO$_X$ Emissions

NO$_x$ emission datas in performed study are given in Figure-6. According to results, NO$_x$ emissions of engine in normal condition, 3N 1S condition and 2N 1S condition have measured as 22 ppm, 127 ppm and 225 ppm respectively.According to results, it were determined that NO$_x$ emissions increases when cycle skipping number increases. The reason for this, to obtain same power, more fuel is injected into the cylinder so the pressure inside cylinder increaes.
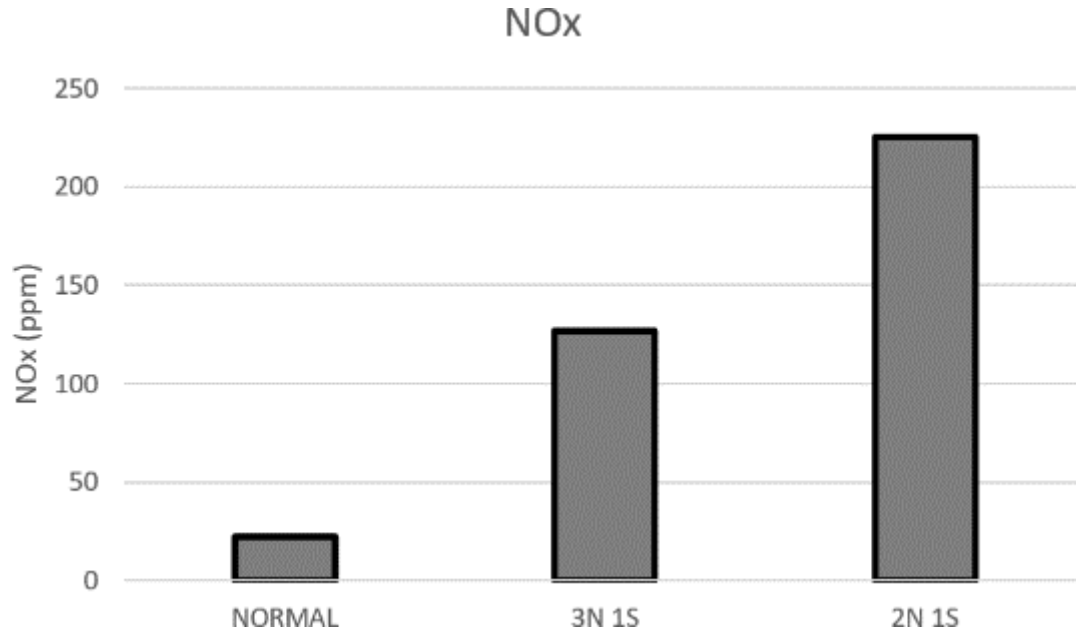
Figure-6 The comparison of NOx emission values

Conclusion

Single cylindired, natural gas, unsupercharged, spark ignition engine under normal condition, 3N 1S and 2N 1S conditions the intake air has cut of during the cycle skipping and fuel consumption, CO, HC and NO_x emissions have compared, Obtained results have summarized below.

● Fuel consumption decrease 20.8% and 25% in 3N 1S and 2N 1S operation conditions respectively compared to normal conditions.

● CO emissions of engine in normal condition, 3N 1S condition and 2N 1S condition have measured as 0.026 %vol. 0.505 %vol. and 1.756 %vol. respectively.

● HC emissions of engine in normal condition, 3N 1S condition and 2N 1S condition have measured as 146 ppm, 133 ppm and 313 ppm respectively.

● NO_x emissions of engine in normal condition, 3N 1S condition and 2N 1S condition have measured as 22 ppm, 127 ppm and 225 ppm respectively.

REFERENCES

[1] Kutlar OA, Arslan H, Calik AT. Skip cycle system for spark ignition engines: an experimental investigation of a new type working strategy. Energy Conversion and Management 2007; 48: 370–379.

[2] Yüksek L, Özener O, Sandalcı T. Cycle-skipping strategies for pumping loss reduction in spark ignition engines: An experimental approach. Energy Conversion and Management 2012; 64: 320-327.

[3] Baykara C, Kutlar OA, Dogru B, Arslan H. Skip cycle method with a valve-control mechanism for spark ignition engines. Energy Conversion and Management 2017; 146: 134-146.

[4] Dogru B, Lot R, Ranga Dinesh KKJ. Valve timing optimisation of a spark ignition engine with skip cycle strategy. Energy Conversion and Management 2018; 173: 95-112.

[5] Abas NA, Tamaldin N, Yamin AKM. Experimental Investigation Of Cylinder Deativation Impact On Engine Performance And Emission For SI Engıne. ARPN Journal of Engineering and Applied Sciences 2019; 14-2: 470-475.

STUDY ON ENGINE WASTE-HEAT RECOVERY FOR AUTOMOBILE AIR-CONDITIONING

Hafiz Muhammad Asfahan[1], Muhammad Sultan[1,*], Hasan Köten[2], Yasin Karagoz[2]

[1] *Bahauddin Zakariya University, Laboratory for Energy and Env. Engineering Research, Agricultural Engineering Department, Multan 60800, Pakistan*

[2] *Istanbul Medeniyet University, Mechanical Engineering Department, Istanbul, Turkey.*

*muhammadsultan@bzu.edu.pk

ABSTRACT

More than half of the heat generated in internal combustion engines (ICEs) is wasted into the surrounding environment. Effective recovery of such heat from automobiles is a key approach to mitigate energy and to sustainable technology. This study investigates its possible use for automobile indoor air conditioning (AIAC) from the viewpoint of adsorption heat pump systems. The study explores the fundamentals and application of adsorption heat pumps for automobile air-conditioning. As the regeneration temperature is the success key for adsorption heat pumps, therefore, this study investigates optimum adsorbent-refrigerant pair which could be employed for recovery of the engine waste heat efficiently. The studied class of adsorbent-refrigerant pairs are (i) silica gel-water (ii) zeolite-water and (iii) PS II-water. Moreover, the study insights the maximum cooling potential associated to former classes of adsorbent-refrigerant pair for AIAC. The study experimentally investigates the adsorption isotherms of locally available silica gel and compare it with other adsorbent-refrigerant pair studied in literature. Steady state ideal cycle analysis is performed to determine the suitable adsorbent-refrigerant pair for AIAC. The study finds all the three studied adsorbent-refrigerant pair are effectively regenerated (55-80℃) from engine waste heat. However, zeolite-water pair is suitable adsorbent-refrigerant pair having cooling potential of 501.5kJ/kg followed by polymer-water pair and silica gel-water pairs.

Keywords: Engine Waste Heat Recovery, Automobile Air-Conditioning, Adsorption Cooling, Adsorbent-Refrigerant Pairs.

1.INTRODUCTION

Due to rapid increase in agricultural mechanization, industrialization and living standards, engines are commonly used for the combustion of fossil fuels. However, after combustion, the fossil fuels contain toxic gasses (i.e., CO, CO_2, NOx, SO_2 etc.) that deteriorate environment. Generally, internal combustion engines (ICEs) are used in automobiles. However, its efficiency is limited due to inefficient use of heat generated during power stroke. About 60 to 70% of heat generated in ICEs has been wasted by exhaust pipe and engine refrigerant/cooling circuit into the surrounding environment [1], [2]. In literature, it is reported that, the waste heat emitted from engine cooling circuit as well as from exhaust pipe have temperature ranges between 100 to 150℃ and 400 to 800℃, respectively which can be potentially utilized as a low grade waste heat for automobile indoor air conditioning (AIAC). Although, various technologies regarding AIAC are in practiced but vapor

compression-based air conditioning (VCAC) system are widely used technology. The VCAC system consumes extra fuel for operating of compressor, electricity driven fans and consequently contributing more CO_2 gas emission (4-8% on yearly basis) that causes ozone depletion (OD). In some studies, adsorption heat pump (AHP) is proposed as alternative option for AIAC [1], [3]–[7]. Unlike VCAC system, AHP contains adsorbent material which behaves as a vapor compressor (increasing temperature and pressure). These materials possess dual properties (i.e. hydrophilic at low temperature and hydrophobic at high temperature). The performance of AHP primary depends upon the adsorbent-refrigerant pairs. Many researchers are studied to find the suitable adsorbent-refrigerant pair for AIAC [3], [8]–[15]. The summary of their findings is furnished in table 1. Till now activated carbon-ammonia pair shows the highest specific cooling energy (SC) of 800 W/kg and regenerated it at 90°C. However, refrigerant emanates greenhouse gasses which causes serious environmental risks. Whereas, water is most sustainable refrigerant which is used in adsorption heat pump for air conditioning. Therefore, the present study utilize water as refrigerant for AIAC. Moreover, the experimentally investigates the adsorption isotherms of silica gel at different regeneration temperature. The study explores the suitable adsorbent-refrigerant pair for AIAC from the perspectives of low regeneration temperature and high specific cooling energy (SCE).

2. WORKING PRINCIPLE OF ENGINE WASTE HEAT DRIVEN ADSORPTION HEAT PUMP

Waste heat driven adsorption heat (ACs) consist of thermal compressor (i.e. adsorption/desorption material/bed), condenser, expansion valve evaporator and engine heat recovery circuit. The thermal compressor adsorbs refrigerant coming from the evaporator during adsorption phase. When the adsorbent material gets saturated its adsorption capacity decreases which leading it towards the desorption phase. In doing so, firstly adsorption bed is preheated to achieve the condenser's temperature and pressure by closing the outlet valve of adsorption bed. The waste heat which coming from engine cylinder is circulated in desorption bed via heat exchanger to regenerate the adsorbent material. Figure 1 shows the working principle of engine waste heat driven adsorption cooling system. Desorb refrigerant having high temperature and pressure directed towards the condenser to reduces its temperature. Afterward, the refrigerant moves towards the expansion valve where its temperature and pressure further reduced. The chilled refrigerant is utilized for producing cooling effect in automobile cabin by circulating it through heat exchanger. For completion of cycle the refrigerant which receives heat from the cabin is directed into the evaporator.
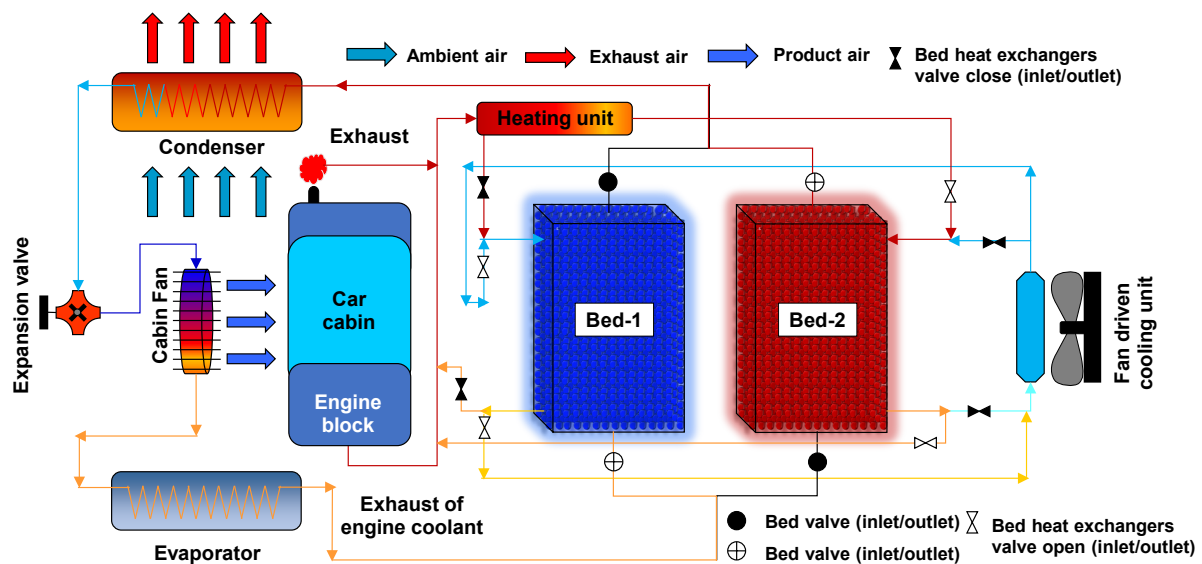

Figure 1: Working principle of adsorption cooling system for automobiles

Adsorbent-Refrigerant	Methodology	Regenertion temperature [°C]	SCP [W/kg]	COP [-]	Ref.
Activated carbon-methanol	Theo.	200	400	0.25	
Activated carbon-ammonia	Exp.	90	650 – 800	0.22	
Silica gel-water	Exp.	87	208	0.62	
Zeolite 13-water	Exp.	200	25.7	0.38	
Zeolite 13X-water	Exp.	350	200	-	
Silica gel-water	Exp	85	0.37	0.32	[16]
AQSOA Z01-water		70	0.32	0.36	[16]
AQSOA Z02-water	Mod.	90	0.52	0.36	[16]

Table 1: adsorbent-refrigerant pair conventionally used for automobile air conditioning

3. METHODOLOGY

3.1 EXPERIMENTS

Locally available granular type silica gel (adsorbent material) is experimentally evaluated in laboratory for Energy and Environmental Engineering research (EEER-Lab) for measuring the maximum adsorption of water vapors on adsorbent material. The studied silica gel has bulk density of 919.5 kg/m3 and average pore radius of 1.4mm. Sample of adsorbent material is first dehydrated by putting it into oven at specific temperature for some duration. By performing a series of experiments, the temperature and duration are optimized until the change in weight of the adsorbent material becomes negligible. For the time being, at a known temperature and relative humidity, the dehydrated adsorbent material is put in the adsorption chamber. Once the adsorbent material is fully saturated, the temperature and relative humidity values are recorded. The amount of water vapors adsorbed at that temperature and relative humidity are measured by taking difference between the weight of adsorbent material at saturation and drying conditions. Whereas the maximum amount of vapors adsorbed per kilogram of adsorbent are determined by taking the ratio of net weight of water vapors adsorbed to the dry weight of adsorbent material.

The process is repeated several times at various temperatures and relative humidity conditions in order to obtain data regarding maximum water vapors uptake by adsorbent material. The adsorption isotherms of silica gel-water pair ranges between 20°C to 100°C are presented in Figure 2. Thus, adsorption isotherm data are modeled with Guggenheim, Anderson, De-Boer (GAB) model (discussed in section 3.3) to investigate the performance parameters of adsorption cooling system driven by engine waste heat.

3.2 ADSORBENT-REFRIGERANT PAIR

Adsorption isotherms of silica gel-water pair are experimentally measured in EEER-lab and perform the ideal cycle analysis to determine the potential of silica gel-water pair in adsorption cooling system driven by engine waste heat. Moreover, two adsorbents i.e. zeolite (AQSOA-Z02) and polymer (PS II) from the literature are corelated with silica gel to identify the optimum adsorbent for adsorption cooling system driven by engine waste heat [17], [18]. These materials possess high hydrophilic characteristics and adsorb 4.48 time (PS II) and 1.5 times (zeolite) more water vapors as compared to silica gel. Dubbinin-Astakhov (D-A) model are used for ideal

cycle analysis both zeolite-water and PS II-water pair, respectively. The isothermal constants of GAB and D-A model are furnished in Table 1.

Table 1: Isothermal constants of adsorbent-refrigerant

Adsorbent-refrigerant pairs	Isotherm model	Parameters	Value	References
Zeolite-water	D-A	W_o [kg kg^{-1}]	1.98	[17]
		E [kJ kg^{-1}]	90	
		n [-]	1.5	
PS II-water	D-A	W_0 [kg kg^{-1}]	1.76	[18]
		E [kJ mol^{-1}]	41.84	
		n [-]	0.50	
Silica gel-water	GAB	W_{mo} [kg kg^{-1}]	0.138	This study
		q_m [kJ kg^{-1}]	0.371	
		C_o [-]	0.285	
		K_o [-]	149.43	
		ΔH_c [kJ kg^{-1}]	385.86	
		ΔH_k [kJ kg^{-1}]	-148.44	

3.3 ADSORPTION ISOTHERM MODEL

In this study, D-A and GAB model is used to measure the adsorption isotherms. The D-A model is used to model the adsorption isotherms of zeolite-water and PS II-water isotherms whereas, GAB model is used for silica gel. The equation of D-A isotherm model is given as Eq. (1):

$$q = q_o \, exp \left\{ -\left(\frac{A}{E}\right)^n \right\} \tag{1}$$

where A, E and n adsorption potential, characteristic energy and structural heterogeneity parameters respectively. While q, q_o are the equilibrium adsorption uptake and maximum water uptake by adsorbent material. Adsorption potential can be further calculated by using Eq. (2):

$$A = RT \, ln \left(\frac{P_o}{P}\right) \tag{2}$$

Where, P_o and P are the saturation pressure and equilibrium pressure, respectively. Whereas T is the adsorption temperature at which the regurgitant adsorbs on the adsorbent material and R is the gas constant. Likewise, GAB model is presented as

$$q = \frac{q_m \, C \, K(P/P_o)}{\left(1 - K(P/P_o)\right)\left(1 - K(P/P_o) + CK(P/P_o)\right)} \tag{3}$$

$$q_m = q_{mo} \, exp \left(\frac{w_m}{RT}\right) \tag{4}$$

$$C = C_o \, exp \left(\frac{\Delta H_c}{RT}\right) \tag{5}$$

$$K = K_o \, exp \left(\frac{\Delta H_k}{RT}\right) \tag{6}$$

where, q_m shows the adsorption of refrigerant to form monolayer on the adsorbent material, and ΔH_c and ΔH_k are functions related to water sorption heat. Whereas, C, C_o, K and K_o are constants related to heats.

3.4 Ideal cycle time independent model

Specific cooling energy (SCE) and coefficient of performance (COP) of studied adsorbent material are calculated using ideal cycle time independent model to determine the suitable adsorbent-refrigerant pair for automobile air conditioning [18]. Dühring diagram is constructed which presents the ideal cooling cycle of adsorbent-refrigerant pair. SCE of adsorption cycle is determined by Eq. (7).

$$SCE = (q_{max} - q_{min}) \left\{ LH_{Te} - \int_{Te}^{Tc} C_{P_{ref}} \, dT \right\} \tag{7}$$

where, q_{max} and q_{min} are maximum and minimum adsorption of refrigerant on the adsorbent material respectively. While LH_{Te} are the enthalpy of vaporization at evaporator temperature. And C_{Pref} is the specific heat capacity of refrigerant. The heat added to adsorbent material during adsorption is calculated as:

$$Q_{ads} = \int_{T_1}^{T_3} C_{P_{ads}} \, dT \tag{8}$$

where, C_{Pads} is termed as specific heat capacity of refrigerant and Q_{ads} is the heat added to adsorbent material. The heat added in adsorbent material during preheating, regenerating and adsorption of refrigerant on the adsorbent material is calculated by Eq. (9), Eq. (10) and Eq. (11) respectively. The total heat added (Q_T) is the summation of former terms.

$$Q_{pre} = q_{max} \int_{T_1}^{T_2} C_{P_{ref}} \, dT \tag{9}$$

$$Q_{des} = \int_{T_2}^{T_3} q . C_{P_{ref}} \, dT \tag{10}$$

$$Q_{adsr} = \int_{q_{min}}^{q_{max}} Q_{st} \, dq \tag{11}$$

where, Q_{st} in Eq. (11) is termed as isosteric heat adoption calculated by the Eq. (12).

$$\frac{Q_{st}}{R} = \left[\frac{\partial lnP}{\partial(1/T_{ads})} \right]_q \tag{12}$$

The COP of the cycle is determined by taking the ratio of *SCE* to the summation of Q_T and Q_{ads} calculated:

$$COP = \frac{SCP}{Q_{ads+}Q_T} \tag{13}$$

4. RESULTS AND DISCUSSION

The study experimentally determines the adsorption isotherms of silica gel-water pair at adsorption temperature ranges between 20 to 100 °C as presented in Figure (a). GAB moel is used to model the adsorption isotherms of silica gel. Model constants are furnished in Table 1. The maximum vapors uptake is observed as 0.18 kg of water per kg of silica gel at adsorption temperature of 20 °C Whereas, the maximum water vapors adsorb on the zeolite and PS II is reported 0.285 kg of water per kg of zeolite and 0.8 kg of water per kg of polymer [17], [19].

The adsorption isotherms of zeolite-water pair and PS II-water pair is presented in Figure 2(b), (c) respectively. It is observed that as the adsorption temperature increases the ability of the material to adsorb water vapors decreases. However, the adsorbent materials have maximum hydrophilic characteristics at temperature ≤30 ℃ and pressure ≤10kPa. The zeolite-water pair and PS II-water pair depicts type-I and type-III adsorption isotherm respectively according to IUPAC classification. Whereas, the silica gel-water pair depicts type-II adsorption isotherms.

Ideal cycle analysis is performed to identify suitable adsorbent-refrigerant pair for automobile air conditioning. Dühring diagram of each pair developed by using the adsorption isotherm constants/parameters and results of ideal cycle analysis are superimposed on the Dühring diagram as shown in Figure 3. The process 1-2 in Dühring diagram of each adsorbent-refrigerant pair represents the isosteric heat of desorption or it is also termed as switching time of the bed. Form the previous adsorption cycle the bed is completely saturated and needs to regenerate. The process 2-3 shows the isobaric heat of desorption. The waste heat recovered from the engine exhaust are utilized to regenerate the adsorption material. The process 3-4 is termed as isosteric heat of adsorption or it is also called the switching time. During this process the material is get ready to adsorb by circulating ambient air into the adsorption material. The process 4-1 is termed as isobaric heat of adsorption. It is observed that all the adsorbent-refrigerant pairs are regenerated at a temperature range between 55 to 80 ℃. However, in terms of adsorption capacity PS II-water pair is more suitable candidate (0.80 kg/kg) Whereas in terms of SCE zeolite-water pair produce high cooling (501.41kJ/kg) followed by PS II-water pair (409.55kJ/kg) and silica gel-water pair (99.863kJ/kg) due to maximum concentration difference (Δq) between saturated (q_{max}) and minimum (q_{min}) adsorption uptake of ideal adsorption cycle. Higher COP value also attributed to zeolite water pair (0.715) followed by PS II-water pair (0.660) and silica gel-water pair (0.509) respectively as shown in Figure 4.
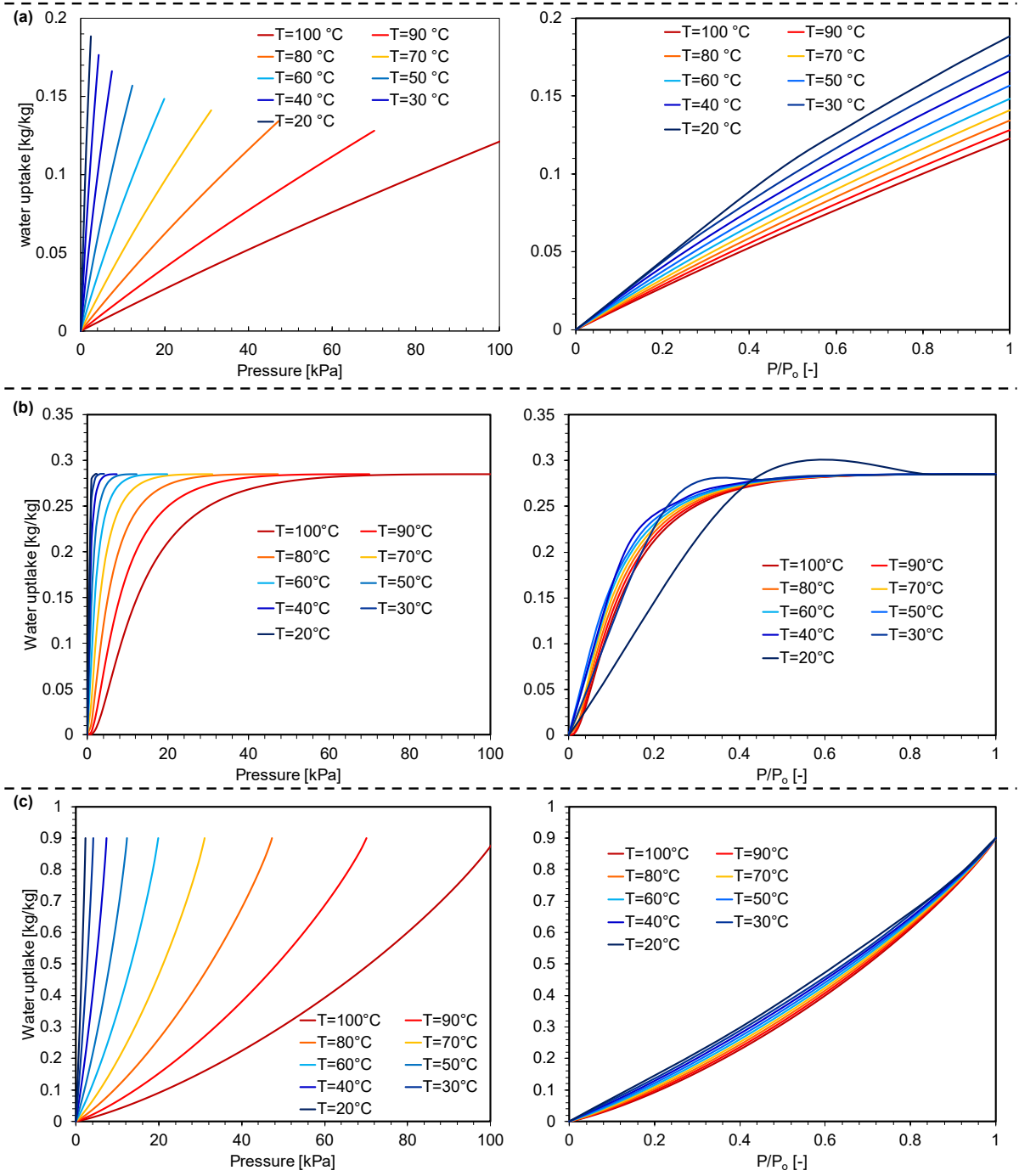
Figure 2: Adsorption isotherms of (a) silica gel-water pair (b) zeolite-water pair (c) PS II-water pair with respect to pressure on left and relative pressure on right
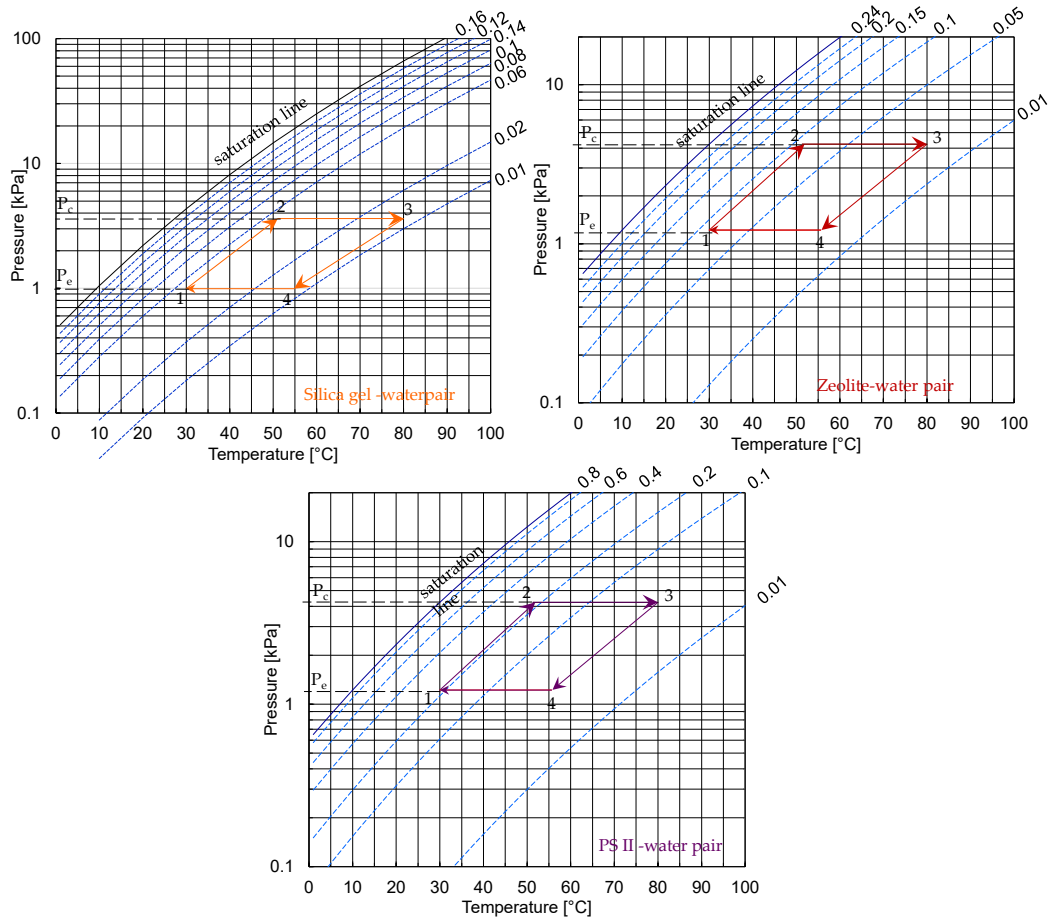
Figure 3: Dühring diagram and results of ideal cycle analysis silica gel-water pair, zeolite-water pair and PS II-water pair respectively.
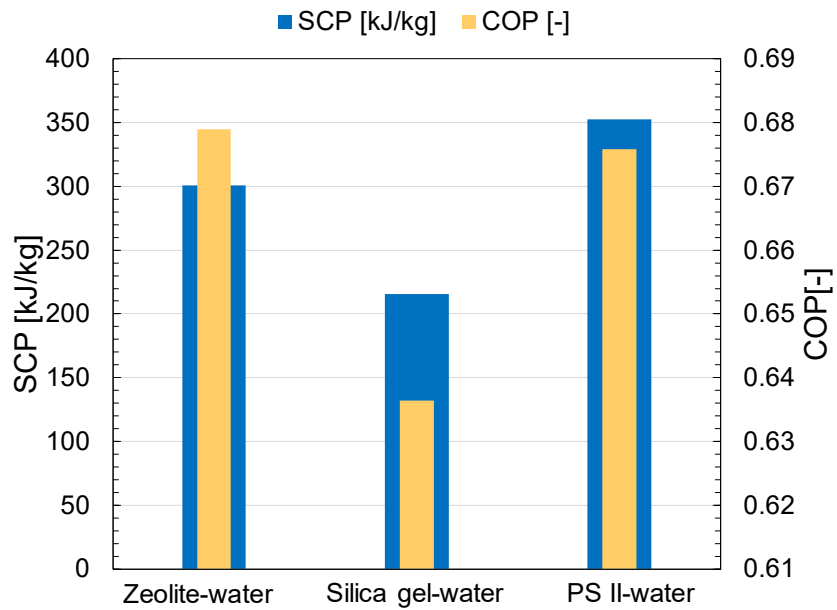
Figure 4: Comparison between studied adsorbent-refrigerant

5.CONCLUSION

The present study experimentally investigates the adsorption isotherm of silica gel water pair in EEER-Lab. The isotherms of silica gel-water pair have been modeled using GAB model. In addition, the study modeled the

adsorption isotherms of zeolite-water pair and PS II-water pair at temperature ranges between 20 to 100 oC temperature. Ideal cycle analysis is performed to investigate the suitable adsorbent-refrigerant candidate for automobile air conditioning driven by engine waste heat. The study finds that all three studied materials are efficiently regenerated (55-80oC) by low grade waste heat released from the engine cooling system having temperature□100 oC. However, zeolite water pair produce maximum specific cooling energy (SCE) of 501.4kJ/kg as compared to other adsorbents. Moreover, the coefficient of performance (COP) of the zeolite water pair is 0.715 which emphasize its applicability for adsorption-based automobile air conditioning system.

REFERENCES

[1] L. Z. Zhang, "Design and testing of an automobile waste heat adsorption cooling system," *Appl. Therm. Eng.*, vol. 20, no. 1, pp. 103–114, 2000, doi: 10.1016/S1359-4311(99)00009-5.

[2] S. Maeda, K. Thu, T. Maruyama, and T. Miyazaki, "Critical review on the developments and future aspects of adsorption heat pumps for automobile air conditioning," *Appl. Sci.*, vol. 8, no. 11, 2018, doi: 10.3390/app8112061.

[3] W. D. Wu, H. Zhang, and C. L. Men, "Performance of a modified zeolite 13X-water adsorptive cooling module powered by exhaust waste heat," *Int. J. Therm. Sci.*, vol. 50, no. 10, pp. 2042–2049, 2011, doi: 10.1016/j.ijthermalsci.2011.05.005.

[4] M. A. Lambert and B. J. Jones, "Automotive adsorption air conditioner powered by exhaust heat. Part 1: Conceptual and embodiment design," *Proc. Inst. Mech. Eng. Part D J. Automob. Eng.*, vol. 220, no. 7, pp. 959–972, 2006, doi: 10.1243/09544070JAUTO221.

[5] M. A. Lambert and B. J. Jones, "Automotive adsorption air conditioner powered by exhaust heat. Part 2: Detailed design and analysis," *Proc. Inst. Mech. Eng. Part D J. Automob. Eng.*, vol. 220, no. 7, pp. 973–989, 2006, doi: 10.1243/09544070JAUTO222.

[6] A. Sharafian and M. Bahrami, "Assessment of adsorber bed designs in waste-heat driven adsorption cooling systems for vehicle air conditioning and refrigeration," *Renew. Sustain. Energy Rev.*, vol. 30, pp. 440–451, 2014, doi: 10.1016/j.rser.2013.10.031.

[7] R. E. Critoph, S. J. Metcalf, and Z. Tamainot-Telto, "Proof of concept car adsorption air-conditioning system using a compact sorption reactor," *Heat Transf. Eng.*, vol. 31, no. 11, pp. 950–956, 2010, doi: 10.1080/01457631003604459.

[8] M. M. Younes, I. I. El-Sharkawy, A. E. Kabeel, and B. B. Saha, "A review on adsorbent-adsorbate pairs for cooling applications," *Appl. Therm. Eng.*, vol. 114, no. November, pp. 394–414, 2017, doi: 10.1016/j.applthermaleng.2016.11.138.

[9] K. Fayazmanesh, C. McCague, and M. Bahrami, "Consolidated adsorbent containing graphite flakes for heat-driven water sorption cooling systems," *Appl. Therm. Eng.*, vol. 123, pp. 753–760, 2017, doi: 10.1016/j.applthermaleng.2017.05.114.

[10] A. Sharafian, S. M. Nemati Mehr, W. Huttema, and M. Bahrami, "Effects of different adsorber bed designs on in-situ water uptake rate measurements of AQSOA FAM-Z02 for vehicle air conditioning applications," *Appl. Therm. Eng.*, vol. 98, no. 2016, pp. 568–574, 2016, doi: 10.1016/j.applthermaleng.2015.12.060.

[11] B. Shi, R. Al-Dadah, S. Mahmoud, A. Elsayed, and E. Elsayed, "CPO-27(Ni) metal-organic framework based adsorption system for automotive air conditioning," *Appl. Therm. Eng.*, vol. 106, pp. 325–333, 2016, doi: 10.1016/j.applthermaleng.2016.05.109.

[12]   B. Shi, "Development of an Mof Based Adsorption Air Conditioning System for Automotive," 2015.

[13]   M. O. Abdullah, I. A. W. Tan, and L. S. Lim, "Automobile adsorption air-conditioning system using oil palm biomass-based activated carbon: A review," *Renew. Sustain. Energy Rev.*, vol. 15, no. 4, pp. 2061–2072, 2011, doi: 10.1016/j.rser.2011.01.012.

[14]   F. Shabir *et al.*, "Recent updates on the adsorption capacities of adsorbent-adsorbate pairs for heat transformation applications," *Renew. Sustain. Energy Rev.*, vol. 119, no. October 2019, p. 109630, 2020, doi: 10.1016/j.rser.2019.109630.

[15]   M. Sultan, T. Miyazaki, S. Koyama, and Z. M. Khan, "Performance evaluation of hydrophilic organic polymer sorbents for desiccant air-conditioning applications," *Adsorpt. Sci. Technol.*, vol. 36, no. 1–2, pp. 311–326, Feb. 2017, doi: 10.1177/0263617417692338.

[16]   S. M. Ali and A. Chakraborty, "Thermodynamic modelling and performance study of an engine waste heat driven adsorption cooling for automotive air-conditioning," *Appl. Therm. Eng.*, vol. 90, pp. 54–63, 2015, doi: 10.1016/j.applthermaleng.2015.06.078.

[17]   H. Wei Benjamin Teo, A. Chakraborty, and W. Fan, "Improved adsorption characteristics data for AQSOA types zeolites and water systems under static and dynamic conditions," *Microporous Mesoporous Mater.*, vol. 242, pp. 109–117, 2017, doi: https://doi.org/10.1016/j.micromeso.2017.01.015.

[18]   M. Sultan, T. Miyazaki, B. B. Saha, and S. Koyama, "Steady-state investigation of water vapor adsorption for thermally driven adsorption based greenhouse air-conditioning system," *Renew. Energy*, vol. 86, pp. 785–795, 2016, doi: 10.1016/j.renene.2015.09.015.

[19] S. Noor, H. Ashraf, M. Sultan, and Z. M. Khan, "Evaporative Cooling Options for Building Air-Conditioning: A Comprehensive Study for Climatic Conditions of Multan (Pakistan)," *Energies*, vol. 13, no. 12, p. 3061, 2020.

ENERGY EFFICIENCY AS AN CRUCIAL CONCEPT IN AUTOMOTIVE INDUSTRY

Ö. Boydak[1*], H. Köten[2]

[1,2]*İstanbul Medeniyet University, Mechanical Engineering Department, Istanbul, Turkey.*
*ozlem.boydak@medeniyet.edu.tr

ABSTRACT

Energy efficiency is rather crucial concept in terms of automotive industry which affect development and economy. Increasingly developing new energy efficient methods take significiant part in automotive manufacturing, which aims not only to reduce emissions to environment, but also to decrease production costs maintaining the quality of the product, and safety of the passengers in their vehicles, leading to customer satisfaction. In terms of energy efficiency concept in automotive industry, preventing leakage from the parts, designing environment friendly vehicles, efficient HVAC measures and energy management systems are some of the basic key points. Additionally, environment friendly low heat recovery system organic rankine cycle (ORC) implementation is useful for vehicle energy efficiency.

Vehicle research and development and energy management systems for energy-efficient automotive technology is of great priority in terms of energy efficiency. Thus, R&D issues are being studied deeply for automotive energy efficiency, such as fuel economy, developing hybrid specific engine and electromechanical coupling devices, implementation of high pressure common rail diesel engine, direct injection in cylinder gasoline engine, homogeneous combustion and turbo charging in terms of internal combustion engine technology, development of six stalls and more mechanical transmission, dual clutch automatic transmission, automatic control of commercial mechanical transmission through simulation control, breakthrough low resistance parts, lightweight materials and laser welding molding technology. Also, utilizing composites in design of vehicle components and their mechanical properties are of great importance. Additionally, energy saving vehicles through new energy automotive industry promote electric transformation of automotive power system as technology upgrade. Consequently, energy efficiency policies have been assigned to reduce energy consumption.

Keywords: *Energy Efficiency, Automotive Industry, Energy-Efficient Vehicle Technology, Energy Saving Vehicles.*

REFERENCES

[1] D. Castro, F. Parreiras, 'A review on multi-criteria decision-making for energy efficiency in automotive engineering', Applied Computing and Informatics, Emerald Publishing Limited 2210-8327.
[2] K. Katchasuwanmanee, R. Bateman and K. Cheng, 'An Integrated approach to energy efficiency in automotive manufacturing systems: quantitative analysis and optimisation', Production& Manufacturing Research, 2017, vol. 5, no. 1, p. 90–98.
[3] S. Oh, A. Hildreth, 'Estimating the Technical Improvement of Energy Efficiency in the Automotive Industry-Stochastic and Deterministic Frontier Benchmarking Approaches', Energies, 2014, 7, 6196-6222.
[4] C. Schmutzler, A. Krüger, F. Schuster, M. Simons, 'Energy efficiency in automotive networks: Assessment and concepts', IEEE Xplore, August 2010.
[5] D. Meike, M. Pellicciari, G. Berselli, A. Vergnano, L. Ribickis, 'Increasing the energy efficiency of multi-robot production lines in the automotive industry', IEEE Xplore, December 2012.
[6] D. Meike; L. Ribickis, 'Energy efficient use of robotics in the automobile industry', IEEE Xplore: December 2011.
[7] A. Hnatov, S. Arhun and S. Ponikarovska, 'Energy saving technologies for urban bus transport', International Journal of Automotive and Mechanical Engineering, Volume 14, Issue 4, pp. 4649-46664, December 2017.

[8] H.Teiwes, M. Rössinger, M. Gonter, C. Herrmann, S. Thiede, 'Data based analysis and improvement of energy efficiency in the automotive body shop', Journal of Cleaner Production, Volume 284, November 2020.

[9] N. Lutsey, D. Sperling, 'Energy Efficiency, Fuel Economy, and Policy Implications', Journal of the Transportation Research Board, Vol 1941, Issue 1, 2005.

[10] A. Modrea, S. Vlase, H. T.-Draghicescu, M. Mihalcica, M. R. Calin, C. Astalos, P. Maior 'Properties of advanced new materials used in automotive engineering', Optoelectronics and Advanced Materials – Rapid Communications Vol. 7, No. 5-6, May - June 2013, p. 452 – 455.

[11] R. McKenna, S. Reith, S. Cail, A. Kessler, W. Fichtner, 'Energy savings through direct secondary reuse: an exemplary analysis of the German automotive sector', Journal of Cleaner Production, Volume 52, August 2013, Pages 103-112.

[12] W. J. Joost, 'Reducing Vehicle Weight and Improving U.S. Energy Efficiency Using Integrated Computational Materials Engineering', JOM 64, 1032–1038 (2012).

[13] S. M. Lukic; J. Cao; R. C. Bansal; F. Rodriguez; A. Emadi, 'Energy Storage Systems for Automotive Applications', IEEE Transactions on Industrial Electronics, Volume: 55, Issue: 6, June 2008.

[14] F. Apostolos, P. Alexios, P. Georgios, S. Panagiotis, C. George, 'Energy Efficiency of Manufacturing Processes: A Critical Review', Procedia CIRP, Volume 7, 2013, Pages 628-633.

[15] C. I. P. Martínez, 'Energy efficiency in the automotive industry evidence from Germany and Colombia', Environment, Development and Sustainability volume 13, 2011, pages367–383.

[16] Q. Chang; G. Xiao; S. Biller; L. Li, 'Energy Saving Opportunity Analysis of Automotive Serial Production Systems (March 2012)', IEEE Transactions on Automation Science and Engineering, Volume: 10, Issue: 2, April 2013.

[17] K. Cheng, K. Katchasuwanmanee, 'An integrated approach to energy efficiency in automotive manufacturing systems: quantitative analysis and optimisation', Production & Manufacturing Research, 2017, 5, pp. 90 - 98.

[18] N. C. Strupp , J. Köhler ,N. C. Lemke , W. Tegethoff , R. M. Kossel, 'Energy Efficient Future Automotive Condenser Systems', 2010 International Symposium on Next-generation Air Conditioning and Refrigeration Technology, 17 – 19 February 2010, Tokyo, Japan

REAL-TIME TRAJECTORY CONTROL OF AN INDUSTRIAL SERVO MOTOR DEVELOPING FOR INDUSTRY 4.0 APPLICATIONS

S. Oner[1], G. Bayrak[1*], H. Meral[2], N.M.Saraç[2], E. Pehlivan[2], A. Şahiner[2]

[1]*Bursa Technical University, Department of Electrical and Electronics Engineering, Bursa, Turkey.*
[2]*Sibernetik R&D Center, Demirci Mh. Demirciyolu Cd. No: 58, Bursa, Turkey.*
gokay.bayrak@btu.edu.tr

ABSTRACT

Servo motors used in all areas of the industry are generally controlled by PLC. The increase in technological competitiveness on a global scale and the results of Industry 4.0 have led to the need to develop real-time monitoring, control, automation system and software using LabVIEW infrastructure instead of the standard PLC based automation system. As a result, it is aimed to increase reporting, real-time monitoring, graphing, testing, analysis and communication capabilities.

In this study, AC servo motor and a cylinder system connected to the shaft of the servo motor were used, and the trajectory control of the servo motor was performed in real time with LabVIEW. Then the commands to be given to the servo motor and information to be received from the servo motor were controlled by using LabVIEW with a communication protocol called Ads Server. TwinCAT program was used for the movement of the servo system on the control screen. Position, velocity information is displayed on the interface prepared with LabVIEW on the computer from the AC servo motor, through the servo driver via the industrial PC. All operations carried out via the developed LabVIEW interface ..

Keywords: Servo motor, trajectory control, real-time data acquisition and control

REFERENCES

[1]. R. Halıcıoğlu, L.C. Dülger, A.T.Bozdana,(2015) Servo Pres Tasarımı ve Dinamik Modeli: Uygulamalı Bir Örnek, Gaziantep Üniversitesi, Gaziantep, Uluslararası Katılımlı 17. Makina Teorisi Sempozyumu, İzmir, 14-17 Haziran 2015

[2]. Közkurt, Cemil & Fenercioğlu, Ahmet & Akar, Mehmet. (2012). Otomatik Depolama Sistemlerindeki Robotlar için Servo Motor Seçimi (In Turkish). Gaziosmanpaşa Bilimsel Araştırma Dergisi. 1. 97-105.

[3]. Yıldırım, F. & Babaoğlan, H. & Tosun, L.(2016). Endüstride Kullanılan Kereste Kesme Mekanizmasının Otomatik Kontrolü ve Prototipinin Oluşturulması(Lisans Tezi). Karabük Üniversitesi, Mühendislik Fakültesi, Karabük.

[4]. Lei, S. Y. (2013). Servo-Control System Design of Automatic Production Line Based on PLC and HMI. Applied Mechanics and Materials, 457–458, 1381–1385.

[5].Yılmaz, F. H.(2008) AC ve DC Servo Sistem Eğitim Setinin Geliştirilmesi(Yüksek Lisans Tezi).Selçuk Üniversitesi, Elektrik-Elektronik Mühendisliği Anabilim Dalı, Konya.

[6]. Chanchal Dey, Sunit Sen, Industrial Automation Technologies, University of Calcutta, India

[7]. Gerçek zamanlı Ethernet:Terminale kadar ultra yüksek hız. 2013, https://www.beckhoff.com.tw/tr/default.htm?ethercat/default.htm

[8]. Hu Xing , Huan Jia , Liu Yanqianga,(2011) Motion Control System using SERCOS over EtherCAT School of Mechanical Engineering & Automation Beihang University, Beijing, China

[9]. Ö.Aydoğdu, A.Çatkafa, SECA Mühendislik Otomasyon Ltd. Şti (2019) Bir Hidrolik Derin Çekme Pres Makinesinin PLC Tabanlı Bulanık Mantık Kontrolü Ve Endüstri 4.0 Uygulaması, Konya Teknik Üniversitesi, Mühendislik ve Doğa Bilimleri Fakültesi, Elektrik – Elektronik Mühendisliği Bölümü, Konya, TÜRKİYE, ISSN: 2667-8055

[10].Hakan Terzioğlu, Gökhan Yalçın , Mustafa Kısa,(2019) Servo Motorun SCADA ile Kontrolü, Department of Electrical and Energy, Konya Technical University, Konya,Turkey, European Journal of Science and Technology Special Issue, pp. 428-435, October 2019

SIMULATION OF VISION BASED LANDING FOR AN AUTONOMOUS TRUCK AND DRONE DELIVERY SYSTEM

Musa Nurullah Yazar

National Defense University Air Force Academy, Electronics Engineering Department, Istanbul, Turkey.
https://orcid.org/0000-0002-4453-662X
nyazar@hho.edu.tr

ABSTRACT

Recently, intensive research has focused on modeling delivery systems that include both trucks and drones to deliver goods to customers more efficiently. In this study, we simulate a vision-based landing on the back of a moving truck vehicle. The landing trajectory is generated by a developed algorithm and is followed by the tracking controller. We analyzed the control algorithm performance in the presence of bounded and unknown wind conditions that will be crucial for an efficient truck and drone delivery system. The simulation environment has been created on V-REP which is a robotic simulator that provides modularity, compatibility across platforms, and a large number of tools in less complexity. We implement the controller and processing architecture in Matlab/Simulink, the communication interface between both programs is achieved by means of the V-REP's API.

Keywords: *Robotic, simulation, autonomous delivery system, drone and truck, landing, vision*

REFERENCES

[1] Velasco, O., Valente, J., Alhama Blanco, P. J., & Abderrahim, M. (2020). An open simulation strategy for rapid control design in aerial and maritime drone teams: A comprehensive tutorial. *Drones*, *4*(3), 37.

[2] Crişan, G. C., & Nechita, E. (2019). On a cooperative truck-and-drone delivery system. *Procedia Computer Science*, *159*, 38-47.

[3] Liu, Y., Liu, Z., Shi, J., Wu, G., & Pedrycz, W. (2020). Two-Echelon Routing Problem for Parcel Delivery by Cooperated Truck and Drone. *IEEE Transactions on Systems, Man, and Cybernetics: Systems*.

[4] Das, D. N., Sewani, R., Wang, J., & Tiwari, M. K. (2020). Synchronized Truck and Drone Routing in Package Delivery Logistics. *IEEE Transactions on Intelligent Transportation Systems*.

[5] Marinelli, M., Caggiani, L., Ottomanelli, M., & Dell'Orco, M. (2017). En route truck–drone parcel delivery for optimal vehicle routing strategies. *IET Intelligent Transport Systems*, *12*(4), 253-261.

[6] Patruno, C., Nitti, M., Petitti, A., Stella, E., & D'Orazio, T. (2019). A vision-based approach for unmanned aerial vehicle landing. *Journal of Intelligent & Robotic Systems*, *95*(2), 645-664.

[7] Rabah, M., Rohan, A., Talha, M., Nam, K. H., & Kim, S. H. (2018). Autonomous vision-based target detection and safe landing for UAV. *International Journal of Control, Automation and Systems*, *16*(6), 3013-3025.

[8] Paris, A., Lopez, B. T., & How, J. P. (2020, May). Dynamic landing of an autonomous quadrotor on a moving platform in turbulent wind conditions. In *2020 IEEE International Conference on Robotics and Automation (ICRA)* (pp. 9577-9583). IEEE.

FAST-CHARGING HYBRID POWER SUPPLY FOR SCOOTERS

O. Yargi[1*]

[1]*Yildiz Technical University, Physics Department, Istanbul, Turkey.*
.
oyargi@yildiz.edu.tr

ABSTRACT

This study presents a production of supercapacitors that can be used in electiral scooters which consist of battery /supercapacitor bank which is called hybride energy storage system(HESS) to obtain high performance energy. The approximate charging time of lithium-ion technology batteries of electric scooters varies between 6-8 hours. It is predicted that this time will be shortened in supercapacitor/battery hybrid power systems, thanks to the very fast charging feature of the supercapacitors. The battery of a scooter at the moment of take-off can drop to 28V with the effect of internal impedance. In this case, Segway Max G30, which has 610W starting power, needs 22A levels of current to feed the scooter motor. These levels, especially at low voltage levels, both damage the battery and cannot be met except for a short time (a few seconds). In this work, a supercapacitor was devoleped where one side was produced by Nickel-Zinc and other side was produced by dealloying of the Nickel/Zinc electrodes with the organic cellulose as a seperator in the presence of 6M pottasium Hydroxide (KOH). Results showed that dealloying process in 1M potassium chloride (KCL) created much higher performance than that of alloyed supercapacitors.

Keywords: *Supercapacitors, Hybride energy, Electrical Scooters.*

REFERENCES

[1] https://letspalm.com/
[2] İ Yılmaz, A Gelir, O Yargi, U Sahinturk, OK Ozdemir, Electrodeposition of zinc and reduced graphene oxide on porous nickel electrodes for high performance supercapacitors.
[3] Lu Han, Hailong Huang, Junfeng Li, Zhongli Yang, Xinlu Zhang, Dafeng Zhang, Xinjuan Liu, Min Xu and Likun Pan N, Novel zinc–iodine hybrid supercapacitors with a redox iodide ion electrolyte and B, N dual-doped carbon electrode exhibit boosted energy density.

USING BASIC-SHAPED TINY ROBOTS FOR BIOMEDICAL APPLICATIONS: A MATHEMATICAL APPROACH

Musa Nurullah Yazar[1,2], Samire Yazar[3,4*]

[1] National Defence University, Air Force Academy, Electronics Engineering Department, Istanbul, Turkey.
[2] https://orcid.org/0000-0002-4453-662X
[3] Ordu University, Department of Mathematics, Ordu, Turkey.
[4] https://orcid.org/0000-0002-1125-3631

*samirebalta@odu.edu.tr

ABSTRACT

Tiny robots to deliver medicine or to transport of drugs in the vascular system or lung airways have recently been very popular in both robotics and mathematical modelling. The work presented in this paper involves mathematical methods and robot simulation environment to develop a model for these kinds of medical problems by investigating rigid body motion as well as the surrounding fluid properties within the vessel. We first establish the simulation environment using V-REP "CoppelliaSim" (Virtual Robot Experimentation Platform) which is multi-objective and ideal for multi-robot applications. Then Matlab is used for the numerical integration of the coupled system of partial and ordinary differential equations to analyse the fluid flow behavior and the hydrodynamic forces acting on the robot body for the purpose of modelling the related problem. Comparisons between the analytical predictions and the numerical results appear to be quite encouraging.

Keywords: *Tiny Robots, Drug Delivery, Vessels, Mathematical Modelling, Fluid Flow.*

REFERENCES

[1] Li, H., Tan, J., & Zhang, M. (2008). Dynamics modeling and analysis of a swimming microrobot for controlled drug delivery. *IEEE Transactions on Automation Science and Engineering*, *6*(2),220-227.
[2] Nistor, M. T., & Rusu, A. G. (2019). Nanorobots with Applications in Medicine. In *Polymeric Nanomaterials in Nanotherapeutics* (pp. 123-149). Elsevier.
[3] Peyer, K. E., Zhang, L., & Nelson, B. J. (2013). Bio-inspired magnetic swimming microrobots for biomedical applications. *Nanoscale*, *5*(4), 1259-1272.
[4] Shang, Z. (2013). Numerical investigations of supercavitation around blunt bodies of submarine shape. *Applied Mathematical Modelling*, *37*(20-21), 8836-8845.
[5] Smith, F. T., & Ellis, A. S. (2010). On interaction between falling bodies and the surrounding fluid. *Mathematika*, *56*(1), 140-168.
[6] Smith, F. T. (2017). Free motion of a body in a boundary layer or channel flow. *Journal of Fluid Mechanics*, *813*, 279-300.

High Efficiency Luminescent Solar Concentrator using superposing of Graphene Quantum Dots

L. Asadi[1], M. Dolatyari[2], A. Rostami[1, 2], S. Matloub[3] and R. Yadipour[4]

Abstract

In this paper, a novel method is proposed and evaluated theoretically to enhance the efficiency of luminescent solar concentrator (LSC). For implementation of the idea, superposing quantum dots are used. LSCs doped with graphene quantum dots (GQDs) and Nd-doped GQDs show high efficiency up to 9%. The Monte Carlo ray tracing is employed to evaluate the proposal structure. We anticipate our high-efficiency LSC prototype device based on GQDs will shed light on near future research of LSCs and transparent solar harvesting devices.

Keywords- Monte Carlo, superimposed quantum dots,

Underhood Thermal Analysis of a Heavy Commercial Vehicle with OpenFOAM

Çağatay Emre Ayhan[1], Altuğ Melik Başol[1], Bekir Aydın[2], Yasin Hacısalihoğlu[2], Cenk Dinç[2]

1. Mechanical Engineering Department
   Ozyegin University
   emre.ayhan@ozu.edu.tr
   altug.basol@ozyegin.edu.tr

2. Ford Otosan
   yhacisal@ford.com.tr
   baydin2@ford.com.tr
   cdinc@ford.com.tr

Underhood thermal design of the heavy commercial vehicles have a large influence on the performance and reliability of the vehicle. In this study a computational thermal model of a heavy commercial vehicle has been developed using the open source CFD package OpenFOAM. The model includes detailed underhood geometry and heat rejecting components. The turbocharger heat shield temperatures predicted with the computational model are in agreement with the measurements showing error in the order of 2%. Running on 56 CPU cores the model converges in 38h. The weak scalability of the solver has been tested by running the model on 28 CPU cores. Except the thermal radiation model, the solver shows almost an ideal scalability. The surface-to-surface radiation model in OpenFOAM is currently not parallelized which seriously limits its use in underhood thermal analysis. The radiation model is computationally feasible only for scenarios where the number of surface elements is less than 20k.

QUALITY MANAGEMENT IN AUTOMOTIVE INDUSTRY AND KEY STUDY

FATIH MEHMET NURHAT[1],

[1] *Istanbul Medeniyet University, Engineering Management Department Istanbul, Turkey.*

fnurhat@gmail.com

ABSTRACT

Nowadays quality is the most important concept in automotive industries. Especially automotive industries need quality about in both visual and durability. But there are needed a quality management standard for in a implementing every production phase. For long years used and known by everybody ISO 9001 quality management standard is a source of inspiration about that in automotive industries. Due to rise of automotive industries in global level in for years, automotive industries were need more comprehensive quality Standard. Because of that, established a quality standard as called IATF 16494. Quality management standard supports to company about evaluating opportunities, preventing threatening and planning cost. So every company should have a quality management Standard. Implementing this system may seem exhausting but in long termination established and applied system useful to companies for both about cost and quality was proved. In this study different quality management strategies were explained in automotive industry in detail.

OPTIMIZATION OF IMPACT MITIGATION USING ORIGAMI BASED METAMATERIALS

K. Kocak[1*], J. Yang[2]

[1] *Istanbul Medeniyet University, Department of Mechanical Engineering, Istanbul, Turkey.*
[2] *University of Washington Seattle, Department of Aeronautics and Astronautics, Seattle, WA, USA.*
*kamil.kocak@medeniyet.edu.tr

ABSTRACT

Origami based metamaterials provide unique wave dynamic mechanisms, which can be used to enhance the mechanical properties of the engineered structures. Triangulated Cylindrical Origami (TCO) is a volumetric origami structure, in which the folding process develops coupling dynamics of axial and rotational motions. One of the unique properties of TCOs is their strain-softening behavior, and it is possible to design TCO cells so that this behavior can generate rarefaction solitary waves. It is known that under impact excitation, initial compressive strain waves are overtaken by a rarefaction solitary wave, which would also decrease the maximum amplitude of the compressional force in the system. This study aims to optimize the design parameters of a TCO system for impact mitigation as well as to investigate the underlying mechanisms resulting in its unique properties using analytical modeling and numerical analysis.

Keywords: ORIGAMI BASED METAMATERIALS, TRIANGULATED CYLINDRICAL ORIGAMI, STRAIN SOFTENING, WAVE DYNAMICS, RAREFACTION SOLITARY WAVES, IMPACT MITIGATION.

Enhancement in Thermal Energy Storage using Encapsulated Phase Change Material

Muhammad Azhar Hussain[1*], Aneela Wakeel[2], Hafiz Muhammad Ali[1]

[1*,1] *University of Engineering and Technology, Mechanical Engineering Department, 47050 Taxila, Pakistan.*
[2] *University of Engineering and Technology, Metallurgy Engineering Department, 47050 Taxila, Pakistan.*
*muhammadazharhussain27@gmail.com

ABSTRACT

Energy is the basic need of the world. The demand of energy of the world can be fulfilled by using the fossil fuel resources but the main problem is that these resources rapidly used and one-day it will be diminished. To fulfill energy demand, renewable energy assets like solar energy has the supreme rule because it is easily available on earth. For energy storage purposes phase change material has the vital role. It can store surplus amount of energy by financing less amount and small variation in temperature. The main theme of this research is to increase energy retention by the use of encapsulated phase change material. The amalgam of $NaNo_3$-KNo_3 is used as PCM in cylindrical body capsules which is constructed of stainless steel. The experimentation is done at various temperatures temperature (220℃, 235℃, 250℃, 265℃, and 280℃) and different mass flow rates (4 liter/min, 3.33 liter/min and 2.67 liter/min). To check the energy storage and the emancipate capacity of PCM in a certain time experiment is done at both charging and discharging cycles. The overall analysis of the system can also be done on these two cycles. Finally, the results of experimentation are compared with mathematical model already developed.

Keywords: *Phase change material, encapsulated phase change material, Thermal energy storage.*

DEVELOPMENT OF AUTOMATED GROUND VEHICLE FOR MEDICAL AND COMMERCIAL APPLICATION

Dr. K. Sivasakthi balan [1], Mr. Muthuvel [2], Mr. R. Vijai [3] , Mr. Harishbabu L [4] & Mr. Darshan NK [5]

[1] Professor [2-4] Assistant Professor [5] Research Engineer, Department of Mechanical Engineering, Sri Sairam college of engineering, Bangalore, Karnataka, India.

The aim of this paper is to design and fabrication of Autonomous Ground Vehicle (AGV) for the medical and Commercial application. The automation of transportation in the production, trade and service sectors is a key point in optimization of logistics. Industries are trying to reduce the labour cost and processing time which is taken by human. Autonomous ground vehicle provides several benefits to full fill this task. This proposal to work will be helpful for handling the material efficiently by carrying the material automictically. The vehicle that can be moved autonomously while automatically detecting and avoiding obstacles and reads the directions from QR codes to reach its destination, not only in industries this idea can be extended to fit in many sectors such as schooling to carry the documents, hospitals for carrying medical equipment's and medicines, malls hotels, banks, offices and many more. This system includes a battery-operated remote sensing carrier on which the goods is provided, specific path over which it moves, sensors for sensing the abstractions on the path. The vehicle can lift up to 150 kg payload, cost effective, 3 to 4 Hours endurance, ground clearance is 15 cm and can operate in remote or autonomous mode depends on the user requirements.

EFFECTS OF THE COMBUSTION CHAMBER GEOMETRY ON COMBUSTION AND EMISSION OF A LIGHT-DUTY CI ENGINE

R. Sener[1*], M.Z. Gul[2]

[1] *Batman University, Automotive Engineering Department, Batman, Turkey.*
[2] *Marmara University, Mechanical Engineering Department, Istanbul, Turkey.*
*ramazan.sener@batman.edu.tr

ABSTRACT

Compression-ignition engine is widely used due to its thermal efficiency, reliability, and fuel economy, while the engine emissions are harmful to the environment and human health. Therefore, standards (EPA, Tier, NRE-v / c standards, etc.) limit the exhaust emissions of engines around the world. The most successful method of reduction of exhaust emissions is to optimize the combustion chamber and fluid motion inside the engine. In this study, the CFD method was used to analyze fluid motion, spray, combustion process, and exhaust emissions in a CI engine. A new type of swirl piston bowl is used in the engine. The results are compared to the baseline engine piston bowl on combustion and emission. The results show that piston bowl shape has a critical impact on engine performance and emissions. The multi-swirl piston bowl (MSB) and double-swirl piston bowl (DSB) design contribute to reducing emissions and improving the combustion process, as it increases in-cylinder swirl and turbulence. DSB and MSB improve the combustion process but also increase NO_X emissions due to an increase in-cylinder temperature. On the other hand, NO_X emissions can also be reduced if the injection parameters of the engine are optimized to provide the same power as the swirl piston bowls.

Keywords: Combustion, bowl, diesel engine, emission.

NUMERICAL INVESTIGATION OF PPCI STRATEGY FOR HIGH-EFFICIENCY COMBUSTION

R. Sener[1*], M. Yılmaz[2]
[1] *Batman University, Automotive Engineering Department, Batman, Turkey.*
[2] *Marmara University, Mechanical Engineering Department, Istanbul, Turkey.*
*ramazan.sener@batman.edu.tr

ABSTRACT

Homogeneous charge compression ignition (HCCI) is a combustion concept with significant potential due to low NO_X, soot emissions, and high efficiency. Early direct injection during the compression process is an option within the HCCI concept. However, in this strategy, the spray angle should be applied narrower to prevent the fuel from impinging the cylinder wall. In this study, it was aimed to constitute an HCCI concept with a pre-, main- and post-injection strategy and injector with an 80-degree narrow spray angle. Two different injection strategies were proposed in order to minimize emission. These were compared with the conventional injection strategy under the same conditions. The partial premixed (PPCI) combustion process was investigated in terms of combustion efficiency, fuel consumption, and emissions. The engine emits significantly low NO_X emissions with the PPCI combustion strategy.

Keywords: HCCI, PPCI, Combustion, emission reduction.

Modeling and design of an intelligent controller

Soumia KEDAIFA & Abdelouahab HASSAM

Department of Electronics, Laboratory of Intelligent Systems University Ferhat Abbes
Sétif-1 19000, Sétif, Algeria.
E-mail: soumia.kedaifa@univ-setif.dz
abdelhassam@univ-setif.dz

Abstract: This paper presents a collaborative study comparison of two intelligent controllers for trajectory tracking and obstacle avoidance in an autonomous vehicle in order to guide autonomous vehicles in external environments. A Part of this article focuses on the performance of two path tracking controllers which are implemented using two different approaches, the fuzzy logic and the neuro-fuzzy control. The first provides a good tracking whereas the second one has a great potential for navigation issue. We use those techniques of artificial intelligence to guarantee autonomy and intelligence for the path tracking behavior. Matlab/Simulink simulation show satisfactory results that helped to equip the robot up to a certain intelligence degree. However, there are still some improvements to bring to increase the performance of both systems.

Keywords: *Trajectory tracking, Fuzzy control, neuro-fuzzy control, Nonlinear control system.*

INVESTIGATION OF BIOGAS COMBUSTION IN SI ENGINE

Y. KARAGÖZ[1,*]

[1] Istanbul Medeniyet University, Mechanical Engineering Department, Istanbul, Turkey.
[1,*]yasin.karagoz@medeniyet.edu.trCO[2]

ABSTRACT

Gasoline fuel and biogas fuel in a single cylindired, spark ignition type, naturally aspirated, four stroke engine has been compared in terms of performance and emission by using the one dimensional simulation program in the study carried out. The biogas fuel consist of 20% CO_2 and 80%CH_4 gas composition. According to the results obtained, torque rating reduced as a little amount, CO and THC emissions increased because of worsening of combustion. On the other hand, NO_x emissions decreased because of increasing the CO_2 ratio in biogas usage in the combustion chamber and decreasing O_2 accessiblity.

Keywords: *Biogas, SI engine, alternative fuel, emissions*

INTRODUCTION

In the recent years, both the harsher emission regulations and environmental concerns have been led researchers to alternative vehicle technologies. Studies has been increased on hybrid and elecytical drive systems. Hovewer, both battery technologies still need time and the cost of batteries have led researchers to alternative technologies. It has been a great importance to study on engines that run with alternative fuels during the transition process to hybrid and electrical vehicle technologies in this context. Using alternative fuels such as hydrogen, biogas, biodiesel, natural gas are a great importance in conventional internal combustion engine. Some researchers used the alternative gas fuels in internal combustion engine as mentioned below.

Rosadi and Aleiferis [1] in the study carried out, they investigated thermodynamically combustion in the port injection type engine and direct injection engine with different fuels such as hydrogen and gasoline at 100 rpm engine speed with 1 to 2 degrees crank angle tendency. HCCI studies were carried out with different fuels, direct spraying or port spraying, at different air excess coefficients.

Fırat et al.[2] in the study carried out, they investigated the effect of engine performance by addition hydrogen as additional fuel in different ratios (2%, 4% and 6%) in pure diesel fuel by AVL-Fire program. According to obtained results, they have decided that combustion time and CO emission decreases , combustion speed increased with the hydrogen addition.

Mariani et al.[3] in the study carried out, they modelled one cylindired,controlled auto ignition engine which works with only methane fuels and methane fuels that enriches with 10% and 20% hydrogen and modelled with Chemkin, and they analyzed the indicated mean effective pressure,thermal efficiency and emission data. They observed that by using hydrogen added biogas fuel, indicated mean pressure stays constant and NOx emissions reduce.

Sharma et al.[4] in the study carried out, they observed that formation of NO_x,CO and unburnt hydrocarbons decrease with the addition of hydrogen, also consumption of hydrocarbon fuels decrease with the addition of hydrogen, lean operation conditions develop, therefore they concluded that hydrogen can be reform by electrolysis of water or hydrocarbon fuels for the application of this method.

Santaso et al.[5] in the study carried out, they investigated the effects on thermal efficiency and peak cylinder pressure by runnig of hydrogen with diesel engine and low loads. According to obtained results, they concluded that peak cylinder pressure decrease by adding hydrogen in different rations in the 200 rpm speed engine and Nm load conditions.

In the performed study, due to lack of sufficient studies in the literature that regarding the use of biogas fueled engines in conventional spark ignition type engines, performance and emission data of only gasoline fuel and biogas (20% CO_2 + 80%CH_4) fuel in a single cylinder, naturally aspirated, air cooled, spark ignition type engine at a fixed engine speed of 2900 rpm have analyzed and have modelled with the help of AVL Boost one dimensional combustion analyze program.

Engine Specifications

Analyses have carried out on a single cylinder, naturally aspirated, air cooled, 4 stroked, spark ignition type engine. Engine specifications are given in Table-1.

Table – 1 Test Engine Specifications

Engine brand	Honda
Number of cylinder	1
Cylinder volume (cc)	270
Bore (mm)	77

Stroke (mm)	58
Max power (kW)	6.3 kW @ 3600 rpm
Cooling system	Air
Aspiration system	Naturally aspiration

Theoretical Engine Model

Single cylinder, one dimensional, quassi-stattic spark ignition type engine has set up as an engine model by AVL Boost software. Only gasoline and only biogas (20% CO_2 + 80%CH_4) fuels have analyzed with developed model at 2900 rpm engine speed. Model has applied from intake port of engine with biogas injection or gasoline injection.On the other hand, measured ignition advance value by stroboscope and measured valve advance value by comparator have added to model.

Engine model schematic view is given in Figure-1.

Figure-1 Schematic view of engine model

Design of Experiments

Two different conditions have focused during studies. Study conditions have carried out with only gasoline fuel and only biogas fuel (20% CO_2 + 80%CH_4) at 2900 rpm fixed speed. Excess air coefficient in engine has tried to keep same value and ignition advance has not changed. Summary of studies are given in Table-2.

Table-2 Summary of studies

	Engine Speed (rpm)	Brake Engine Torque (Nm)
Gasoline	2900	23
Biogas	2900	19

RESULTS AND DISCUSSION

Analyses have carried out on a single cylinder, naturally aspirated, air cooled, 4 stroked, spark ignition type engine and only gasoline fuel and biogas fuel (20% CO_2 + 80%CH_4) have analyzed by AVL Boost software program at 0.1 crank angle tendency. Engine performance and emission values(CO, HC and NOx)have compared.

Brake Engine Torque

Comparison of brake engine torque data are given in Figure 2. According to results, it has concluded that brake engine torque value decreased from 23 Nm to 19 Nm at 2900 rpm fixed engine speed. The reason of these results are; fuel with an volumetrically unsufficient heating value can not send into ,because of the keep constant of the excess air coeffieicient and the biogas fuel consist specific amount CO_2 gas.
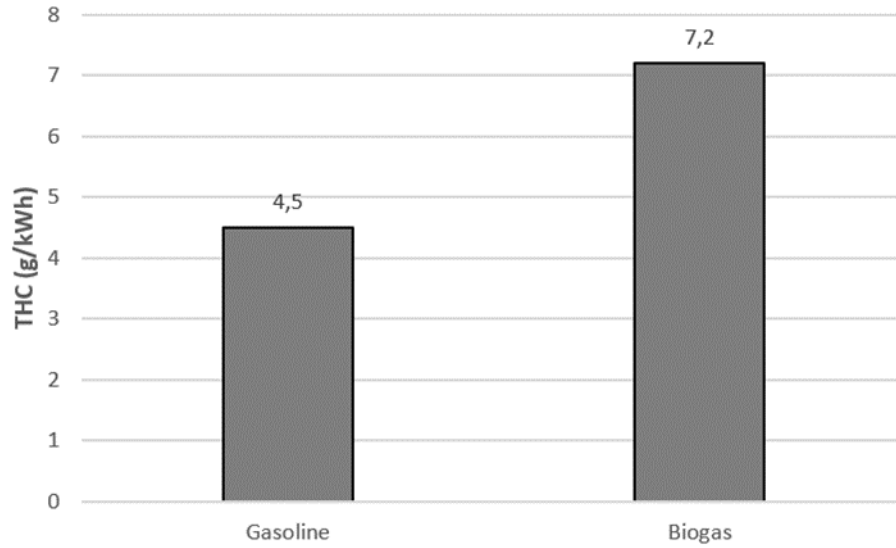
Figure-2 The comparison of brake engine torque

CO Emissions

CO emission datas in performed study are given in Figure-3. According to obtained results, CO emission value increased from 205 g/kWh to 275 g/kWh with the carried out biogas fuel analyses. In the obtaining results, CO emissions increased as a result of these factors which are; biogas consist CO_2 gas and decrease of in-cylinder pressure and decrease achievability to O_2 gas.
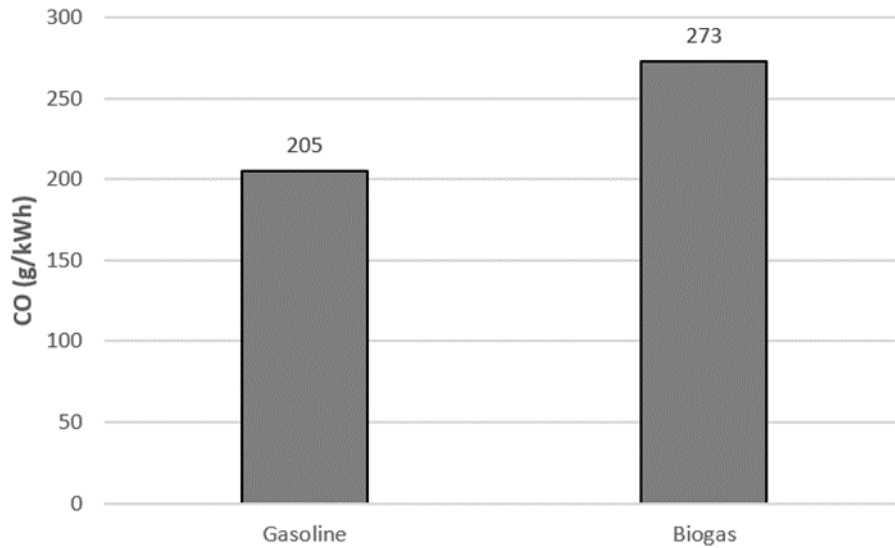
Figure-3 The comparison of CO emission values

THC Emissions

THC emission datas in performed study are given in Figure-4. According to obtained results, THC emissions value increased from 4,5 g/kWh to 7,2 g/kWh with the carried out biogas fuel analyses. During the analyses, considering the decreasing the air amount that taken in-cylinder because of biogas consist of CO_2 and being a gas fuel, it has concluded that THC emission decreased with the worsenin of combustion. On the other hand, it has expected to increment of THC with the consideration of quenching distance of methane.

Figure-4 The comparison of THC emission values

NO$_X$ Emissions

NO$_x$ emission datas in performed study are given in Figure-5. According to obtained results, NO$_x$ emissions value decreased from 0,8 g/kWh to 0,4 g/kWh with the using of biogas fuel. According to these analyse ;decreasing of NO$_x$ emission can be commented with these factors which are; diluting the cylinder with the biogas that contains CO_2, restriction of O_2 availability and decreasing of in-cylinder pressure thus decreasing of temperature values. In the obtained results, when both the increase in CO and THC emissions with the use of biogas and the decrease in combustion efficiency have evaluated together, it has concluded that NO$_x$ emissions reduced as expected.
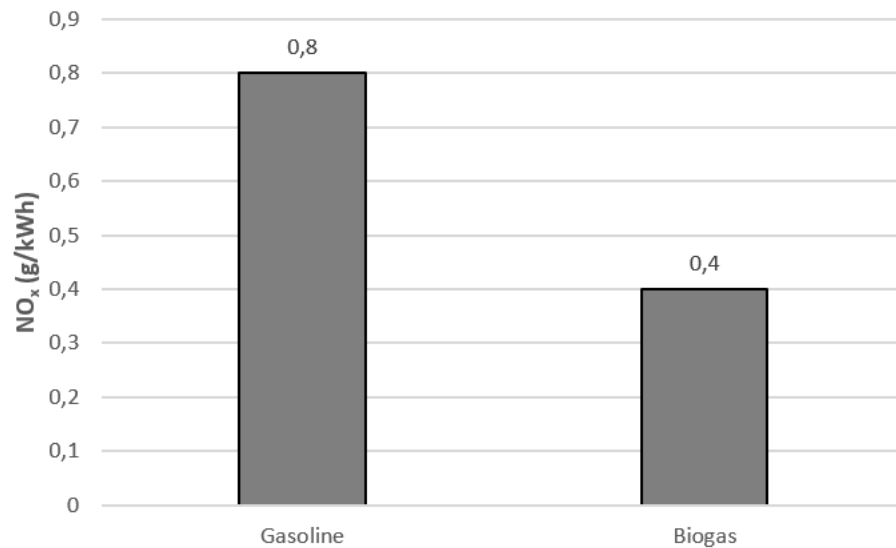
Figure-5 The comparison of NOx emission values

CONCLUSION

In the performed study, with the help of AVL Boost software program, on a single cylinder, naturally aspirated, air cooled, 4 stroked, spark ignition type engine and only gasoline fuel and biogas fuel (20% CO2 + 80%CH4) engine torque, have been compared in terms of CO, HC and NOx emission values. Obtained results have summarized below.

- Brake engine torque value decreased from 23 Nm to 19 Nm at 2900 rpm fixed engine speed according to biogas fueled analyse result.
- CO emission value increased from 205 g/kWh to 275 g/kWh at 2900 rpm fixed engine speed according to biogas fueled analyse result.
- THC emissions value increased from 4,5 g/kWh to 7,2 g/kWh at 2900 rpm fixed engine speed

according to biogas fueled analyse result.

● NO_x emissions value decreased from 0,8 g/kWh to 0,4 g/kWh at 2900 rpm fixed engine speed according to biogas fueled analyse result.

REFERENCES

[1] M.F. Rosati and P.G. Aleiferis. Hydrogen SI and HCCI Combustion in a Direct-Injection Optical Engine. SAE International. Paper No: 2009-01-1921

[2] Müjdat FIRAT, Mutlu OKCU, Yasin VAROL. Dizel Motorlarda Yakıta Hidrojen Katkısının Yanma, Performans ve Emisyonlar Üzerine Etkilerinin İncelenmesi. Fırat Üniv. Müh. Bil. Dergisi. 29(1), 101-108, 2017

[3] Antonio Mariani, Andrea Unich, Mario Minale. Combustion of Hydrogen Enriched Methane and Biogases Containing Hydrogen in a Controlled Auto-Ignition Engine. Applied Sciences. 2018, 8, 2667; doi:10.3390/app8122667

[4] Suryakant Sharma, Deepak Bhardwaj, Vinay Kumar. EFFECT ON PERFORMANCE OF ENGINE BY INJECTING HYDROGEN. IJMERR. Vol. 2, No. 3, July 2013

[5] W. B. Santosoa, R. A. Bakar, A. Nur. Combustion characteristics of diesel-hydrogen dual fuel engine at low load. Energy Procedia 32 (2013) 3 – 10

DYNAMIC RESPONSE CHARACTERISTICS OF SPUR GEARS IN TORQUE SPLIT APPLICATION

S. Civan[1*], C. Demir[1]

[1] *Yildiz Technical University, Mechanical Engineering Department, Istanbul, Turkey.*
*suleymancivan@gmail.com.tr

ABSTRACT

Gear vibration is an important consideration in drive-train systems due to noise and durability problems. Under dynamic conditions, gear systems produce much higher gear mesh forces than static forces transmitted. These high frequency dynamic forces must be supported by the bearings and are eventually transmitted to the housing to act as the main excitations for gear related noise. Furthermore, alternating forces induced by the vibration reduce fatigue life of the driveline components. Therefore, a better understanding of the gear system dynamics is vital in order to design more silent and durable transmission.

The mathematical model of nonlinear dynamics of a multi mesh spur gear train is studied. Nonlinear dynamic equations are established by using Lagrange method with 2 degree of freedom in torsional direction. Dynamic model includes gear backlash, time variant gear mesh stiffness, and static unloaded transmission error. The equation of motion is solved by time integration Runge Kutta method in Simulink/MATLAB. The purpose of this analysis is to estimate relative root mean square of dynamic transmission error in the operation range and specify mesh natural frequencies.

Keywords: Transmission Dynamics, Gear Dynamics, Jump Phenomenon, Gear Vibration, Dynamic Analysis of Gears.

INTRODUCTION

Gearbox is the main basic element of powertrain systems in aerospace, automotive, railway applications in terms of obtaining required speed and torque ratio from input to output. There are some topics like noise-vibration, part life time estimation, permissible maximum torque, speed and efficiency still under study to optimize best design.

Deflection can be occurred when load is exerted on tooth surface. Especially high speed and torque applications can cause torsional vibrations due to change in mesh stiffness. Bending, shear, axial compression, Hertz strength and gear foundation flexibility are the elements of gear stiffness parameter.

There should be some backlash not to be stuck during the system motion. If the torque in the system is so high, tooth contact is never lost in the line of action. If the torque is not high, tooth contact can be lost and tooth can hit to succeeding tooth or not to contact with preceding or succeeding tooth. By gear dynamic modelling, nonlinear displacement factor can be obtained. Nonlinear dynamic factor comprises of gear stiffness and backlash change.

Dynamic modelling consists obtaining of system response for the effect like force, torque. Mass and inertia is the kinetic energy and stiffness is the potential energy storage parameters. Oil film, hysteresis due to material structure and friction effects can be described as damping parameters. In addition, static transmission error should be included when calculating the dynamic transmission error. System dynamic model is established in Simulink/MATLAB program. Compound torsional – bending frequency response is obtained for variable stiffness values.

DYNAMIC MODELLING METHODS OF SPUR GEAR

There are four methods in the literature as given below.

Linear time invariant: Mesh stiffness is assumed as time invariant and constant value. Backlash is also not considered for the model.

Linear time variant: Mesh stiffness variation is based on gear roll angle rotation. There is no backlash theoretically in this modelling type.

Nonlinear time invariant: Mesh stiffness is taken as constant average value. Backlash is introduced to model.

Nonlinear time variant: Mesh stiffness variation is based on gear roll angle rotation. Backlash cause nonlinear motion especially resonance region and its sub harmonics. [10]

Table 1. Modelling Methods
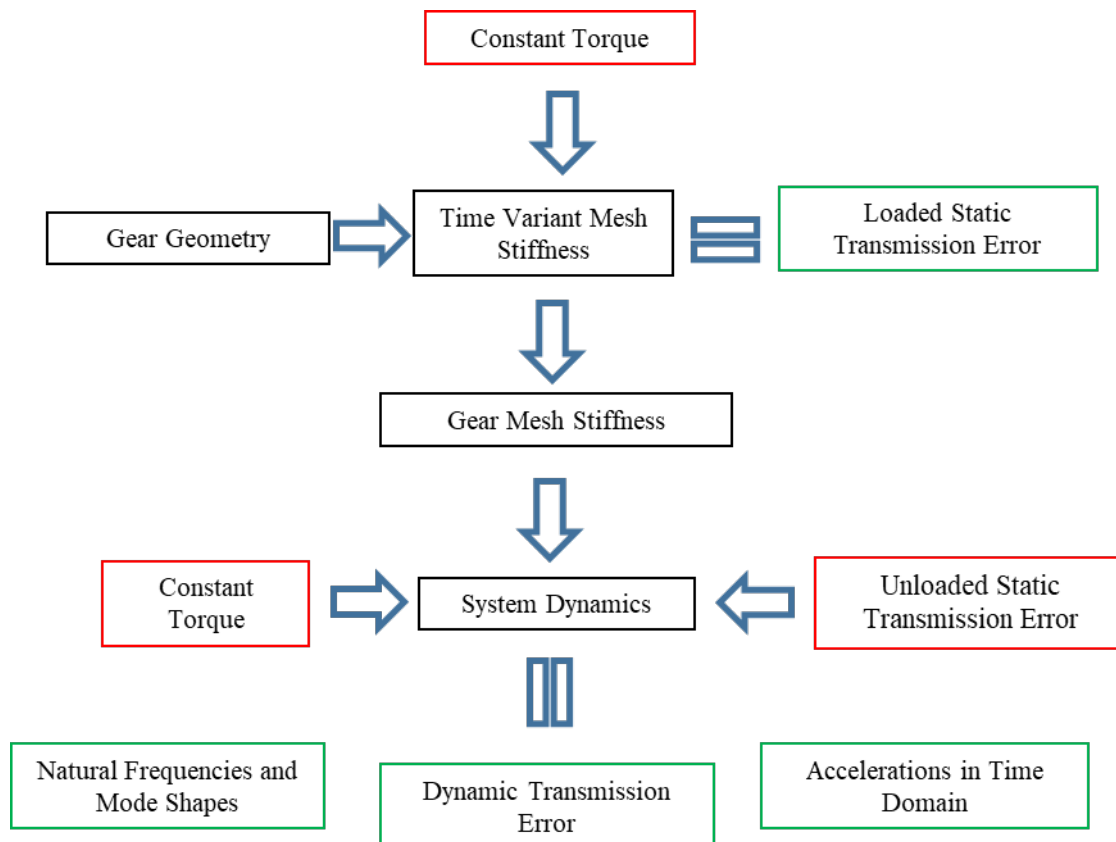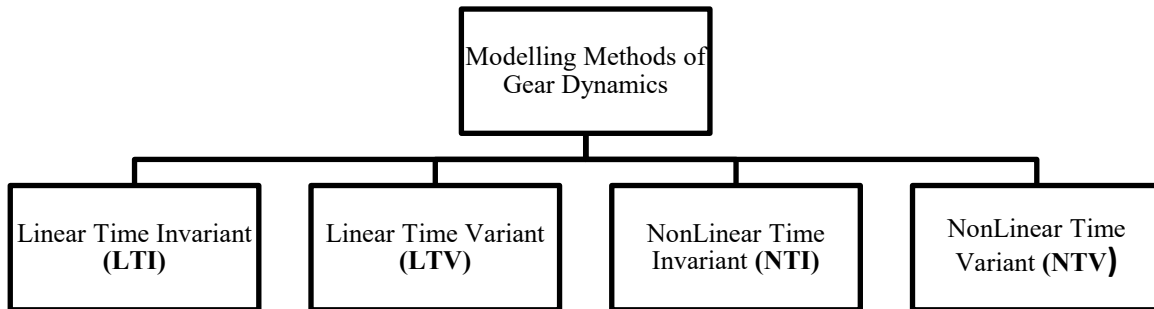
Figure 1. Flow chart of the simulation for gear dynamics of spur gears

Mesh stıffness PARAMETERS

The system stiffness parameters can be categorized in two section: elastic deformation factors and static deformations.

Elastic Deformation Parameters

- There are some deformation factors in gear pairs can be given as axial compression, bending, shear, foundation compliance and Hertz deformation.
- Material removal from web and holes could increase deformation in gear web
- Shaft and gear bore compliance can be neglected if these two part assembled rigidly.
- Bearing stiffness also affect system deflection. Therefore, bearing effect should be considered in translational motion.
- Housing stiffness can be obtained by test rig or finite element analysis.
- Housing foundation represents the displacement on the housing relative to ground.

Static Deformation Parameters:

Static deformation factors can be given as bearing clearances, thermal expansions, interference fit, oil film thickness at plain bearing, etc. [11]

Gear Train Geometry

Firstly, number of teeth, module, face width and pressure angle should be specified based on load and speed boundary conditions in gear system conceptual design. Then amount of profile shift can be calculated according to center distance. Generally, the purpose of profile shift is to facilitate measuring shaft coordinates on housing to keep integer values.
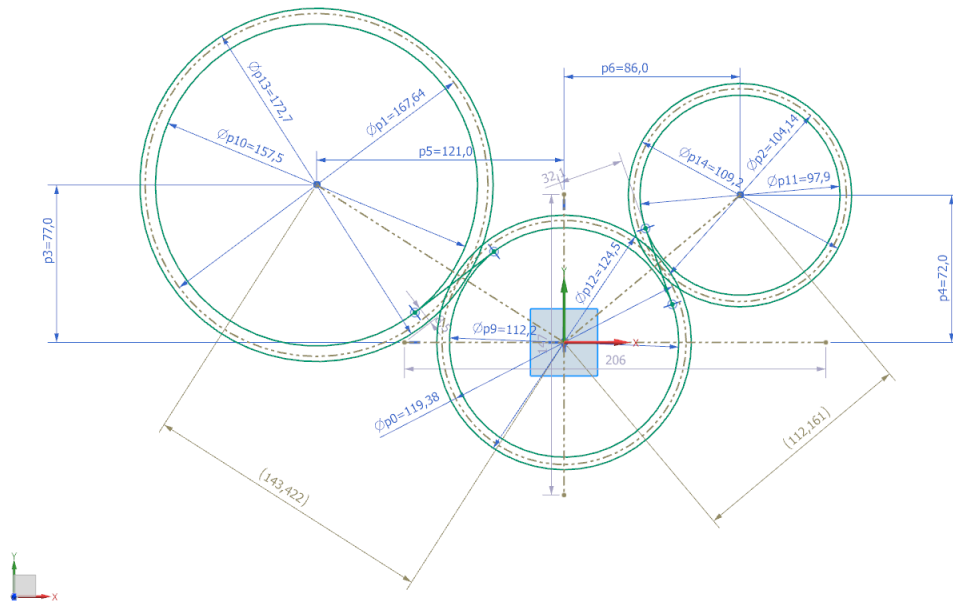
Figure 2. Defining gear shaft locations based on design inputs
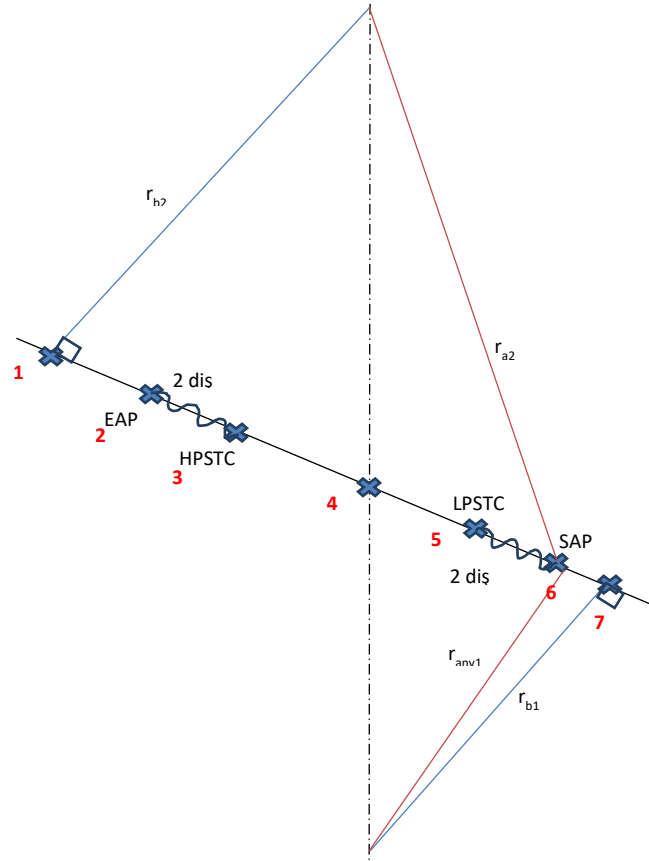
Figure 3. Determining LPSTC and HPSTC points from gear pair geometry [2]

Instantaneous pressure angle for each roll angle increment:

$$\alpha_{any} = acos\left(\frac{r_b}{r_{any}}\right) = atan\left(\sqrt{\left(\frac{r_{any}}{r_b}\right)^2 - 1}\right) \tag{1}$$

Single and double tooth contact length is calculated from gear geometry.

$$\text{Line of action} = |17| = \frac{r_{b1} + r_{b2}}{2}\tan\alpha_w \tag{2}$$

$$\text{Center distance (a)} = m * \frac{(z_1 + z_2)}{2} \tag{3}$$

$$\text{Working pressure angle } (\alpha_w) = \frac{acos(r_{b1} + r_{b2})}{\text{Working center distance (profile shifted) } a_w} \tag{4}$$

$$r_{EAP1} \rightarrow r_{SAP1} = \sqrt{r_{b1}^2 + \left(|17| - \sin\alpha_{tip2} * r_{tip2}\right)^2} \tag{5}$$

$$r_{EAP2} \rightarrow r_{SAP2} = \sqrt{r_{b2}^2 + \left(|17| - \sin\alpha_{tip1} * r_{tip1}\right)^2} \tag{6}$$

Total profile shift value of gear pair

$$x_1 + x_2 = \frac{a_w(\text{inv } \alpha_w - \text{inv } \alpha)}{m * \tan \alpha} \tag{7}$$

$$|67| = |17| - r_{tip2} * \sin\left(\frac{acos\ r_{b2}}{r_{tip2}}\right) \tag{8}$$

$$|36| = |25| = P_B = m * \pi * \cos \alpha \tag{9}$$

$$\text{Contact Length} = |26| = r_{tip1} * \sin \alpha_{tip} - |67| \tag{10}$$

$$|27| = r_{tip1} * \sin \alpha_{tip1} \tag{11}$$

$$|56| = |26| - |25| \tag{12}$$

$$|12| = |17| - |27| \tag{13}$$

$$|23| = |26| - |25| \tag{14}$$

$$|16| = r_{tip2} * \sin \alpha_{tip2} \tag{15}$$

$$|15| = |16| - |56| \tag{16}$$

Theoretical contact ratio

$$CR = \frac{\text{Contact Length}}{\text{Base Pitch } P_B} = \frac{|26|}{|25|} \tag{17}$$

Start of active profile radius of pinion:

$$r_{SAP1} = \sqrt{|67|^2 + r_{b1}^2} \tag{18}$$

End of active profile radius of pinion:

$$r_{EAP1} = r_{tip1} \tag{19}$$

Start of active profile radius of gear:

$$r_{SAP2} = r_{b2} * \cos \alpha_{SAP2} \tag{20}$$

End of active profile radius of gear:

$$r_{EAP2} = r_{tip2} \tag{21}$$

Highest point of single tooth contact of pinion radius:

$$r_{HPSTC1} = \sqrt{r_{b1}^2 + (|36| + |67|)^2} \tag{22}$$

Lowest point of single tooth contact of pinion radius:

$$r_{LPSTC1} = \sqrt{r_{b1}^2 + (|56| + |67|)^2} \tag{23}$$

Highest point of single tooth contact of gear radius:

$$r_{HPSTC2} = \sqrt{r_{b2}^2 + (|15|)^2} \tag{24}$$

Lowest point of single tooth contact of gear radius:

$$r_{LPSTC2} = \sqrt{r_{b2}^2 + (|12| + |23|)^2} \tag{25}$$

These gear geometry parameters is defined gear system design with accordance to Ref [2].

Bending, shear and axial compression deformations:

Bending, shear and axial compression is calculated by using unit load (F=1 N) and unit face width length (fw=1 mm). Hereby, these deformations are independent from load and only depend on gear geometry

Pitch:

$$p = m\,\pi \tag{26}$$

Reference diameter:

$$D_p = m\,z \tag{27}$$

Base diameter:

$$D_b = m\,z\,\cos\alpha \tag{28}$$

Tip diameter:

$$D_a = r_p + 2\,m\,(1) + 2\,m\,x_i \tag{29}$$

Root diameter:

$$D_d = r_p - 2\,m\,(1{,}25) - 2\,m\,x_i \tag{30}$$
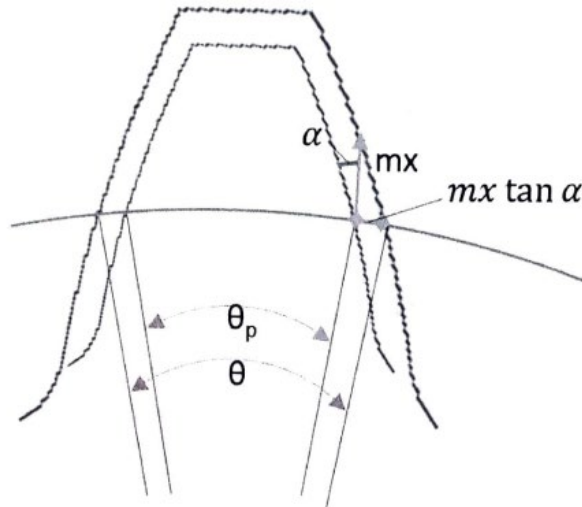
Figure 4. Tooth thickness alteration with profile shift

$$\theta_p = \tan\alpha_w \tag{31}$$

To specify backlash and profile shift effect on tooth thickness in gear geometry calculation

$$\gamma = \frac{\pi m}{2} + 2\,m\,x\,\tan\alpha - b \tag{32}$$

98
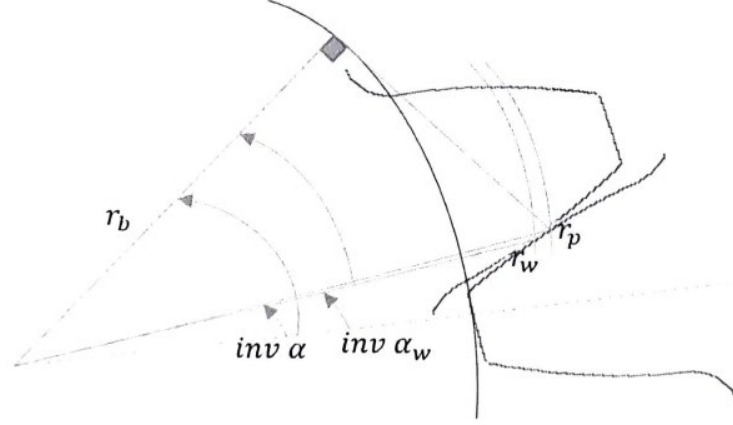
Figure 5. Determining amount of profile shift

Instantaneous tooth thickness for each roll angle increment:

$$S_{any} = r_{any}\big(\gamma + 2*(inv\,\alpha_w - inv\,\alpha)\big) \tag{33}$$

Amount of total profile shift:
Profile shift is applied to facilitate measurement on housing for determining shaft locations. Tooth thickness is supposed to change based on profile shift direction and amount.

$$m \tan \alpha\,(x_1 + x_2) = (inv\,\alpha_w - inv\,\alpha)(r_{w1} + r_{w2}) \tag{34}$$

$$x_1 + x_2 = \frac{(inv\,\alpha_w - inv\,\alpha)(r_{w1} + r_{w2})}{m \tan \alpha} \tag{35}$$

Here, x_1 or x_2 need to be defined to obtain other missing profile shift parameter.
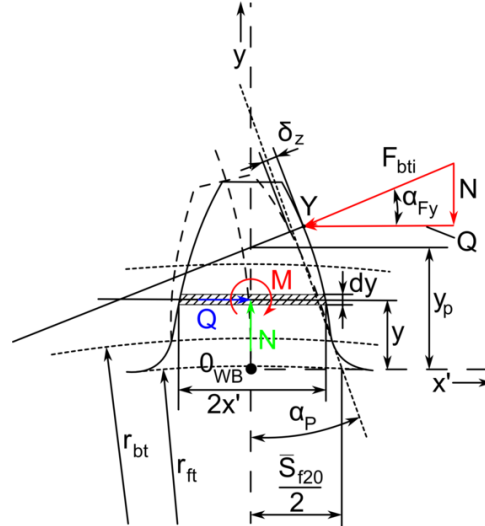
Figure 6. Bending, axial compression and shear deformation calculation [13]

$$\delta_z = \frac{F_{bti}}{b}(\cos\alpha_{Fy})^2\,\frac{1-v^2}{E}\left[12\int_0^{y_p}\frac{(y_p-y)^2}{(2x')^3}\,dy + \left(\frac{2,4}{1-v} + (\tan\alpha_{Fy})^2\right)\int_0^{y_p}\frac{dy}{2x'}\right] \tag{36}$$

Some parameters calculation can be made as below by following gear geometry principals. Before doing this, basic gear geometry parameters need to be on hand.
Roll angle for any point in contact that equal slice angles:

$$\theta_{any} = \left(\frac{r_{any}}{\frac{d_{b1}}{2}}\right)^2 - 1 = \tan\alpha_{any} \tag{37}$$

Tooth thickness at any point in contact

$$S_{w\,any} = r_{any} * \left(\frac{\frac{\pi*m}{2}}{r_{base}} + 2 * ((\theta_{ref} - \text{atan}\,\theta_{ref}) - (\theta_{any} - \text{atan}\,\theta_{any}))\right) \tag{38}$$

Linear tooth thickness

$$S_l = r_{any} * \sin\left(\frac{S_{w\,any}}{\frac{r_{any}}{2}}\right) * 2 \tag{39}$$

Load application point

$$RL = \frac{\frac{d_{b1}}{2}}{\cos(\beta_{any})} \tag{40}$$

Load application point distance from base diameter

$$Y_{p_i} = RL_i - \frac{d_{b1}}{2} * \cos\left(\pi * \frac{m}{d_{ref1}}\right) \tag{41}$$

Slice thickness for each roll angle increment

$$A_i = \frac{S_{l\,any_i} + S_{l\,any_{i+1}}}{2} \tag{42}$$

$$J_i = \left(\frac{S_{l\,any_i} + S_{l\,any_{i+1}}}{2}\right)^3 \tag{43}$$

Relation between roll angle, pressure angle and force at any point
$$\tan\alpha = \theta \tag{44}$$

$$\theta_{p\,any} = \frac{1}{2} * \frac{S_{w\,any}}{r_{any}} \tag{45}$$

Load angle on tooth can be found by using pressure angle at any point and tooth thickness angle.
$$\beta_{any} = \alpha_{any} - \theta_{p\,any} \tag{46}$$

100
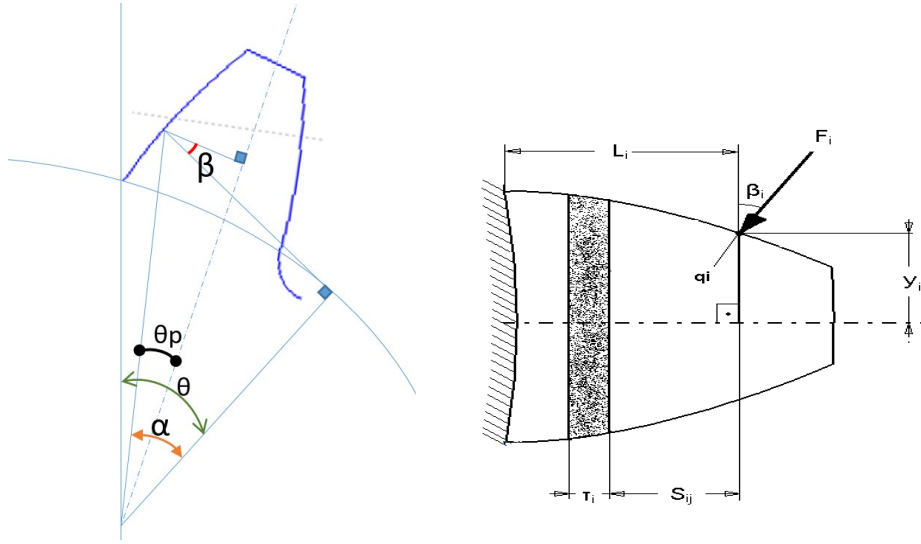
Figure 7. Determining load angle

Gear foundation deformation

This is the compliance between tooth root and gear body and independent from load according to Weber Banaschek equation.
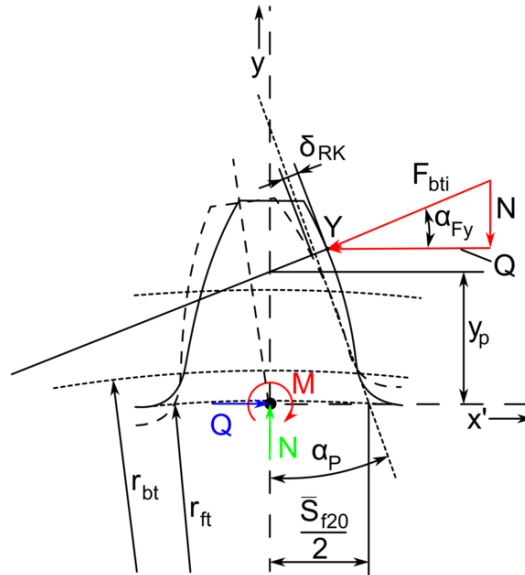
Figure 8. Gear foundation flexibility [13]

$$\left(\overline{Sf_{20}}\right) = 1{,}05 * ltt_{max} \tag{47}$$

y_p : distance from root

$$\delta = \frac{F}{b} \left(\cos \beta_{load}\right)^2 \frac{1-\nu^2}{E} \left[\frac{18}{\pi} \frac{y_p^2}{S_{f20}^2} + \frac{2(1-2*\nu)}{1-\nu} \frac{y_p}{S_{f20}} + \frac{4{,}8}{\pi} \left(1 + \frac{1-\nu}{2{,}4} \left(\tan \beta_{any}\right)^2\right)\right] \tag{48}$$

Hertz deformation
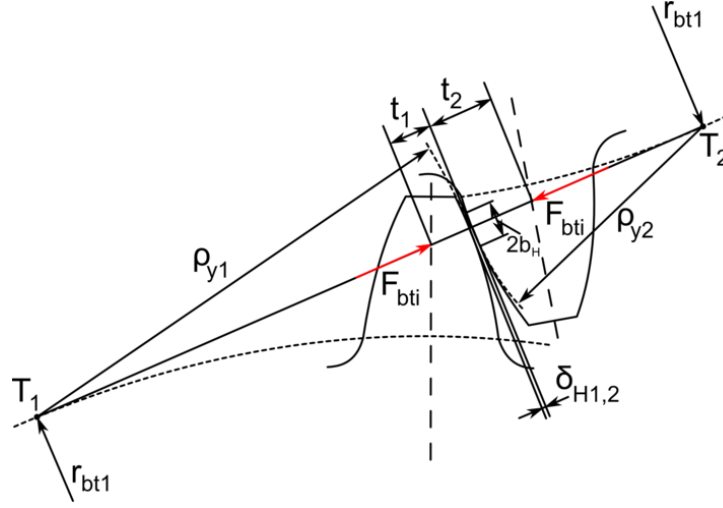
Figure 9. Determining compliance from Hertz deformation [14]

b_H directly depends on load in Hertz deformation equation, Hertz deformation is load dependent compliance type.

$$\rho_1 = \sin \alpha_1 * r_1 \ \ (\text{pinion}) \tag{49}$$

$$\rho_2 = \sin \alpha_2 * r_2 \ \ (\text{gear}) \tag{50}$$

$$E_r = 2 * \left(\frac{(1 - v_1^2)}{E_1} + \frac{(1 - v_2^2)}{E_2} \right)^{-1} \tag{51}$$
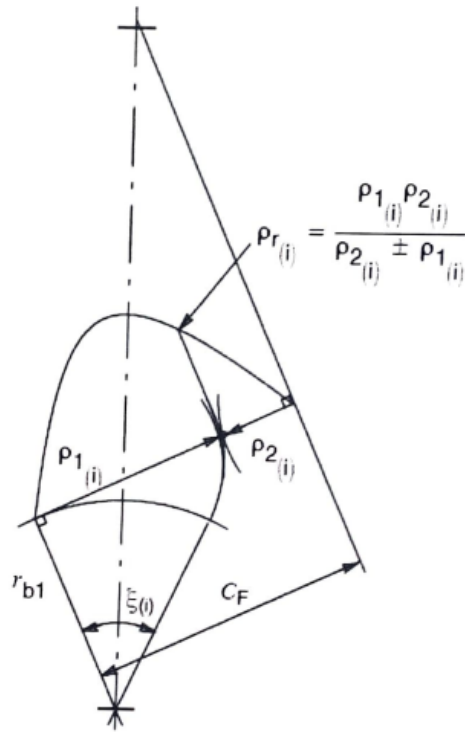
Figure 10. Radius of curvature [5]

$$\rho_{(i)} = r_{any} * \sin \alpha_i \tag{52}$$

$$\rho_{r\,(i)} = \frac{\rho_{1\,(i)}\,\rho_{2\,(i)}}{\rho_{2\,(i)} \pm \rho_{1\,(i)}} \tag{53}$$

102

$$W = \frac{F}{b} = \frac{T * \frac{1000}{0,5} * z_1 * m * \cos \alpha}{b} \tag{54}$$

$$b_H = \sqrt{8 * W * \frac{\rho_1 * \rho_2}{\rho_1 + \rho_2} * \frac{1}{\pi * E_r}} \tag{55}$$

$$t_{1,2_i} = \frac{ltt_i * 0,5}{\cos\beta_i} \tag{56}$$

$$\delta_{1,2} = \frac{F}{\pi * b_{1,2}} \left[\left| \frac{1 - v_1^2}{E_1} \ln\left(\frac{b_H^2}{4 * t_1^2}\right) + \frac{v_1(1 + v_1)}{E_1} \right| + \left| \frac{1 - v_2^2}{E_2} \ln\left(\frac{b_H^2}{4 * t_2^2}\right) + \frac{v_2(1 + v_2)}{E_2} \right| \right] \tag{57}$$

$b_{1,2}$ is taken as 1 mm.
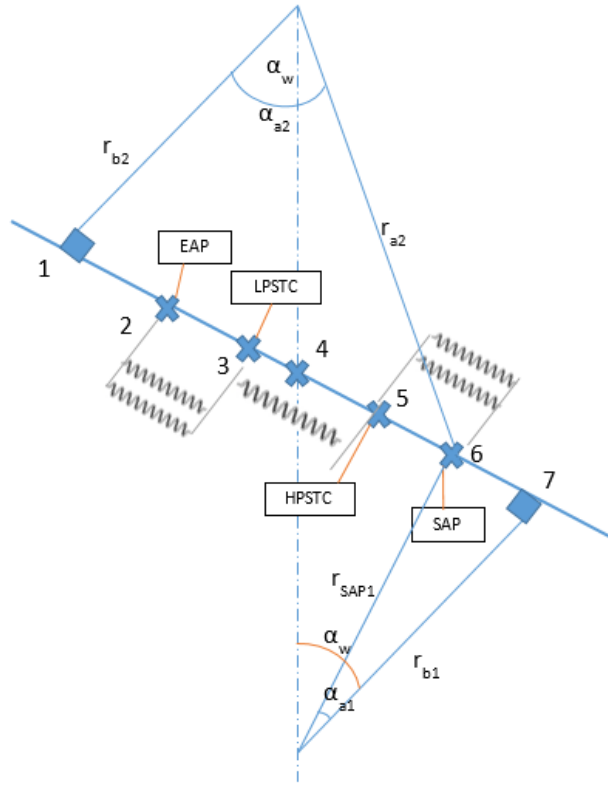
Figure 11. Mesh stiffness calculation based on single or double teeth in contact

Gear pair contacts single tooth, double teeth, and single tooth respectively in low contact ratio gear system. Pinion and gear is contacted in series when single tooth contact condition. During double teeth condition, two series contacts occurred and those are considered as parallel connection. Thus, mesh stiffness can be obtained by following this sequence.

$$k_1 = \frac{1}{\left(C_{b1} + C_{s1} + C_{a1} + C_{f1} + C_h\right)} \tag{58}$$

$$k_2 = \frac{1}{\left(C_{b2} + C_{s2} + C_{a2} + C_{f2} + C_h\right)} \tag{59}$$

$$K_1 = \frac{1}{k_1} + \frac{1}{k_2} \tag{60}$$

K_1 and K_2 can be found same algorithm and roll angle should be considered during summation. After defining HPSTC and LPSTC, K_2 is supposed to be taken as zero when single tooth contact.

103

$$K_{eq} = K_1 + K_2 \tag{61}$$

TRANSMISSION ERROR

Transmission error can be obtained by three methods in the literature: energy method, finite element method and by experiment. Profile modification and profile error is simulated as square wave during the transmission error calculations in some studies, and other studies includes these factors to mesh stiffness.

If there is no manufacturing and assembly error in the gear pair theoretically, pinion rotates constant speed, gear is supposed to rotate constant speed either. However, it is not possible to transmit fix torque transmission value in reality due to tooth and blank deformations. Transmission error can be defined as tooth position difference between theoretical coordinate and actual one.
If torsional deflection is taken into account at rotational way, formula can be given as below in the simplest form:

$$TE = \theta_2 - \left(\frac{R_1}{R_2}\right)\theta_1 \ \ [rad] \tag{62}$$

Here, R_1 and R_2 represents base diameters, θ_1 and θ_2 gears rotational positions. Linear displacement along line of action can be stated as below:
Transmission error can be classified differently according to load and manufacturing error in the literature. [15]

$$TE = R_2\theta_2 - R_1\theta_1 \ \ [m] \tag{63}$$

Unloaded Static Transmission Error
Along the tooth profile and face width errors due to manufacturing and assembly. In this study, there are 3 sinus harmonics taken to represent this error type. Lower and upper boundaries of the error ranges are defined according to gear quality class, and then these specific values are determined with proportional to Ref [5].

Table 2. Manufacturing error for 3 grade gear

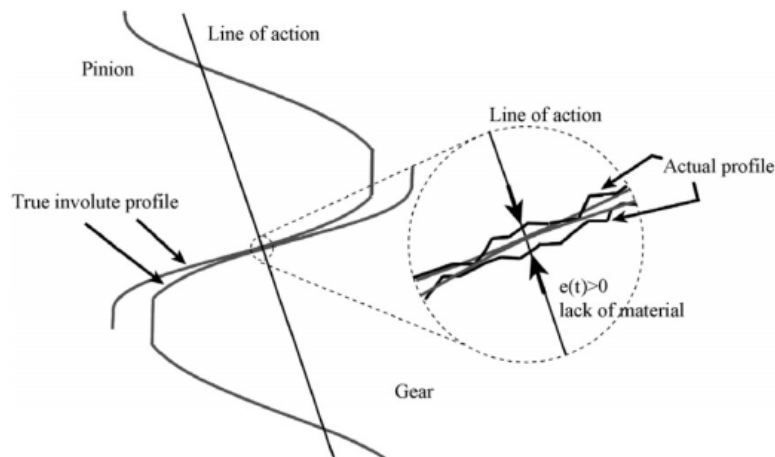| ω_m/ω_n	Manufacturing Error [μm]		Phase [rad]	
1	$\bar{E}_1$	2,176	γ_1	0,935
2	$\bar{E}_2$	0,452	γ_2	1,99
3	$\bar{E}_3$	0,18	γ_3	2,52

Figure 12. Manufacturing errors: lack of material along the line of action. [3]

Loaded Static Transmission Error

When torque is applied to gear, tooth will be deformed on line of action by these factors: bending, axial compression, shear, foundation compliance and Hertz deformation. In order to calculate these parameters, Weber Banaschek method is applied to find compliance per roll angle. Roll angle start with start of active profile (SAP) and ends with end of active profile (EAP) for each gear. Profile is sliced equal roll angle value and for each roll angle, compliance is supposed to be calculated. Hereby, single tooth contact and double tooth contact region mesh stiffness can be found by following this sequence. Firstly, compliance, and then mesh stiffness and loaded static transmission error is calculated respectively.
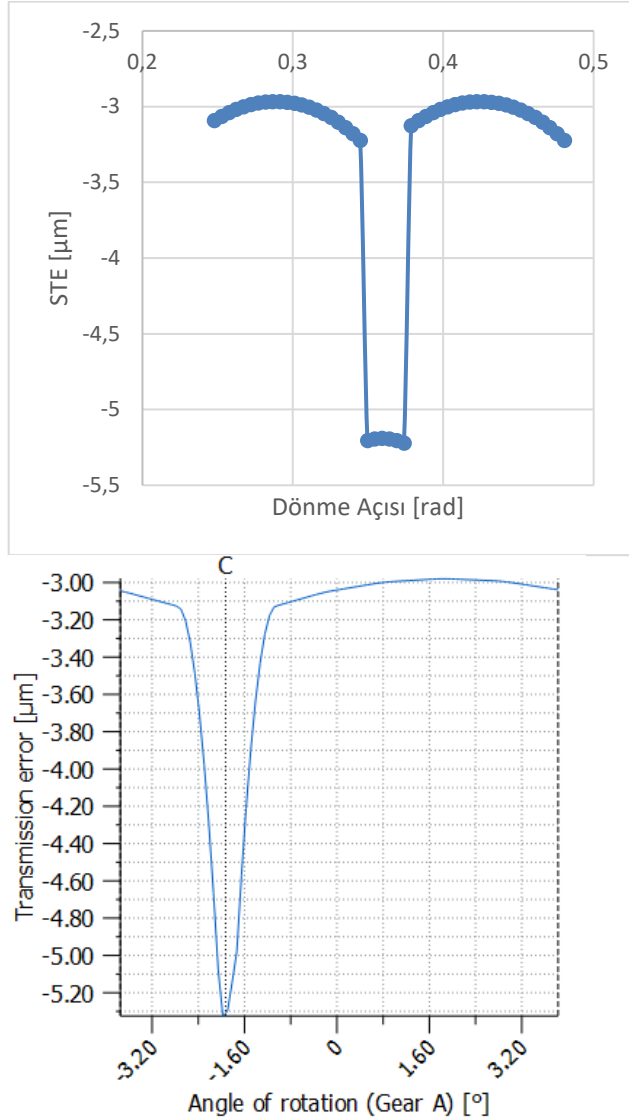
Figure 13. Loaded static transmission error calculation comparison with KissSoft program

Dynamic Transmission Error

Dynamic transmission error depends on several parameters like rotation speed. DTE can be defined as amplitudes of TE can be magnified by dynamic loading. [7] By this loading, dynamic loading and contact stress is increased and gear life is degraded.

- Rotating parts mass and inertias like gear, shaft
- Tooth, web blank, bearing and housing stiffness
- Coulomb or viscous damping could affect DTE directly.

$$I\ddot{\theta} + c\dot{\theta} + k\theta = T \ [Nm] \tag{64}$$

105

Gear Mesh Damping

Damping can be categorized as two section; material its own damping (hysteresis) and oil film damping. Oil film and its damping depends on gear geometry, rotation speed as well as viscosity, viscosity pressure factor and temperature of contact region.

$$c_{dişli} = 2\xi \sqrt{\frac{k}{\left[\left(\frac{r_{b1}^2}{J_1}\right) + \left(\frac{r_{b2}^2}{J_2}\right)\right]}} \qquad (65)$$

$$c_{şaft} = 2\xi \sqrt{\frac{k_s}{\left[\left(\frac{1}{J_1}\right) + \left(\frac{1}{J_2}\right)\right]}} \qquad (66)$$

Here, ξ denotes damping ratio. Gear damping ratio ranges between 0,03 and 0,17 in the literature. Shaft damping ratio is given between 0,005 and 0,075. J_1 denotes gear rotational inertia, J_2 gear moment of inertia. Shaft stiffness can be calculated by below formula in a simple way. [6]

$$k_s = \frac{I_s G}{L} \qquad (67)$$

Here, I_s represents polar inertia of shaft, G shear modulus, L shaft length.
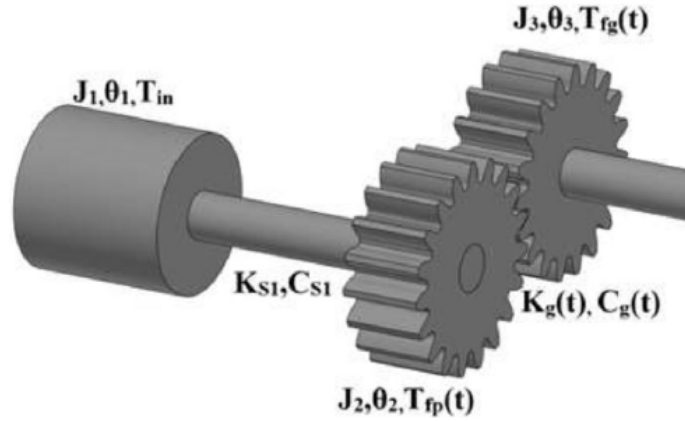
Figure 14. Determining shaft damping using gear and shaft inertias [6]

Backlash

Backlash is the clearance between the non-working flanks of two mating gears when their working flanks are in contact. Type of backlash is defined based on geometry as circumferential backlash and normal backlash. [12]

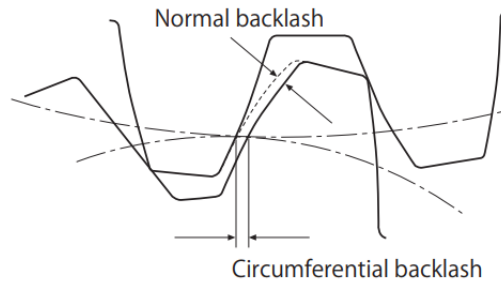$$j_n = j_t \cos \alpha \qquad (68)$$

Figure 15. Backlash types [16]

106

$$b_{min} = \frac{2(0,06 + 0,0005a_w + 0,03m)}{3} \tag{69}$$

$$b_{min} = \frac{2(0,06 + 0,0005 * 143,422 + 0,03 * 2,54)}{3} \tag{70}$$

$$b_{min} = 138,6 \ \mu m \tag{71}$$

Here a_w denotes working center distance between gear pair and m module.

Friction Force Calculation in Gear System

Firstly, power and torque values at input and output is supposed to be calculated theoretically assuming that there is no power loss.

$$P_2 = P_1 + P_3 \tag{72}$$

$$T_2 * \omega_2 = T_1 * \omega_1 + T_3 * \omega_3 \tag{73}$$

$$T_2 \ \omega_2 = T_1 \ \omega_2 \frac{n_2}{n_1} + \ T_3 \ \omega_2 \frac{n_2}{n_3} \tag{74}$$

Input and output torque values should provide below equation according to gear ratio.

$$T_2 = T_1 \ \frac{n_2}{n_1} + \ T_3 \ \frac{n_2}{n_3} \tag{75}$$

Friction force is calculated based on constant friction coefficient.

$$Fs_1 = W_1 * \mu \tag{76}$$
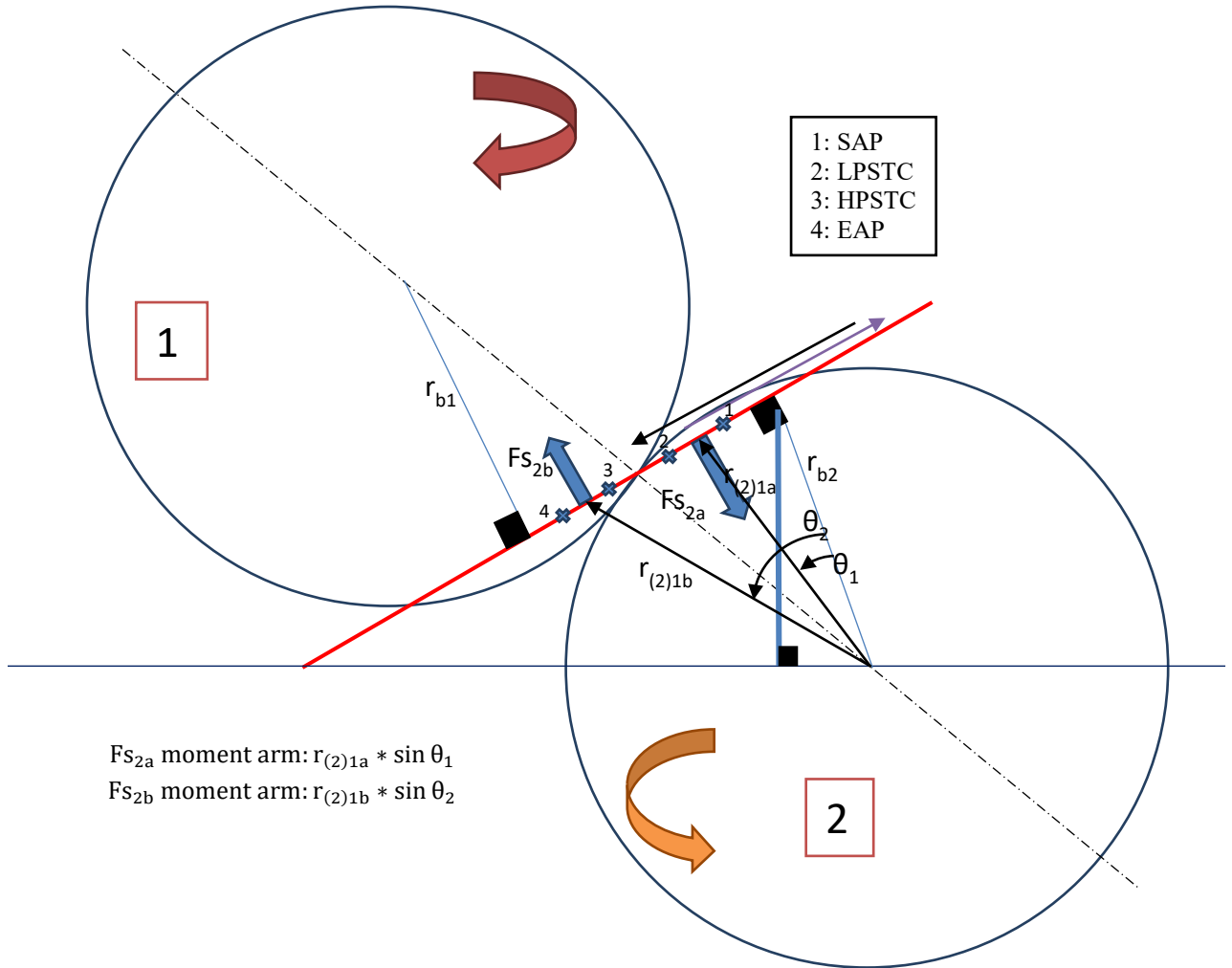
$$Fs_2 = W_2 * \mu \tag{77}$$

Figure 16. Determining friction torque based on contact point

Output torque fluctuation can be found by subtracting the calculated torque that caused by friction. Here input torque value is assumed as constant value. Firstly, actual normal force need to be calculated and then gear normal force should be taken as equal to pinion and inverse way.

$$T_2 = F_{n_{new}} * r_{b2} + Fs_{2a} * r_{(i)2a} * \sin(\theta_{(i)2a}) + Fs_{2b} * r_{(i)2b} * \sin(\theta_{(i)2b}) \tag{78}$$

$$F_{n_{new}} * r_{b1} = T_{1_{new}} + Fs_{2a} * r_{(i)1a} * \sin(\theta_{(i)1a}) + Fs_{2b} * r_{(i)1b} * \sin(\theta_{(i)1b}) \tag{79}$$

$$F_{n_{new}} * r_{b3} = T_{3_{new}} + Fs_{2a} * r_{(i)3a} * \sin(\theta_{(i)3a}) + Fs_{2b} * r_{(i)3b} * \sin(\theta_{(i)3b}) \tag{80}$$

Total power loss can found by two torque loss need to be multiplied with rotational speed.

$$P_{loss} = (T_1 - T_{1_{new}}) * \omega_2 * \frac{\pi}{30} * \frac{n_2}{n_1} + (T_3 - T_{3_{new}}) * \omega_2 * \frac{\pi}{30} * \frac{n_2}{n_3} \tag{81}$$
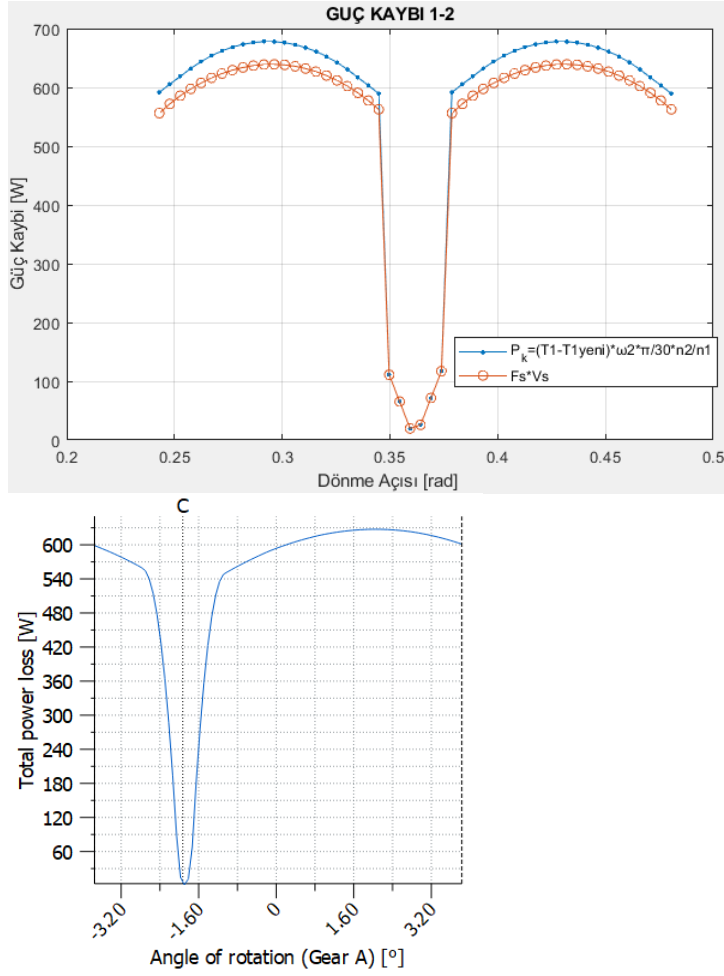
Figure 17. Power loss of gear pair calculation comparison with KissSoft program

As the comparison shown with program and obtained results, both power loss calculation F_s*V_s and friction torque is validated. Although power loss has not so much effect on overall torque transfer, this contributes to find more precise results with actual condition.

Mesh stiffness mostly depends on gear geometry and load as well. Here some gear geometry parameters and load factor is investigated to show how mesh stiffness change with variation of below mentioned parameters.

45-degree chamfer is applied to both gear in order to prevent extended tooth contact in the system. Therefore, smooth force distribution can be provided along tooth profile. Amount of chamfer depends on load magnitude. Chamfer causes to extend single tooth contact length on the profile. If chamfer value increases much than desired, then contact ratio decreases that may cause vibration problem.
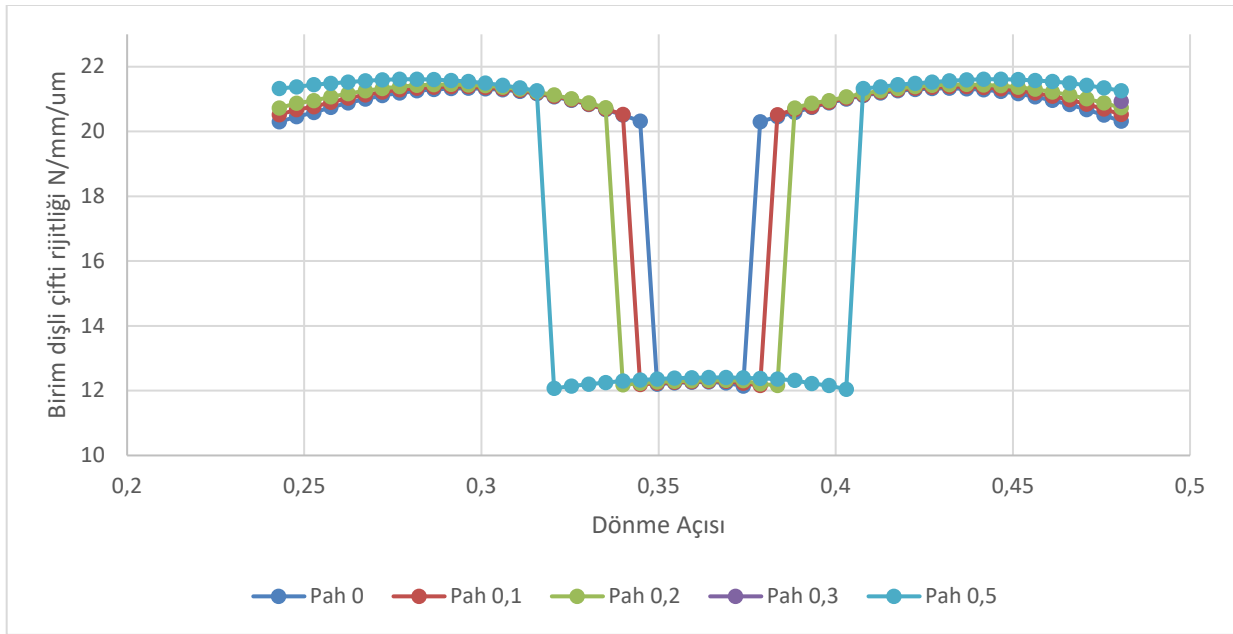
Figure 18. Mesh stiffness variation based on different chamfer values

In this study, gear center distance is presumable fixed. In other words, total profile shift is constant. One of the gear's profile shift value is varied to investigate mesh stiffness variation. Single tooth contact length along profile increases slightly, and magnitude of mesh stiffness around single or double teeth contact does not change.
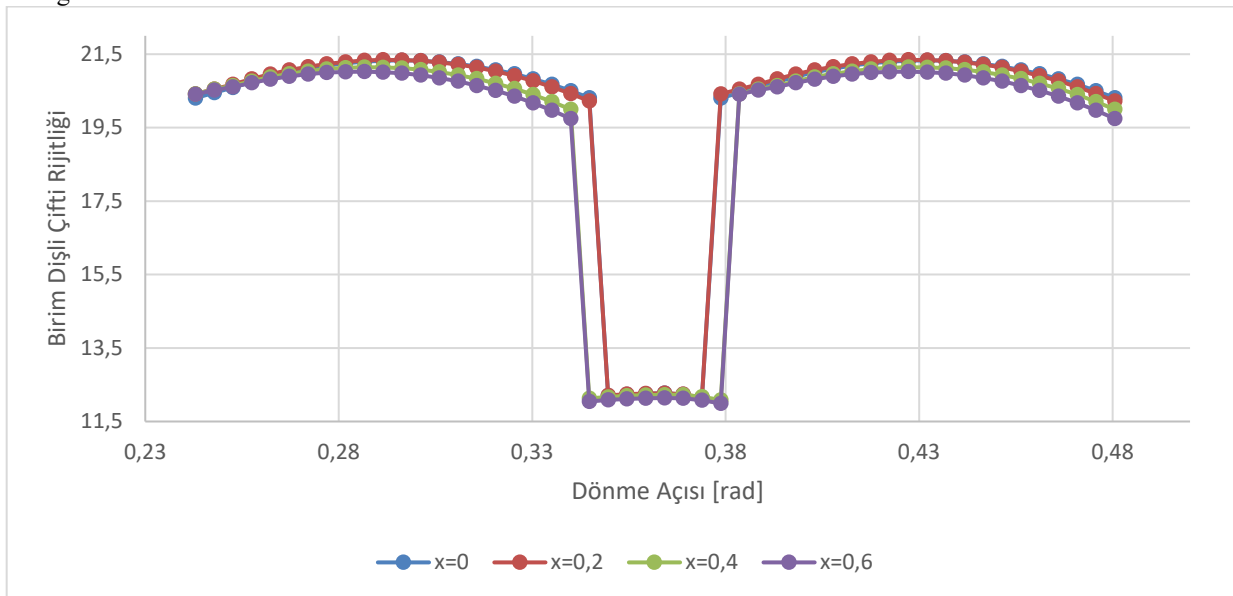

Figure 19. Mesh stiffness variation based on different profile shift values

Addendum coefficient is used 1 normally. If different addendum coefficient were to use, length of tooth is increased, so contact ratio increased as well. Thus, single tooth contact region reduces and double tooth contact region increases.
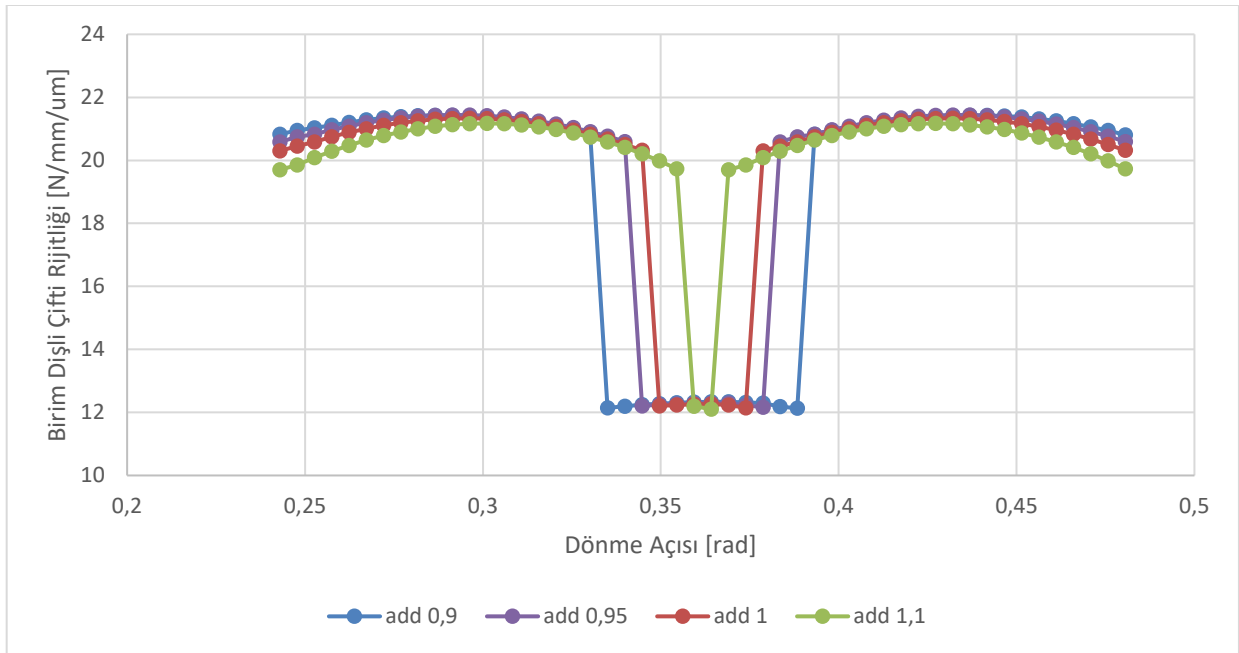
Figure 20. Mesh stiffness variation based on different addendum coefficients

Dedendum coefficient is used 1,25 normally. If different dedendum coefficient were to use, length of tooth contact does not change due to outer diameter is still same, therefore contact ratio does not change. Thus, single tooth contact length and double tooth contact length are same. Mesh stiffness reduces due to bending compliance increase as tooth length.
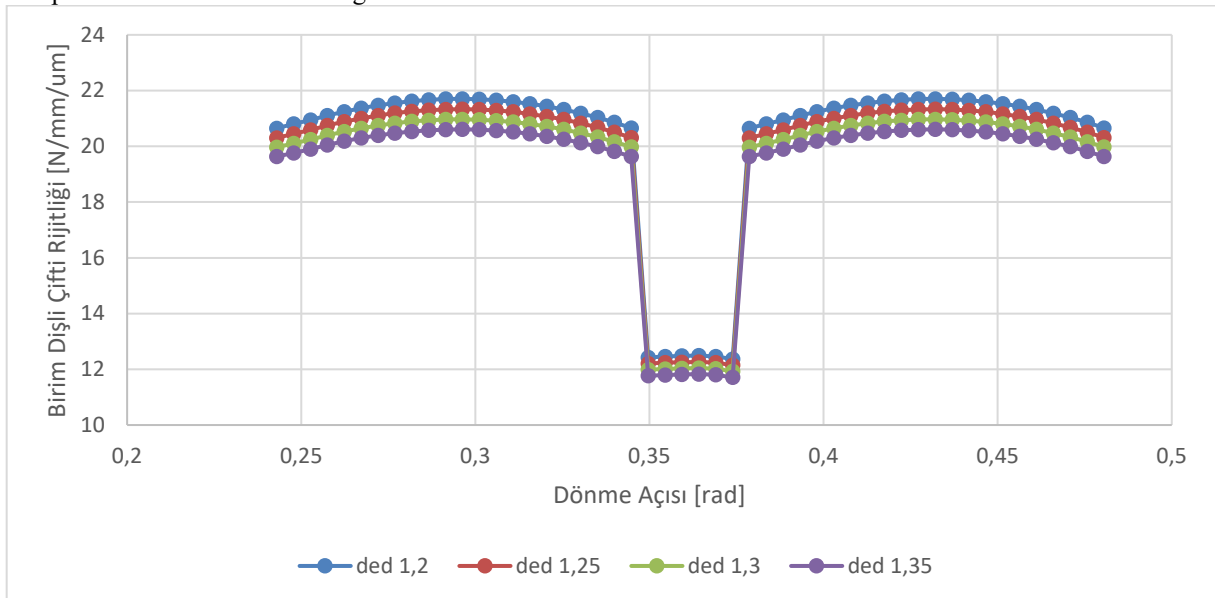

Figure 21. Mesh stiffness variation based on different dedendum coefficients

Generally, pressure angle is used 20 degrees in gear design. This parameter directly affects gear geometry so it changes amount of mesh stiffness as well as single or double tooth contact lengths on profile.
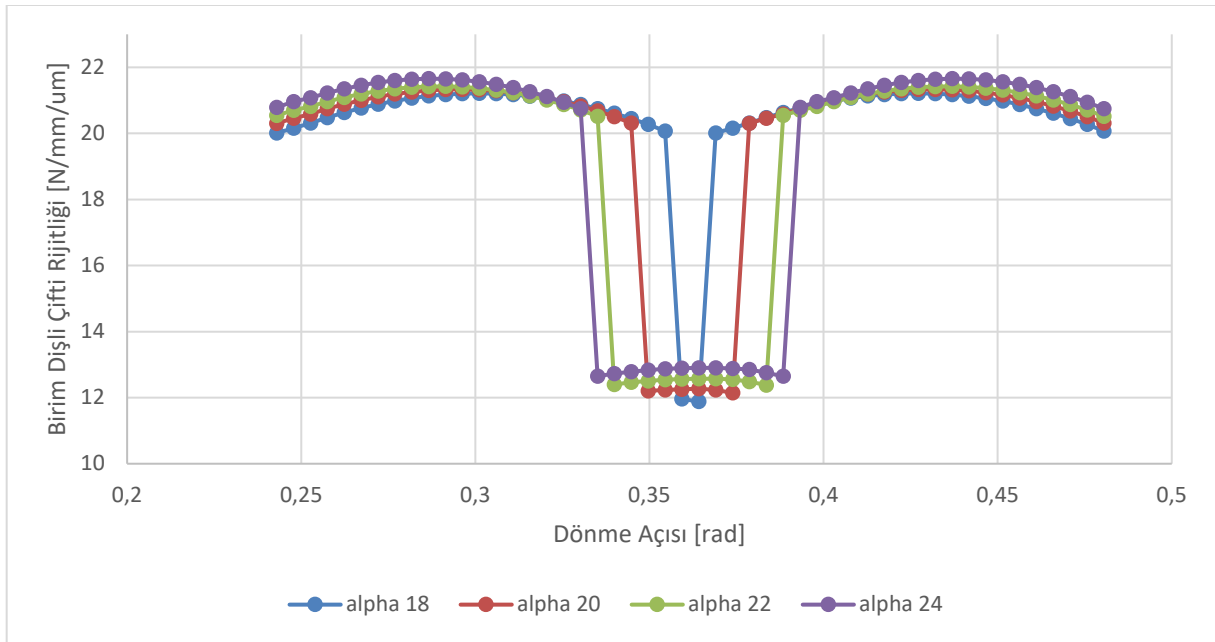
Figure 22. Mesh stiffness variation based on different pressure angles

There are some studies which deal with mesh stiffness independent from torque or power. Hertz deformation that one of the elements comprise mesh stiffness directly depend on force. Thus, whenever torque increase or decrease that amount changes Hertz deformation in gear system.
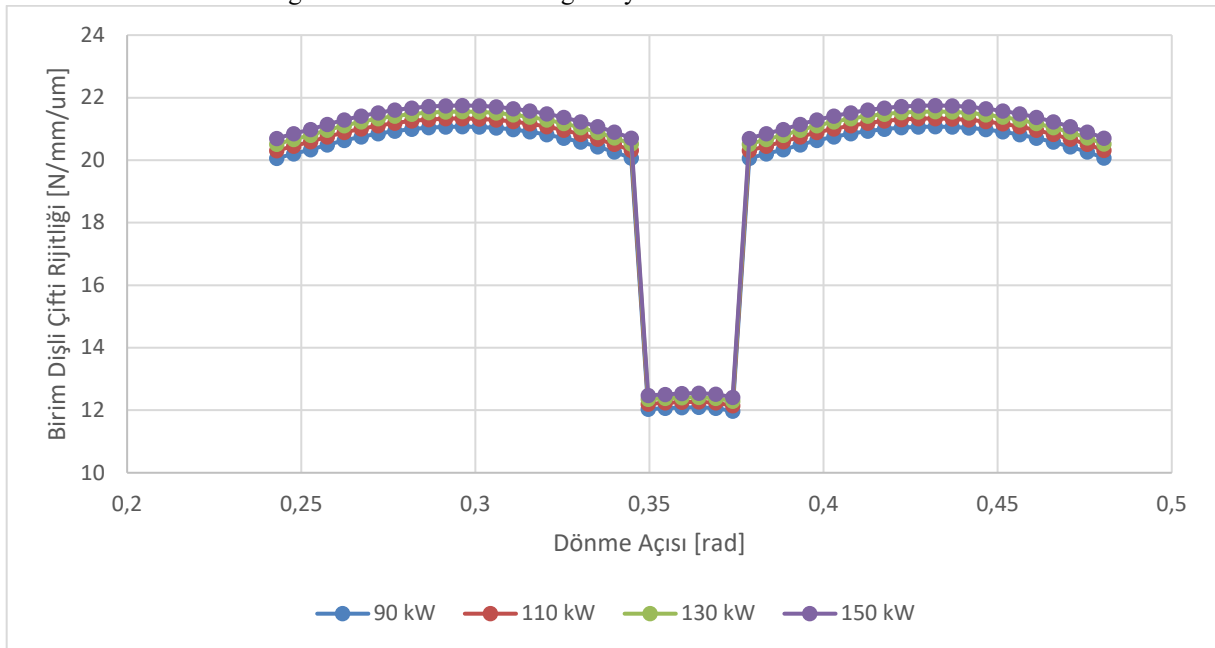

Figure 23. Mesh stiffness variation based on different input torque values

NUMERICAL RESULTS OF DYNAMIC GEAR MODEL

The experimental data of dynamic transmission errors from the published works are employed to validate the proposed model. The testing platform is a set of mechanical power enclosed gear transmission system test device for dynamic transmission error test of spur gears, as shown in Fig. 23. The basic parameters of the test

gears are given in Table 3.

Table 3. Test gear parameter at Ref [3]

|	Pinion	Gear
Number of Teeth	50	50
Module	3	3
Pressure Angle [°]	20	20
Base diameter [mm]	140,95	140,95
Tooth thickness at pitch diameter [mm]	4,64	4,64
Outer diameter [mm]	156	156
Root diameter [mm]	140,68	140,68
Face width [mm]	20	20
Mass [kg]	2,52	2,52
Inertia [kgm²]	0,0074	0,0074
Young's modulus [MPa]	206000	206000
Poisson's coefficient	0,3	0,3
Center distance [mm]	150	
Backlash on line of action [mm]	0,136	
Contact ratio	1,7547	
Profile modifications	None	
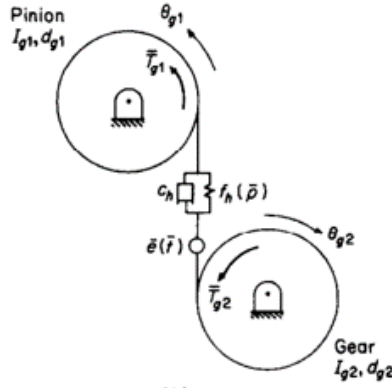
Figure 24. Schematic of 2 dof gear [4]

p_1 and p_2 represent the relative gear mesh displacements, which are the combinations of the dynamic and static transmission errors. [1]

$$p_1 = r_2\theta_2 - r_1\theta_1 - e_1 \tag{82}$$

$$p_2 = r_2\theta_2 - r_3\theta_3 - e_2 \tag{83}$$

Gear equations in torsional direction at rotational way:

$$I_1\ddot{\theta}_1 - r_1c_1\dot{p}_1 - r_1k_1g_1 =$$
$$-Fs_{1a} * r_{(i)1a} * \sin(\theta_{(i)1a}) - Fs_{1b} * r_{(i)1b} * \sin(\theta_{(i)1b}) \tag{84}$$

$$I_2\ddot{\theta}_2 + r_2c_1\dot{p}_1 + r_2k_1g_1 + r_2c_2\dot{p}_2 + r_2k_2g_2 =$$
$$Fs_{1a} * r_{(i)2a} * \sin(\theta_{(i)2a}) +$$
$$Fs_{1b} * r_{(i)2b} * \sin(\theta_{(i)2b}) + Fs_{2a} * r_{(i)2a} * \sin(\theta_{(i)2a}) + Fs_{2b} * r_{(i)2b} * \sin(\theta_{(i)2b}) \tag{85}$$

$$I_3\ddot{\theta}_3 - r_3 c_2 \dot{p}_2 - r_3 k_2 g_2 =$$
$$-Fs_{2a} * r_{(i)3a} * \sin(\theta_{(i)3a}) - Fs_{2b} * r_{(i)3b} * \sin(\theta_{(i)3b}) \tag{86}$$

In the system, torque is transmitted through gear via shaft. Equation right side shows friction force losses in regard to time or roll angle. Here, I_2 denotes pinion moment of inertia, I_1 and I_3 gear moment of inertia. For these two gear couples, nonlinear displacement functions can be defined as below. [4, 7]

$$\begin{cases} \mathbf{p_1 - b_1}, & p_1 > b_1 \\ \mathbf{0}, & -b_1 \leq p_1 \leq b_1 \\ \mathbf{p_1 + b_1}, & p_1 < -b_1 \end{cases} \tag{87}$$

$$\begin{cases} \mathbf{p_2 - b_2}, & p_2 > b_2 \\ \mathbf{0}, & -b_2 \leq p_2 \leq b_2 \\ \mathbf{p_2 + b_2}, & p_2 < -b_2 \end{cases} \tag{88}$$

It can be observed that the amplitude jump phenomenon occurs when the input speed is near the resonance speed of the gear system due to total tooth separations which are caused by too large relative dynamic displacement on line of action. The jump speed in the speed-up process is not consistent with the decline speed in the speed-down process, when the input speed is near the main resonance and harmonic resonance speeds of the system. The numerical results obtained using the proposed model suggest that the amplitude jump phenomenon can be accurately obtained as the input speed increases or decreases. [8, 14]
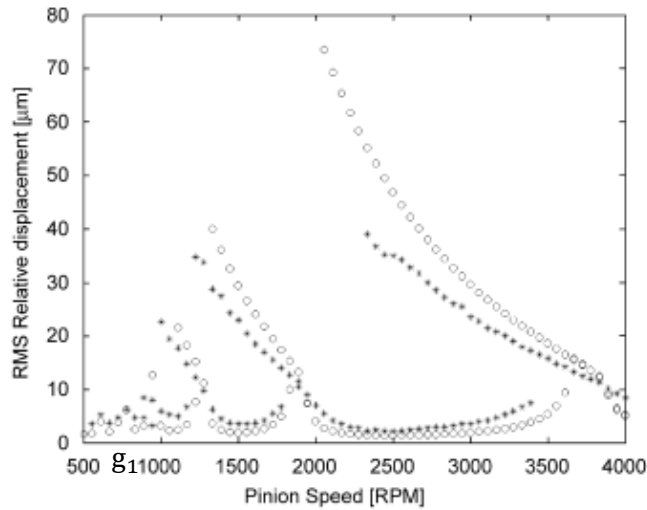

Figure 25. Comparison between numerical simulation and experimental data: (o) numerical simulation, (*)experimental data [5]

g_2

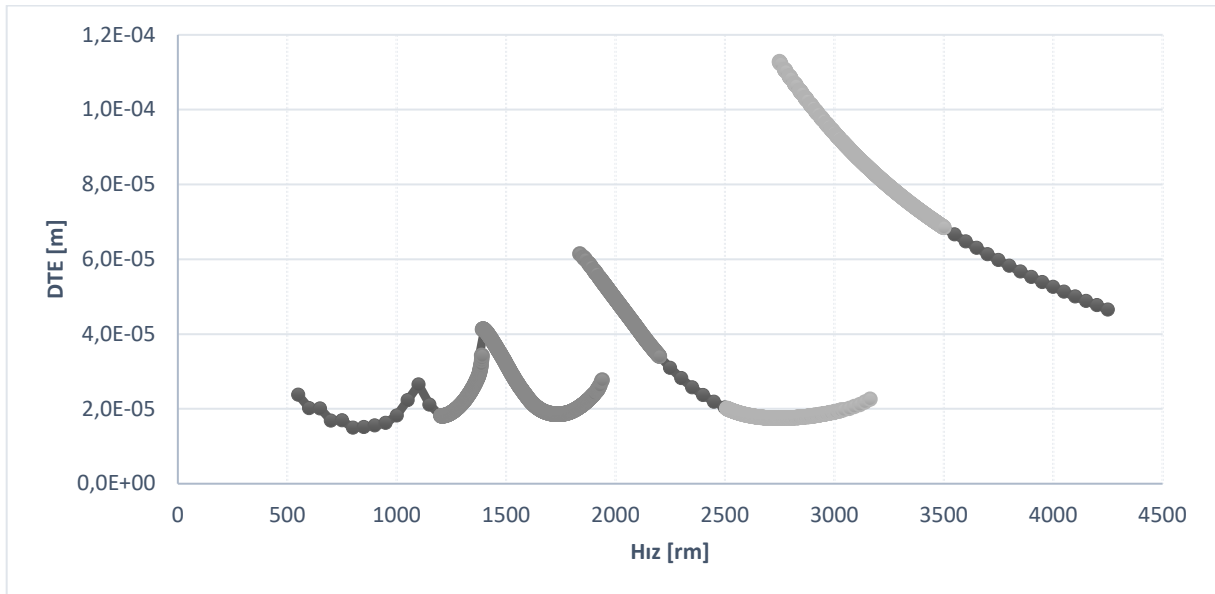|	Pinion	Gear-1	Gear-2
Number of Teeth	47	66	41
Module	2,54		
Working Pressure Angle [°]	19,9032	20,5554	
Base diameter [mm]	119,38	167,64	104,14
Tooth thickness at pitch diameter [mm]	3,8832	3,8086	4,1275
Outer diameter [mm]	124,46	172,5445	110,0356
Root diameter [mm]	113,03	161,1145	98,6056
Face width [mm]	20	20	20

Figure 26. Dynamic transmission error validation with Ref [5].

It can be found that the numerical results agree well with the experimental results. It can be found that experimental results considering especially frequency range.

Mass [kg]	1,7461	3,4433	1,3288
Inertia [kgm^2]	0,0031	0,0121	0,0018
Young's modulus [MPa]	206000	206000	206000
Poisson's coefficient	0,3	0,3	0,3
Center distance [mm]	143,422	112,161	
Half backlash on line of action [mm]	0,0693	0,0641	
Contact ratio	1,4043	0,8723	
Profile modifications	None	None	

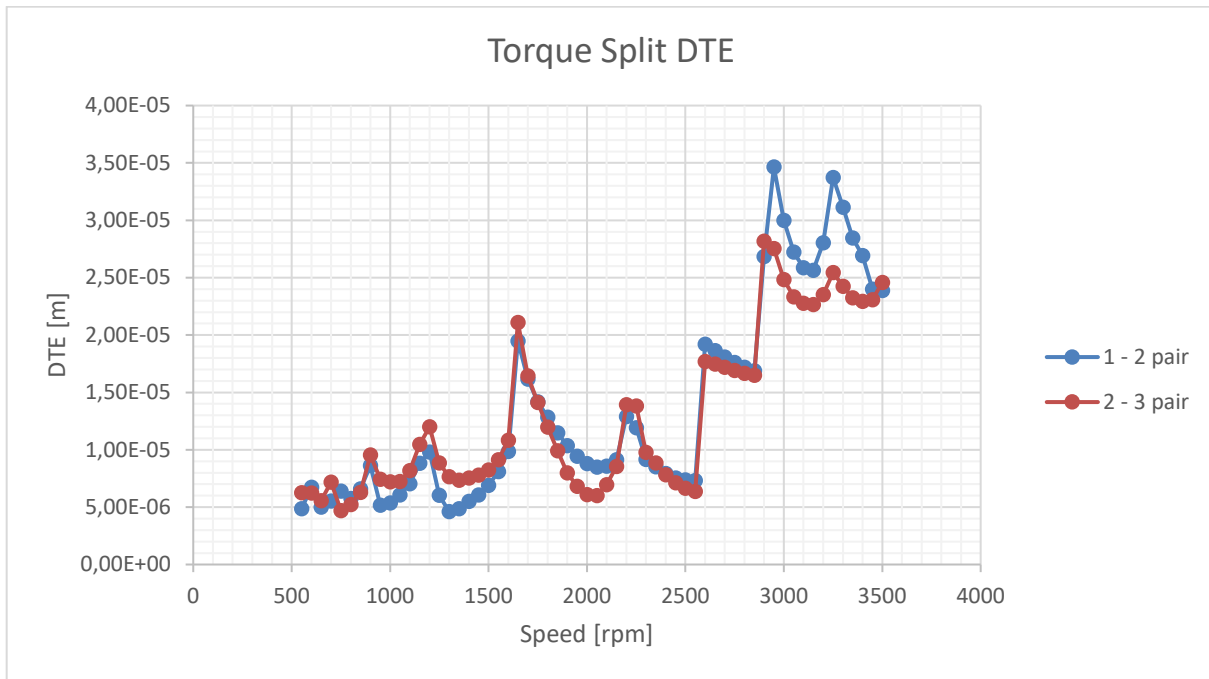Table 4. Complete geometrical data of used gear pairs

Figure 27. Torque split DTE results of two gear pairs

Phase is the difference between gear locations in terms of angle. Phase difference between gear pairs affects DTE results. In the next study, how phase difference contributes DTE in terms of speed and magnitude will be investigated. Optimization of phase angle in the design may improve vibration and noise characteristics.

Gear pairs can be excited by torque fluctuations due to other gear vibrations. Therefore, gear train is need to be modelled to evaluate all effects.

CONCLUDING REMARKS
System dynamic analysis is performed 0,5*10e-6 sampling time with ode4 Runge-Kutta solver with numerical integration.
Simulink/MATLAB has been used to carry out simulation study and findings are listed as below.

- There is no tip relief in gear design system. Mesh stiffness is one of the main inputs to DTE calculation and its excitation has a dominant factor in the simulation. In this study, how mesh stiffness can be affected by various factors from gear design geometry.
- After determining what comprises mesh stiffness, mesh stiffness variation given with some factors. Basically, lower contact ratio degrades vibration characteristics. Therefore, what reduces single contact length on profile improves DTE results like higher addendum coefficient. Meanwhile, gear

design constraints should be taken into account like gear tooth root failure. As a result, each of these factors should be studied one by one.

- Magnitude of relative RMS of DTE mostly depend on manufacturing error. As mentioned at Ref [3], manufacturing error values are need to be investigated with a statistical study that can be changed based on gear quality.
- DTE can be reduced to very low values by using perfect surface condition. STE can shift resonance region in speed axis as well as amplitudes of DTE.
- Gear mesh stiffness is time invariant in this model. Especially in spur gear system, mesh stiffness fluctuation affects DTE severely.
- Speed increment is done by sweeping. By doing this, transient phase to steady state phase period less than 0,05 sec. That is why, all analysis is performed for not much than 0,1 sec., and to eliminate transient effects first 0,05 sec. is ignored and second 0,05 sec. simulation data is investigated.
- Backlash affects DTE amplitudes in RMS evaluation, and peak to peak values of DTE is not affected by backlash except for resonance region.
- In case of increasing torque value, tooth touch stability can be improved. In other words, instantaneous pinion drive and contact loss condition can be reduced. If enough torque is applied to system contact loss condition could be shifted higher rotational speed values.
- Friction force has an impact at torque input fluctuation. System power loss of spur gear is around 1-2%, so torque loss that caused by friction force is in the same range with power loss.
- If contact loss is observed before resonance region, then jump phenomenon could not be seen in the resonance region. Contact loss begins during the jump phenomenon.

NOMENCLATURE

DOF   Degree of Freedom

DTE   Dynamic Transmission Error

EAP   End of Active Profile

HPSTC Highest Point of Single Tooth Contact

ISO   The International Organization for Standardization

LSTE   Lowest Point of Single Tooth Contact

LTI   Linear Time Invariant

LTV   Linear Time Variant

NTV   Non-Linear Time Varying

NTI   Non-Linear Time Invariant

RMS   Root Mean Square

SAP   Start of Active Profile

STE   Static Transmission Error

REFERENCES

[1] A. Al-shyyab, A. Kahraman, 2005, "Non- Linear Dynamic Analysis of a Multi-Mesh Gear Train Using Multi-Term Harmonic Balance Method: Period-one Motions," Journal of Sound and Vibration, vol. 284, pp. 151-172, 2005

[2] AGMA 913-A98 Standard

[3] AGMA 925 Standard

[4] A. Kahraman, R. Sing, 1991, "Interactions between Time-Varying Mesh Stiffness and Clearance Non-Linearities in A Geared System," J. Sound Vib. vol. 146(1), pp. 135-156, 1991

[5] Bonori, G., A., F. Pellicano (2007). Non-smooth dynamics of spur gears with manufacturing errors. 306, 271–283.

[6] Doğan, O., Karpat, F. (2019). Crack detection for spur gears with asymmetric teeth based on the dynamic transmission error. Mechanism and Machine Theory, 133, 417–431.

[7] G. Blankenship, A. Kahraman, 1995, "Steady State Forced Response of A Mechanical Oscillator with Combined Parametric Excitation and Clearance Type Non-Linearity," J. Sound Vib. vol. 185(5), pp. 743-765, 1995

[8] H. Özgüven, D. R. Houser, 1988, "Dynamic Analysis of High Speed Gears by Using Loaded Static Transmission Error," Journal of Sound Vibration, vol. 125(1), pp. 71-83, 1988

[9] H. Özgüven, 1991, "A Non-Linear Mathematical Model for Dynamic Analysis of Spur Gears Including Shaft and Bearing Dynamics," J. Sound Vib. vol. 145(2), pp. 239-260, 1991

[10] H. Özgüven, & Houser, D. R. (1988). Mathematical models used in gear dynamics—A review. Journal of Sound and Vibration, 121(3), 383–411.

[11] ISO 6336-1:2006 Standard

[12] 1SO 10064-2 Standard

[13] KissSoft Program Manual

[14] Yuan, B., Chang, L., Liu, G., Chang, S., Liu, L., & Shen, Y. (2020). An efficient three-dimensional dynamic contact model for cylindrical gear pairs with distributed tooth flank errors. Mechanism and Machine Theory, 152, 103930.

[15] Y. Saygili (2018). Torsional Vibrations of Gear Systems with Single And Dual Mass Flywheels Modelling and Analyses. MSc Thesis.

[16]https://www.kggear.co.jp/en/wp-content/themes/bizvektor-global-edition/pdf/1.7_Backlash_TechnicalData_KGSTOCKGEARS.pdf